Dynamical Properties of Dark Matter Halo Mergers: Observation of Heating and Mixing in N-body Simulations

by

Anael Berrouet

A thesis
presented to the University of Waterloo
in fulfillment of the
thesis requirement for the degree of
Master of Science
in
Physics

Waterloo, Ontario, Canada, 2015

I hereby declare that I am the sole author of this thesis. This is a true copy of the thesis, including any required final revisions, as accepted by my examiners.

I understand that my thesis may be made electronically available to the public.

Abstract

This thesis examines the nature of mixing and heating during the merging of single, isolated dark matter halos, as well as a short discussion of the statistical nature of repeated mergers in a cosmological setting. A small set of gravitational "N-body" simulationsof halo mergers are used to study heating and mixing, by measuring the dynamical properties of individual particles, as well as the overall properties of the merging halos. The accretion of mass onto a host halo is known to change the overall structure of the halo. Many previous studies have determined the general effect of mass accretion on the structure of the halo in general, and the concentration parameter in particular. Changes in this concentration parameter over the course of the merger are measured as a function of the mass of the incoming satellite and the circularity of the satellite's orbit. The amount of self-mixing in the radii and energies are also examined in order to determine the amount of memory preserved in the host halo throughout merger, as well as the amount of phase-space mixing between the host and satellite halos. Three possibilities are considered when observing how the host and satellite are mixed: that new material is layered onto the outside of the host halo and that new material falls into the center of the host halo, and that new material is evenly distributed throughout the host.

Halos are found to be unevenly heated by in-falling material. The heating overall tends to make the halo expand and experience a drop in its concentration parameter due to the increase in scale radius. Examining the cumulative mass distribution and the density profile of each halo through time, it is clear that material from the core is transported to larger radii during the merger. The scale radius presents the most relevant parameter with which to measure heating, as it represents the extent of the core of the halo. The relative increase in this observable appears to have non-trivial dependence on the mass ratio of the merging halos. We develop a simple model which provides the ability to estimate the change in the scale radius as function of the mass ratio of the merging objects. The model does not take circularity, or the total energy of the orbit into consideration, but the orbital energy of each orbit is representative of cosmological energies expected and any dependence on the circularity is actually extremely weak. Future work will examine the particular nature of these dependencies.

Mixing within the host is found to be relatively inefficient, with a maximum mixing leading to a rank correlation of approximately ~ 0.7 in radius and ~ 0.65 in energy. This relatively small amount of mixing is even less visible when particles are binned in to radial shells, explaining previous findings of very little mixing in the literature.

We also investigated the nature of phase-space mixing, that is mixing in position-velocity space, between the host and satellite halos. We expected a certain amount of

phase-space mixing among the merging structures, due to the fact that they must overlap spatially, and that exchanges of energy would bring their velocity distributions closer together. Overall, merging halos will tend towards equipartition of their energies through dynamical friction. We find that phase-space mixing is most efficient at mass ratios close to 1:1. The distance between the phase-space distributions of each halo, as measured by a statistic outlined in this work, is found to be anti-correlated to the mass ratio.

Finally a few simple applications to previous work performed by Wong & Taylor (2012) as well as Fakhouri & Ma (2008) is replicated. Using the mass accretion histories developed during this work, the heating model is applied to the mass accretion histories in order to build a theoretical concentration distribution prediction for halos at redshift $z = 0$.

Acknowledgements

I would like to thank my parents for their unwavering support, my supervisor for his guidance, and all my colleagues for our discussions of physics and other subjects. The isolated merger simulations described in this thesis were generated using intial condition codes and scripts written by our collaborators, Dr. Chris Power and Dr. Aaron Robotham, both at the International Centre for Radio Astronomy, University of Western Australia. We thank them for making this work possible.

Table of Contents

List of Tables

List of Figures

Chapter 1

Introduction

Understanding the nature of structure in our universe at all scales is one of the principal goals of astrophysics and cosmology. The most influential component in structure formation in our universe is dark matter, constituting the potential wells in which galaxies and other luminous substructures can form. The gravitationally bound structures in which galaxies and clusters of galaxies form are called dark matter halos. These halos, as studied by numerical simulation, appear to all have the same structural form. Whereas our understanding of the early universe has been greatly refined over the past decade thanks to advances in observational techniques and increases in computational power, the dynamical evolution of dark matter halos, although crucial and widely studied, has yet to be clearly understood. Halo evolution, and consequently halo mergers, are a fundamental component of large scale structure formation and greatly influence the formation of galaxies and galaxy clusters. Mergers occur due to the gravitational attraction between two distinct halos, pulling them together to form a single object. Through dynamical relaxation they combine to form a single combined halo, transforming the structure of the merging halos in the process. Although halos may gain mass from smooth accretion of surrounding matter, mergers are responsible for the growth of dark matter halos. Mergers are also responsible for a significant amount of the mass growth of galaxies. The structure of dark matter halos also plays a significant role in the formation of their galaxies and has been shown to exhibit properties which are ubiquitous across all halos. This universality is not completely understood but can be observed through simulation and has been the subject of intense study [27, 28, 10, 40]. In particular, the structure of these halos may be characterized by a single parameter, their concentration, a parameter relating how much mass is present in the core of the halo relative to its envelope. The halo concentration parameter has been shown to be related to the mass accretion history of halos [6, 46, 51, 50, 23], and as a result

mergers clearly must play a significant role in shaping the parameter, or at the very least these must be well understood in order to understand the changes in a halo's structure.

In this thesis, we use a small set of gravitational "N-body" simulations of major and minor mergers in order to better understand certain aspects of the merger phenomenon. The accretion of mass onto a host halo is known to change the overall structure of the halo, generally changing its concentration; we will determine the dependence of this concentration parameter on the mass of the incoming satellite as well as the differences in this dependence due to the circularity of the satellite's orbit. We will also verify the coherence of this interaction in the form of mixing of the internal host material with itself, as well as with the incoming material. We will consider three possibilities when observing how the host and satellite are mixed: that new material is layered onto the outside of the host halo and that new material finds itself into the center of the host halo, and that new material is evenly distributed throughout the host.

Chapter 1 will provide a more complete context for this research, discussing our current cosmological understanding of the universe, the nature and structure of dark matter halos, as well as the effects of mergers between them. Chapter 2 will summarize the particulars of running the simulations as well as detailing the orbital parameter that characterize these merger simulations. Chapter 3 will discuss the physical phenomena occurring during merger. Chapter 4 will discuss the nature of heating from encounters between halos, along with its effects on concentration and its dependence on the host-satellite mass ratio and on circularity. Chapter 5 will discuss how well memory of initial phase-space, and energy conditions is conserved, as well as measuring qualitatively the phase-space mixing between the host and satellite halos. The dependence of these processes on mass ratio and on orbital circularity will also be examined. Chapter 6 will deal with the more cosmological component, discussing the link with the mass-accretion histories and verifying the accuracy of merger rate calculations. A summary of the research performed in this thesis as well as the conclusions we can draw from it will be presented in chapter 7.

1.1 The Composition of the universe

The standard concordance model of cosmology presents a highly successful description of the universe. Although our understanding of this model is incomplete and many important problems still exist, this model provides a relatively robust understanding of the origin and evolution of large scale structure. Ultimately, we can break down the universe as we know it into three main components: a small baryonic and leptonic component making up approximately 4.9% of the energy density of our universe, and two large "dark" components.

Making up about 26.8% of our universe, the first dark component is cold dark matter (CDM), which is theorized to be composed of relatively massive, non-relativistic particles. These particles are expected to interact through gravitational force and may also interact through the weak force. As a result, they are largely unaffected by particle-particle interactions with one-another, and are therefore termed "collisionless". Making up 68.3% the second dark component is dark energy (Λ), a uniform vacuum energy density with negative pressure. Dark energy is widely considered to be a cosmological constant causing the expansion of the universe to accelerate, and will be referred to as such hereafter. These "dark" components are so called due to the fact that they are not directly observable. The equations governing the expansion history are given by Einstein's field equations. Under the assumption that the universe is homogeneous and isotropic (the Cosmological Principle), however, and that energy and momentum are conserved quantities, the field equations reduce to the Friedmann equations (e.g. Peacock (1999) [32]).

The first of the Friedmann equations is given by:

$$H^2 \equiv \left(\frac{\dot{a}}{a}\right)^2 = \frac{8\pi G}{3}\rho - \frac{\kappa c^2}{a^2} \tag{1.1}$$

Where H is called the Hubble parameter, $a(t)$ is the scale factor dictating the relative size of the universe, G is the gravitational constant, κ gives the curvature of the universe and c is the speed of light in vacuum. In a spatially flat universe where $\kappa = 0$, this equation may be simplified by removing the second term in the equation, allowing for the definition of a "critical density" corresponding to a given Hubble parameter. The critical density may then be given by:

$$\rho_{crit} = \frac{3H(t)^2}{8\pi G} \tag{1.2}$$

Thus, in the case of general κ, if the density $\rho(t)$ is larger than this value, the universe has a positive curvature corresponding to $\kappa = +1$, if the density $\rho(t)$ is smaller then this value, the universe has a negative curvature corresponding to $\kappa = -1$. The second Friedmann equation, referred to as the "acceleration equation", is given by:

$$\frac{\ddot{a}}{a} = \frac{4\pi G}{3}\left(\rho + \frac{3p}{c^2}\right) \tag{1.3}$$

Here p is the pressure of the various materials composing the universe. This pressure can be related to the density of these individual components through a relatively simple "equation of state" . Although equations of state may, generally speaking, assume complicated forms, the relevant cosmological components may be treated as dilute gases revealing a most

simple structure:

$$\omega \equiv \frac{p}{\rho} \tag{1.4}$$

Radiation has $\omega = \frac{1}{3}$, while non-relativistic matter,which includes dark matter which is collisionless, effectively has $\omega = 0$. Dark energy may be formally defined as having $\omega = -1$. Current measurements conclude that the universe is essentially spatially flat ($\kappa = 0$) although tensions exist between measurements on the specific value of H_0, the Hubble constant today. H_0 may be expressed in terms of the dimensionless Hubble parameter h, where $H_0 = 100$ h km s^{-1} Mpc^{-1}. In this way, uncertainty in the Hubble constant is relegated to its dimensionless counterpart.

It should be noted that on large scales the assumptions of homogeneity and isotropy have held up relatively well to observation, with a few notable exceptions. The homogeneity of the universe may be determined by a "homogeneity scale", a length scale above which, when averaged, a given region is within one percent of being completely homogeneous. Surveys and simulations suggest this length scale lies in the range $\sim 70h^{-1}$ Mpc to $320h^{-1}$Mpc [49][36]. In principle, structures cannot be larger than this scale as it would imply that the average density of the material, even when averaged at the homogeneity scale, would exceed the background density. A relatively small number (depending on the homogeneity scale chosen), of exceptions have been found due to technological advances in ground- and space-based observation allowing better detection of these objects. The Sloan Great Wall of galaxies was observed to be approximately 420 Mpc long in 2003[13] while the Huge Large Quasar Group (LQG) has a characteristic size of approximately 500 Mpc, with its longest dimension at approximately 1240 Mpc, much larger than the homogeneity scale[8]. This study however will continue under the assumption that the cosmological principle holds true.

It may also be useful to define a dimensionless density parameter:

$$\Omega(z) \equiv \sum_{i=1} \Omega_i \tag{1.5}$$

where

$$\Omega_i = \frac{\rho_i}{\rho_{crit}}, \quad i = m, r, \Lambda \tag{1.6}$$

It will be useful later on to note that $\rho_m \propto (1+z)^3$ when relating the density of halos to that of the background density, or discussing the charactersitics of these large-scale structures.

1.2 Matter and Large Scale Structure

All structure in the universe is made up of matter, although as discussed previously, not all matter is equal. The structures we can see (e.g galaxies or clusters of galaxies) are made of baryonic and leptonic matter, matter which interacts with light. Luminous structures contain matter which interact through four fundamental forces: strong, weak, electromagnetic and gravitational. As a result, structures made of these types of particles are highly complex dynamical systems. The large structures formed by this material are called galaxies, galaxy clusters, and super clusters. These systems and the particles which compose them interact with dark matter through gravitational interactions, and as a result end up at the bottom of potential wells created by the large dark matter structures which surround them. Dark matter, which makes up most of the total matter component of the universe, does not interact with light and in fact interacts only through the gravitational and weak forces. As such, observations we make about dark matter are all indirect measurements in that we cannot observe them as we do with luminous matter.

The existence of dark matter was first proposed by Fritz Zwicky in 1933 when observing the doppler shifts of galaxies in galaxy clusters[52]. Since then, many (better) cosmological tests of dark matter have determined that dark matter is in fact present. Work done by Vera Rubin provided robust data demonstrating the need for dark matter to account for discrepancies in galaxy rotation curves[34, 35]. Dark matter may also be inferred from observations of gravitational lensing on many scales. Loosely speaking, a localized mass will distort spacetime such that light from background sources will bend around the massive object and reach an observer. From the geometry geometry of the distortion of the image seen by the observer, one can infer the amount of mass required to produce such an image. A well known lensing cluster is Abell 1689, which has been well studied using various techniques to determine its dark component. In cases using lensing like this one and other cases using alternative methods such as X-ray emission from baryonic gas, the mass-to-light ratios are consistent with the presence of dark matter constituting at least 60% of the cluster mass[22] by conservative standards and upwards of 85% by some estimates[1]. There is in fact most definitely significant evidence for the presence of large scale dark matter structures.

On large scales, dark matter is characteristically not diffuse, but rather tends to collapse into filaments and sheets as seen in dark matter simulations. The filaments themselves have a more diffuse component along with a higher density component in the form of gravitationally bound, collapsed, triaxial objects called dark matter halos[14, 3, 17, 20]. The objects at this scale (halos) and their dynamics have a significant and direct impact on the structure of the luminous matter we observe today and thus have been the subject

of intense study.

1.3 Dark Matter Halos

Within the context of the ΛCDM model, it is be possible to define the characteristics of a dark matter halo specifically. In this framework initial density fluctuations are found to be larger on small scales, and, since dark matter is collisionless, it has no pressure and may collapse even at very small scales. Moreover, the growth of large-scale structure, or dark matter halos, has been shown to be hierarchical[26], implying that large scale structure is formed both through the merging of smaller structures to form larger ones. Although halos have been shown to be triaxial rather than spherical[17, 20], as discussed earlier, the process of forming a halo may be approximated and better understood by modeling such an object as a collapsing sphere of dark matter.

1.4 Spherical Collapse

The most basic model for the formation of a dark matter halo is that of a spherically overdense region is space ($\kappa = +1$) embedded in a flat uniform background ($\kappa = 0$). We follow the derivation of Mo, van den Bosch and White (2010) [26] in order to compute the linear density perturbation at collapse. Using Newton's shell theorem or equivalently Gauss' law, all the matter surrounding the spherical perturbation has no gravitational effect and thus can be ignored. In the absence of a cosmological constant, for a shell of mass in this perturbation, the specific gravitational force is given by:

$$\frac{d^2r}{dt^2} = -\frac{GM}{r^2} \tag{1.7}$$

Integrating, we may obtain an equation representing energy conservation,

$$\dot{r}^2 = \frac{2GM}{r} + \varepsilon \tag{1.8}$$

In this equation, ε is the specific energy of the shell. Depending on the sign of ε, different solutions may be obtained. We will examine the case where $\varepsilon < 0$ for which the mass shell in question collapses (Potential Energy > Kinetic Energy). This differential equation has the parametric solution of the form,

$$r = A(1 - cos\theta) \tag{1.9}$$

$$t = B(\theta - sin\theta) \tag{1.10}$$

Plugging these solutions back into equation 1.7 and 1.8, we can relate A to B and both to ε through,

$$A^3 = GMB^2 \quad \text{and} \quad A = -\frac{GM}{2\varepsilon} \tag{1.11}$$

Thus, at some initial radius r_i and velocity v_i for the mass shell, $\varepsilon = \frac{v_i^2}{2} - \frac{GM}{r_i}$, and so, using the right hand side equation from 1.11 and the knowledge of H_i the Hubble constant at time t_i, the dimensionless density parameter $\Omega_i = \overline{\rho}(t_i)/\rho_{crit}(t_i)$, the mass overdensity δ_i related to the mass within the shell $M = (1+\delta_i)\overline{\rho}(t_i)(4\pi r_i^3/3)$ we may obtain an expression for r_i as,

$$\frac{r_i}{2A} = 1 - \frac{(v_i/H_i r_i)^2}{\Omega_i(1+\delta_i)} \tag{1.12}$$

We may then also develop an expression for the velocity of the mass shell,

$$v_i = \frac{dr_i}{dt_i} = H_i r_i \left(1 - \frac{1}{3H_i t_i}\frac{\delta_i}{1+\delta_i}\frac{d\ln\delta_i}{d\ln t_i}\right) \tag{1.13}$$

In such a universe, at early times the universe behaves as a $\Omega = 1$ universe, and as such $t_i \approx 2/3H_i^{-1}$. We can also determine, by comparing the Friedmann equations of both the background universe and the overdense region that the density contrast grows such that $\delta \sim a \propto t^{2/3}$. Using these statements along with the development of equation 1.13 where $v_i/(H_i r_i) \approx 1 - \delta_i/3$, we may express the constants A and B as,

$$A = \frac{1}{2}\frac{r_i}{\left(5\delta_i/3 + 1 - \Omega_i^{-1}\right)} \quad \text{and} \quad B = \frac{3}{4}\frac{t_i}{\left(5\delta_i/3 + 1 - \Omega_i^{-1}\right)^{3/2}} \tag{1.14}$$

The solution describing the motion of the mass shell in full, given by 1.9 and 1.10, indicates that the turnaround radius "r_{max}" of such a system occurs when $\theta = \pi$. As such,

$$r_{max} = 2A \quad \text{and} \quad t_{max} = \pi B \tag{1.15}$$

With the constants defined in terms of the initial conditions, the solutions may be freely explored and the properties of the system properly defined. Expanding 1.9 and 1.10 in terms of θ to higher orders we may obtain,

$$r = A\frac{\theta^2}{2}\left(1 - \frac{\theta^2}{12}\right) \tag{1.16}$$

$$t = B\frac{\theta^3}{6}\left(1 - \frac{\theta^2}{20}\right) \tag{1.17}$$

With a bit of algebra the radius of the overdense region may be re-expressed in terms of t,

$$r = \frac{A}{2}\left(\frac{6t}{B}\right)^{2/3}\left[1 \mp \frac{1}{20}\left(\frac{6t}{B}\right)^{2/3}\right] \tag{1.18}$$

Under the assumption of mass conservation, we can examine certain key events in a halos lifetime, estimating its overdensity at turnaround and its density at collapse, using linear theory. The initial mass of the halo is given by,

$$M_{init} = \frac{4\pi}{3}\overline{\rho}r^3$$

As the structure collapses, its density must increase by the overdensity δ and its radius will decrease by an increment "δr". The mass at a later time will then be,

$$M = \frac{4\pi}{3}(\overline{\rho} + \delta_\rho\overline{\rho})(r + \delta_r r)^3 = \frac{4\pi}{3}\overline{\rho}r^3(1 + \delta_\rho)(1 + \delta_r)^3$$

Equating these two masses we obtain $(1 + \delta_\rho) = (1 + \delta_r)^{-3}$, which may be Taylor series expanded to first order giving $\delta_\rho \approx -3\delta_r$. We can relate this δr back to the second term of 1.18 in order to quantify the evolution of the overdensity δ,

$$\delta \approx -3\delta_r = \frac{3}{20}\left(\frac{6t}{B}\right)^{2/3} \tag{1.19}$$

Using 1.19, the overdensity parameter δ can be estimated for both turnaround and collapse. At turnaround, occurring at $\theta = \pi$, we showed that $r = 2A$ and that $t = \pi B$. Thus,

$$\delta_{turnaround} = \frac{3}{20}(6\pi)^{2/3} = 1.06$$

We also demonstrated that at collapse ($\theta = 2\pi$), $r = 0$ and $t = 2\pi B$. As such the density parameter may be evaluated to be,

$$\delta_{collapse} = \frac{3}{20}(12\pi)^{2/3} = 1.69$$

The latter value has been derived using the linear approximation, and does not represent the actual overdensity the region achieves. In truth, the parameter should increase to

infinity, as the halo is spherically symmetric and pressureless in this model, so each shell collapses to zero radius. We have also assume that shells of mass do not cross and that they turn around and collapse at the same time. Of course, halos are not perfect spherical structures. Halos actually tend to be triaxial [17, 20]; small offsets due to local torques from other large scale structure create anisotropies and, in effect, impart small amounts of angular momentum as the halo collapses.

1.5 Halo Structure

1.5.1 Virialized Halos

As explained above, dark matter halos are in reality aspherical, and contain a net angular momentum. As such, halos do not collapse to a singularity; rather the process of collapse is stopped by "virialization". This stable state, virial equilibrium, is characterized by a condition called the virial theorem. This theorem, valid under the condition of energy conservation for an isolated system, and well defined time-averaged values of both the kinetic and potential energies, states that,

$$< T >= -\frac{1}{2} < U >$$

where $< T >$ and $< U >$ are the time-averaged values of the kinetic and potential energies, respectively. The virial theorem gives us the relationship between the kinetic and potential energies such that if $E = T + U$ and $-2T = U$, then $E = -T = U/2$. The following is the standard derivation for to overdensity parameter for a virialized structures. The final state of the collapsed structure is one in which $U = 2E$. At turnaround, since the kinetic energy is null, all the energy is contained as potential energy implying $E = U$. From the halo's initial state to final state, the potential energy is doubled, and since this potential has an r^{-1} dependence and all else is assumed to remain constant, the radius of the halo must then be halved. This tells us that $r_i = 2r_f$, where the turnaround radius is as shown in 1.15 above, $r_i = 2A$ implying $r_f = A$. This radius allows us then to compute the density of some collapsed halo with mass "M" as,

$$\rho_{halo} = \frac{3M}{4\pi A^3}$$

Moving past linear theory, we should be able to develop a more realistic collapse overdensity parameter. For an $\Omega = 1$ universe as found above, we derived a relationship between

the radius and time given by 1.18, relating this radius to its associated density, through $\rho = \frac{3M}{4\pi r^3}$, the average background cosmological density is given by,

$$\bar{\rho} = \left(6\pi G t^2\right)^{-1}$$

Using the time of collapse, also as above $t = 2\pi B$, this equation becomes,

$$\bar{\rho} = \left(24\pi^3 G B^2\right)^{-1}$$

The overdensity parameter may the be approximated by,

$$\delta \approx \frac{\rho_{halo}}{\bar{\rho}} = \frac{18\pi^2 MGB^2}{A^3} = 18\pi^2 \approx 178 \tag{1.20}$$

Dark matter density perturbations cause gravitational collapse. The matter then virializes and forms dense objects called halos; as shown above in 1.20 the structure may be deemed virialized once its mean density reaches a specific threshold relative to the critical density, $\Delta_c \equiv \rho/\rho_c$. The treatment above is limited in its use, but sufficient to describe this parameter as many simulations find using a $\Delta_c = 178$ yields appropriate results. A commonly used value for this density parameter is $\Delta_c = 200$, which for our purposes will be sufficient, and used henceforth. Defining this parameter we may also define the "virial radius" of a halo as the radius of a sphere centered on the halo, within which the density matches the density parameter condition exactly. As such,

$$\rho_{vir}(z) = \Delta_c \rho_c(z) = \frac{3M_{vir}}{4\pi r_{vir}^3}$$

so,

$$r_{vir}(z) \equiv \left[\frac{3M_{vir}}{4\pi \Delta_c \rho_c(z)}\right]^{1/3} \tag{1.21}$$

The spherical collapse model provides an estimate of the collapse time and final density of dark matter halos, but says nothing about their internal structure. Simulations do however give us the ability to predict the internal properties of the halo. Surprisingly, when studying dark matter halos, simulations demonstrated that although the mergers between halos are stochastic, halos as a whole demonstrate very universal characteristics[38]. The most popular characteristic shared by all halos, is that of a universal density profile. In the 1990s it became evident through the use of high resolution simulations that all dark matter halos had circular velocity profiles characterized fairly well by the same shape. This observation was found to be independent of any variation in halo mass, initial power spectrum, observation epoch and for various cosmological parameters (e.g Λ,Ω_m). This

characteristic was best captured through the measurement of the density profile. In their seminal papers, Navarro, Frenk and White[28, 27, 29] developed a two-parameter formula which they proposed as the universal density profile,

$$\rho(r) = \frac{4\rho_s}{r/r_s(1 + r/r_s)^2} \tag{1.22}$$

where ρ_s and r_s are the scale density and scale radius, respectively. The scale values refer to the density and radial coordinates corresponding to the point at which the logarithmic slope of the profile goes as $\mathrm{d}\ \ln\rho/\mathrm{d}\ \ln r = -2$. The scale radius marks one of the very interesting features of the halo, as it demonstrated that the universal density profile, rather than being scale invariant, depends on its history. As will be discussed in subsequent chapters, one can understand the scale radius as marking the boundary between two phases of accretion, fast and slow. A fast accretion phase may determine the size of the scale radius initially while a subsequent slow accretion phase may determine the exterior envelope of the halo[51]. This leads of course suggests a connection between the density profile and the merger history of the halo. Of course, the NFW model is not the only model which seems to fit dark matter simulations quite well. As higher resolution simulations were created and analyzed, small systematic differences between the observed trend and the NFW profile could be discerned. Navarro et al. (2004)[30] found that using the profile proposed originally by J. Einasto to fit star counts in the Milky Way [10], provided a much more suitable three-parameter fit to the average halo density profile over multiple halos, fitting the inner region of the halo more accurately[30]. It is worth noting, however, that the differences between any individual halo and either the Einasto or NFW model may often be more significant than the differences between the two models. The Einasto profile is as follows,

$$\ln\left[\rho(r)/\rho_{-2}\right] = -\frac{2}{\alpha}\left[\frac{r}{r_{-2}}\right]^{\alpha} \tag{1.23}$$

where α is an adjustable shape parameter with significant scatter, seen to have systematic mass dependence at redshift $z = 0$ demonstrating small deviations from, what would be, a true universal profile [12].

1.5.2 Concentration

A useful tool to characterize the internal structure of dark matter halos is the concentration parameter given by $c \equiv r_{vir}/r_s$, introduced by NFW in their seminal paper on dark matter halos[29]. The concentration parameter as it is defined serves to describe the shape of the

profile, essentially comparing the size and mass within the core to the size and mass in its outer envelope. This parameter will be further discussed in relation to mergers and mass accretions histories later below.

1.5.3 Mass Accretion History

A second significant universal trait is that of a universal halo growth pattern, that is to say, that halos all tend to grow in similar way: an initial period of rapid growth early in their lifetime followed a slower growth at later times. As with the density profile, the growth of mass of the halo as a function of time, or mass accretion history (MAH) was seen in simulations to generally have the same shape varying mainly with a breakpoint between the two accretion phases. Much research has gone in to developing models for MAHs. Van den Bosch (2002)[42] developed an average MAH model, experimenting with various fitting functions of the form:

$$\log(M(z)/M_o) = -0.301 \left[\frac{(1+z)}{(1+z_f)}\right]^{\nu} \tag{1.24}$$

where z_f and ν are fitting parameters. This rather complicated form provided a good quality of fit for late time halos, but showed weakness when fitting early forming halos. Almost concurrently, Wechsler et al. (2002)[46] had developed a single parameter fitting function in the form of an exponential as,

$$\frac{M(z)}{M_o} = e^{-\alpha z} \tag{1.25}$$

where α is a fitting parameter related to z_f by $z_f = \ln(2)/\alpha$. From these models McBride et al. (2009)[25] combined elements of both to develop a simple two parameter fitting function of the form,

$$\frac{M(z)}{M_o} = (1+z)^{\beta} e^{-\gamma z} \tag{1.26}$$

where β and γ are fitting parameters, and $\gamma = \ln(2)/z_f$. This fit, tested over a large mass range, was found to be in good agreement with halos taken from the Millennium Simulation. However, the fitted values β and γ are strongly correlated, suggesting the possibility for a better one-dimensional parameterization may be possible. Wong and Taylor (2012)[48], in order to develop a fit a single parameter carrying clear physical significance performed a principle component analysis on a set of MAHs in order to determine the functional form of this fit. Observing that $\sim 60\%$ of the scatter between MAHs was attributed to principle

component and noting the strength of its correlation with the concentration parameter, as well as $z_{0.5}$, the redshift at which the halo had built up half of its mas, it is clear that the principle component is a reflection of the age of the halo. This fit will be further discussed in chapter 6. Generally speaking, the relationship between the halo formation history and its concentration in particular has been has been well documented and researched (e.g. Wechsler et al. (2002)[46], Zhao et al. (2003)(2009)[51, 50]) and this relationship is quite well understood.

1.6 Halo Mergers

Although, on a statistical level we can predict the merger rates of halos, as well how many halos of a given mass to expect at any given time, mergers remain a stochastic phenomenon for any particular halo. As such it is inherently unsettling that all halos, independent of their merger history have many of the same universal characteristics.

Nusser & Sheth (1999)[31] investigated the differences between different types of mergers through the examination of disruptive and non-disruptive mass accretion in order to determine their effect on the density profile. The non-disruptive accretion case assumes that mass is accreted smoothly into the host and orbits within the host with mean radius equal to the virial radius at the time of merger with the host, a process they named 'stable clustering". The assumption that all accretion is done this way obviously incomplete, and rightfully is invalidated by simulations. Comparisons between the halos from CDM simulations and halos formed from MAHs under the assumption of stable clustering prove to be significantly different. The density profiles taken from CDM N-body halos demonstrate that halos of masses ranging from 10^{11} to $10^{13} M_{\odot}$ almost coincide over the range $0.1 > r/r_{vir} < 1$, while over the same range, the density profile of the halos formed using the stable clustering assumption are dissimilar. Stable clustering neglects the structured nature of mergers, often undergoing exchanges of energy via dynamical friction and leaving residual clumps in the final halo object. Under the condition that the merger is minor, that is not near 1:1, a fairly simple prescription of the merger may be given. The satellite will undergo tidal stripping outside some tidal radius r_t and undergo dynamical friction and exchange energy with the host. This analysis was also completed assuming that energy was re-distributed equally across the entire host rather than locally. Under this assumption, they found that the host halo is heavily influenced by the total overall amount of energy lost, or heating, from the satellite to the host. This work will venture to determine whether local heating or global heating plays a more dominant role in the changes to the concentration and consequently the density profile.

The orbital characteristics of mergers are also well documented. As the choice of many specific parameters are possible it is useful to know what real typical mergers may look like in order to best replicate reality. The circularity parameter may be defined as the ratio between the angular momentum of a particular orbit and that of a circular orbit with the same energy. We can define the circularity treating the halos as isolated point masses,

$$\eta = \frac{L(E)}{L_{circ}(E)} = \sqrt{1 - e^2} \tag{1.27}$$

where e is the eccentricity of the orbit. The circularity parameter distribution at redshift $z = 0$ is quite broad with a peak at $\eta \sim 0.5$ and very few highly radial or circular orbits[41, 44, 19, 47]. This distributions also exhibits dependence on the mass of the host halo. Lower mass hosts tend towards a more central value of the circularity while higher mass hosts show a weak negative correlation with circularity. When observing the satellite mass dependence, Wetzel (2011) finds no significant systematic dependence. What is found, however, is a dependence on redshift. Satellite orbits tend to be more radial and penetrate the host deeper at higher redshifts[47]. As a result of these dependences, circularities $\eta = 0.7\&0.3$ were selected for simulation. These values of the circularity represent both ends of the parameter space while being likely orbits with which a merger may occur.

As discussed briefly previously, the concentration parameter is known to trace the mass accretion history of a given halo quite well, demonstrating a dependence on the halo mass itself [51, 29]. This parameter defines not only the halo's current structure, but also its age. Zhao et al. (2003) postulated that halo accretion occurs in two distinct accretion phases. The first phase is characterized by frequent amounts of highly dynamical mergers with the mass of the halo increasing faster than $H^{-1}(z)$. It appears that in this early phase of accretion, the the scale radius increases rapidly, and approximately at the same rate as the virial radius. As a result, the halos in this early phase are observed to maintain a stable low concentration value. Once the turning point is reached, the halo then enters the second phase in which few or no significant mergers occur, such that the concentration grows consistently since the mass increases as $M_h \propto H^{-1}(z)$ with minor mergers being the dominant form of accretion. When modeling the concentration of these halos, the concentration seems to be best fit empirically by a value of $c = 4$ at the turning point between the two accretion phases. Although there is scatter in this value, the concentration seems to remain at roughly this value during the most of the early accretion phase. Having the initial concentration at a value of ~ 4 is not unique to Zhao et al. 2003, but has been observed as an empirical result through many simulations (e.g. Bullock et al. (2001) and Wechsler et al. (2002)); there has yet to be a formal theoretical framework describing this phenomenon. This may be understood as the result of the high amount of accretion

occurring throughout this portion of the halo's life. It is possible then that either a single major merger preferentially rearranges the profile such that the overall concentration drops to ~ 4, or that many mergers may lead to this result. It is evident that the concentration parameter must depend on cosmology and also of formation history, various models have been proposed (e.g. Bullock et al. (2001), Wechsler et al., (2002), Zhao et al. (2003)). The model proposed by Zhao et al. (2003)[51] is given by,

$$\left[\frac{M(z)}{M_o}\right]^{1-\alpha}\left[\frac{\rho(z)}{\rho_o}\right]^{\alpha} = \frac{[\ln(1+c) - c/(1+c)]\, c^{-3\alpha}}{[\ln(1+c_o) - c/(1+c_o)]\, c_o^{-3\alpha}}$$

where $M_{s,o}$ describes the mass within the scale radius $r_{s,o}$ at some fiducial redshift, notably the turning point z_{tp} defined in Zhao et al. (2003)[51]. Note, this function behaves like a simple power law for moderate concentrations. A dispersion of approximately 0.1 was found for the logarithmic value of the concentration for relaxed halos by Neto et al. (2007) in a suite of cosmological simulations, while in unrelaxed halos the dispersion grew to about 0.15. It is understood that mergers lower the concentration of halos through the distribution of kinetic energy injected from an in-falling satellite through dynamical friction. The specifics of the re-distribution of energy, however, is not well understood[31]. In chapter 3 of this work, we measure the dependence of the concentration parameter on on the mass ratio of the host and satellite halos , and the associated heating due to this merger is also examined. Where and when the kinetic energy from dynamical friction is redistributed in the host may prove to be important in defining how the concentration behaves post-merger.

1.7 This Project

This work will analyze simulations of single halo mergers, in order to determine the effect of mergers on the concentration parameter. Looking at two different circularities as well as various mass ratios, it is the intent of this work to determine how much the core of the halo gets heated, as well as observing when along the merger orbit, these changes occur. We also study the loss of memory of initial conditions in the form of self-mixing and the phase-space mixing of both host and satellite halos. We investigate any important structural changes and how these may be used to describe the level of differentiability between the host and satellite within the final halo object. Both components of this research are relevant to observational cosmology, describing the structure of luminous objects that trace dark matter. The concentration parameter characterises a halos age and describes the extent of the luminous matter within it. These are expected to change as a function of time

through merger. Understanding single merger events should allow the prediction of the concentrations of halos today. Determining the changes of internal structure may lead to predictions of where preexisting material in the host and new material from in-fall may be located within a system such as a galaxy cluster. Predicting the characteristics of old and new material would allow for age dating of material based on its phase-space characteristics and for comparisons of these predictions to known observations. The same would be true for our own galaxy, giving information about its local satellites. While idealized halos are smooth, real halos are not; they are "clumpy", being composed of past in-falling objects which may have retained some structure. Dark matter annihilation has yet to be detected, however, we know that if it does occur, the annihilation rate goes as $R =\sim \rho^2$, where ρ is the local density of the particles. This work may also play a role in predicting where annihilation may occur, providing a framework for identifying the possible orbital characteristics of these dense subhalo objects.

Chapter 2

Simulating Halo Mergers

The vast increases in computational power saw the rise of simulation as a method of solving complex physical problems. Today simulation and numerical computations are ubiquitous across most scientific disciplines and most research fields within them. Of particular interest to most astrophysicists are Hydrodynamic and N-body simulations. For our purposes, N-body simulations were used in order to understand the dynamics of discrete collisionless dark matter particles during merger.

2.1 N-body simulations

In particular, N-body codes deal with with problems that are not analytically soluble. A good example of this is gravitational dynamics; there exists no formal stable solution to the many body problem, that is, the gravitational dynamics of N particles where N $\geq$ 3. The equations of motion for a given particle, in an N-particle system, is given by,

$$\ddot{\mathbf{r}} = -G \sum_{j=1;j\neq i}^{N} \frac{m_j(\mathbf{r_i} - \mathbf{r_j})}{|\mathbf{r_i} - \mathbf{r_j}|^{\mathbf{3}}}$$

From this, one can solve for $\mathbf{r_i(t)}$ using a set of either 3N second-order differential equations, or 6N first-order equations, for each i from 1 to N. As a result operational cost of direct computational methods for a system of N particles goes as $\mathcal{O}(\mathrm{N}^2)$. Typically, the number of particles is extremely large (on the order of millions of particles), such that these direct integration methods are prohibitively expensive. In order to limit the expense of

calculations for large N systems of particles, multiple methods exist for reducing the number of operations necessary for the force computation to $\mathcal{O}(\mathrm{N}\log\mathrm{N})$, which scales almost almost linearly.

2.1.1 Tree Algorithms

Tree algorithms are one way to reduce the computational complexity. Tree algorithms reduce the complexity of force calculations by grouping particles together such that the computational costs may be reduced. A popular example of a tree code is the Barnes-Hut algorithm, which recursively divides particles into 1/8th sections of cubes, storing them in an *octree* for three dimensional simulations[2]. Each node of the tree represents a section of three dimensional space with one parent and eight children, who represent the eight octant subdivisions of that space. The space is recursively subdivided into octants, until either no particles, or a single particle is contained in a given space. In order to compute the force, the tree is traversed starting from the root (largest space) upwards. Whether the force is computed at the current node (space), or using its children is determined by an opening angle θ. This criterion essentially sets the accuracy of the simulation and may be written as $\theta = \mathrm{s/d}$ where s is the width of the region of the node and d is the distance between a particular particle and the center of mass of the node. This algorithm degenerates into a direct computation code for $\theta = 0$ and demonstrates increases in performance as θ gets larger, but at the cost of accuracy.

2.1.2 Particle-Mesh Algorithms

Particle mesh algorithms are by far the fastest schemes for calculating the gravitational field of a group of particles. This computation is accomplished by converting the system of particles into a grid of densities such that these may bay be used in conjunction with Poisson's equation. In Fourier space, the potential from Poisson's equation takes the simple form,

$$\hat{\Phi} = 4\pi G\frac{\hat{\rho}}{k^2}$$

where $\hat{\Phi}$ and $\hat{\rho}$ are the Fourier transforms of their real space counterparts Φ and ρ. Here, k is the co-moving wavenumber. Simply performing the inverse Fourier transform on this potential we may compute the gravitational field. This scheme is ineffective for short range interactions as it is most fundamentally limited by the spatial resolution of the cells.

2.1.3 Gravitational Softening

Another concern for N-body simulations, involves the presence of singularities. Any $1/r^{\alpha}$ force, where $\alpha > 0$, has the presence of a non-physical singularity at $r = 0$. In order to avoid any numerical divergences, it is possible to modify the potential function of the particles such that,

$$\Phi \propto \frac{1}{\sqrt{r^2 + \epsilon^2}}$$

Apart from preventing these numerical issues, the softening length also provides a buffer against two body interaction between particles. Dark matter particles in simulations do not represent real individual dark matter particles, but rather represent a large amount of them. As such the softening of the potential provides a sort of mass smoothing to more accurately reflect the dynamics.

2.2 Gadget

This set of simulations was produced using the Gadget-2.0.7 code produced by Volker Springel. The original Gadget-1 code which forms the foundation for this one, was produced by Springel at the Max-Planck Institute for Astrophysics under the supervision of Simon White. Gadget-2 was released as a complete reworking of its predecessor updating and improving algorithms and numerical methods. Gadget-2 utilizes what is referred to as a TreePM code, trying to combine the best of both numerical schemes taking advantage of their most efficient ranges, restricting the tree algorithm to short-range interactions, while computing the long-range interactions using a Particle Mesh algorithm. In Gadget-2 it is possible to define a number of numerical parameters to control the accuracy of the simulation. The code has undergone rigorous testing, and also provides recommended standard values for each of its free parameters. The opening angle θ may be set directly, as the Barnes and Hut algorithm is used as the Tree method. One can also specify the error tolerance for this parameter along with the error on the time stepping of the simulation.

In Gadget-2 gravity is softened using a spline, the single particle density distribution function $\tilde{\delta}$ is the Dirac δ-function convolved with a normalized gravitational softening kernel on a comoving softening scale ϵ. This kernel is given by a spline function,

$$W(r,h) = \frac{8}{\pi h^3} \begin{cases} 1 - 6(r/h)^2 + 6(r/h)^3 & \text{for} \quad 0 \leq \frac{r}{h} \leq \frac{1}{2} \\ 2(1 - r/h)^3 & \text{for} \quad \frac{1}{2} < \frac{r}{h} \leq 1 \\ 0 & \text{for} \quad \frac{r}{h} > 1 \end{cases} \tag{2.1}$$

such that the Newtonian potential of a point mass in non-periodic space is $-Gm/\epsilon$, equivalent to that of a Plummer sphere of length ϵ[37]. The Plummer sphere is simply a density law that was used by H. C. Plummer to fit observations of globular clusters [33]. The softening length is in internal units and when comoving integration is used, the solving of the equations of motions for each particle in comoving coordinates, then ϵ is also in comoving coordinates, which then usually stays constant throughout the simulation. The primary output from the Gadget-2 code is called a *snapshot* file. These files are output at predefined regular, linear or logarithmic, simulation time intervals. The information in these files are organized into blocks, each containing a particular type of information (e.g. positions, velocities, temperatures). The first block however, contains the global information of the simulation. These block are organized according to the type of particle but do not order the particles themselves in a coherent way. The simulation does however, provide particle identification numbers such that they may be tracked throughout a simulation. Snapshots by default are provided in unformatted binary, and so C-code is used to turn these files into easily viewable ASCII files. For more detailed formatting information and formatting options, one may refer to the User Guide.

2.3 Setup

As noted previously, these simulations were created using the Gadget-2.0.7 code created by Volker Springel[37]. These simulations were based off of initial codes created by Chris Power and Aaron Robotham. They were adapted to suit the specific needs of this research and provided the baseline for observing singular mergers in simulations. Multiple simulations exploring multiple circularities in conjunction with various host-satellite mass ratios were generated. The satellite halos in each case were placed at a distance slightly less than $2R_{vir,host}$, to then follow their respective orbits. The internal units of the simulation were in $M_{\odot}/h$, Kpc/h, and Myr, where each snapshot spans 0.955Myr. There are a total of 1401 snapshot, making for a simulation runtime of 13.37Gyr. These energies involved in each simulation are cosmologically inspired quantities based on the infall from the virial radius, and the corresponding energies of such an orbit. This work will analyze the dynamics of halo mergers with orbital energies equal to that of a circular orbit at the virial radius $\epsilon = E/E_{vir} = 1$. Two different circularities, $\eta = 0.3, 0.7$, were examined, each with host-satellite mass ratios 1:1, 2:1, 4:1, and 32:1. The naming convention used for these simulations is $EXXCYYMRZZ$, where XX denotes the relative energy parameter (e.g. E10 $\Rightarrow \epsilon = 1.0$), YY denotes the circularity parameter (e.g. C07 $\Rightarrow \eta = 0.7$), and ZZ denotes the mass ratio (e.g. MR05 $\Rightarrow M_{red}/M_{blue} = 2^5 = 32$). Both the satellite and the host

were generated such that their initial concentrations were $c_{host} = c_{sat} \sim 10$. These halos were created such that the were spherically symmetric and isotropic, with a Hernquist density profile[15]. Each halo was created with $N = 12100$ particles, where the mass of the host particles is $1 \times 10^8 M_{odot}$, and the mass of the satellite particls is scaled from this according to the prescibed mass ratio. As a result, the host halo mass is constant acrross all simulations with mass $1.21^{12} M_{odot}$, and its coresponding virial radius radius may be given by

The analyses of each simulations involved a softened potential $\propto (r^2 + \epsilon^2)^{-1/2}$, in order to more properly estimate quantities, with $\epsilon_{soft} = 1$kpc chosen to reflect a fraction the mean inter-particle spacing. Henceforth, the host halo will be referred to as the *red* halo and the satellite will be referred to as the *blue* halo as this distinction will be used in order to seperate the parameters involved with the host from the properties specific to the satellite.

2.3.1 Hernquist Profile

Although NFW or Einasto provide the most realistic representations of a cosmological halo's overall structure, their mass diverges at large radius. The Hernquist profile [15] is similar at small radii, but its mass converges at large radii, so we adopted it for this study. It is expected that analysis carried out in this work be repeated on a similar set of simulations using NFW halos. The Hernquist model was originally used to represent the internal structure of spherical galaxies. Many of its characteristic properties, such as the distribution function and the velocity dispersion, have simple analytic forms. The Hernquist density profile is given by:

$$\rho(r) = \frac{M}{2\pi} \frac{a}{r(r+a)^3} \tag{2.2}$$

Here, M is the total mass of the system and a is a scale length, essentially setting the breakpoint in the profile. At the center of the halo $\rho(r) \sim r^{-1}$ descending in power to $\rho(r) \sim r^{-4}$ in the outer regions. This profile also yields simple forms for the cumulative

mass distribution and potential. The cumulative mass distribution may be calculated as,

$$\begin{aligned} M(<R) &= 4\pi\int_0^R \rho(r)r^2dr = 4\pi\int_0^R \frac{M_o}{2\pi}\frac{a}{r(r+a)^3}r^2dr = 2aM_o\int_0^R \frac{r}{(r+a)^3}dr \\ &= 2aM_o\left[\int_0^R \frac{r+a}{(r+a)^3}dr - \int_0^R \frac{a}{(r+a)^3}dr\right] = 2aM_o\left[\left(-\frac{1}{(r+a)}\right)\Big|_0^R - a\left(-\frac{1}{2(r+a)^2}\right)\Big|_0^R\right] \\ &= 2aM_o\left[\left(\frac{1}{a}-\frac{1}{(r+a)}\right) - \frac{a}{2}\left(-\frac{1}{a^2}+\frac{1}{(r+a)^2}\right)\right] = M_o\left[2-\frac{2a}{r+a}+\frac{a^2}{(r+a)^2}-1\right] \\ &= M_o\frac{r^2}{(r+a)^2} \end{aligned}$$

Thus, it follows quite simply from

$$F = -\frac{GM(r)}{r^2} = \frac{\partial\Phi}{\partial r}, \tag{2.3}$$

integrating the force out to infinity that the potential is given by,

$$\phi(r) = -\frac{GM_o}{r+a} \tag{2.4}$$

Also of importance is the velocity dispersion profile derived by Hernquist (1990). The Jeans equation, for a spherically symmetric non-rotating system, determines the velocity dispersion and may be written as,

$$\frac{1}{\rho}\frac{d}{dr}(\rho\bar{v_r^2}) + 2\beta\frac{\bar{v_r^2}}{r} = -\frac{d\Phi}{dr} \tag{2.5}$$

where $\beta = 1 - \bar{v_\theta^2}/\bar{v_r^2}$ is defined as the anisotropy parameter, $\bar{v_r^2}$; $\bar{v_\theta^2} = \bar{v_\phi^2}$ are the radial and angular velocity dispersions respectively. For an isotropic system, the anisotropy parameter reduces to zero and using equations 2.2 and 2.4 in equation 2.5, the velocity dispersion in long form may be written as,

$$\bar{v_r^2} = \frac{GM}{12a}\left\{\frac{12r(r+a)^3}{a^4}\ln\left(\frac{r+a}{r}\right) - \frac{r}{r+a}\left[25+52\left(\frac{r}{a}\right)+42\left(\frac{r}{a}\right)^2+12\left(\frac{r}{a}\right)^3\right]\right\} \tag{2.6}$$

This quantity, being relatively simple for isotropic systems, will prove useful when calculating the dynamical friction later in this work since

$$\bar{v^2} = \bar{v_r^2} + \bar{v_\theta^2} + \bar{v_\phi^2} = 3\bar{v_r^2} \tag{2.7}$$

It became apparent that the choice of central position for the halo was an important one, as it may skew the spherically averaged density profile and other radial quantities. The choice then between the highest density position as approximated by the position of the most bound particle (MBP), and the center of mass, becomes relevant. As the particles are stochastically generated around the halo in order to match the prescribed density profile, the actual center of mass may be disproportionately affected by particles placed at large radii. Thus, any useful center of mass value is obtained by truncating the number of particles at some radius and then calculating the center of mass location. The offset of the center of mass in contrast with the location of the MBP may be seen in figure 2.1 where the center of mass of the blue halo is plotted in purple and the most bound particle is plotted in cyan; these points are overlayed atop both the blue and red particles, plotted in the x-y plane using the codes length units. The center of mass location also presents

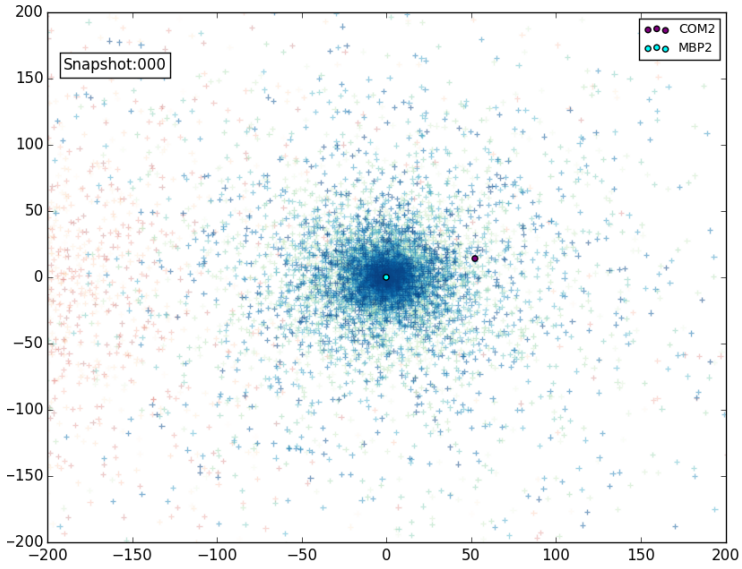

Figure 2.1: The center of mass, offset as compared to the most bound particle position for the satellite halo in simulation "E10C07MR02".

an added difficulty during highly dynamical events where deformation of the halo and mass loss may cause the center of mass to not be an accurate representation of the leftover satellite's bound core, as seen in figure 2.2 in which the particles from both halos, the MBP position and the COM position are plotted the same way as figure 2.1. Consequently, the MBP was selected to best represent the center of the bound core of the halo. The most bound particle presents its own challenges however, as it may oscillate about the center of the potential, or another particle, like a binary. This rotation about the center may be clearly observed in figures 3.2 and 3.1 in chapter 3. Due to this rotation effect with

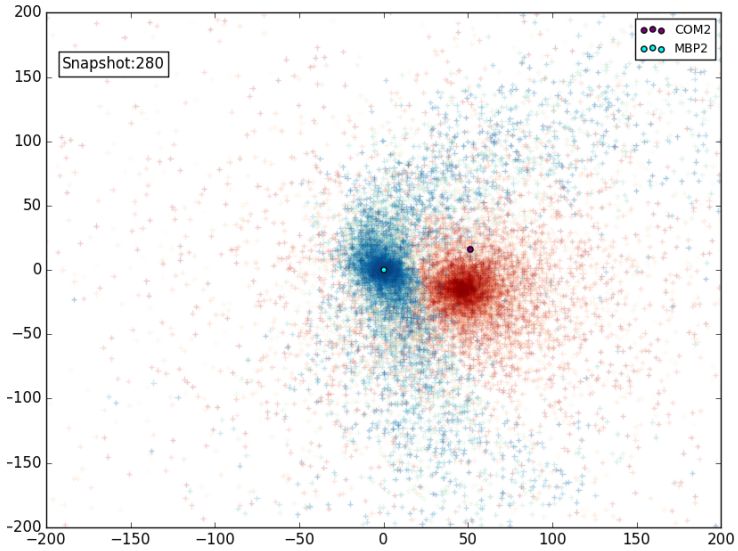

Figure 2.2: The center of mass, offset as compared to the most bound particle position of the satellite halo, during pericentric passage, in simulation "E10C07MR05".

multiple particles moving through the center of the halo, the most bound particle at any given moment is not necessarily the same, and may switch between these moving particles. The switching of particles may skew the understanding of the dynamics when discussing mixing and as a result the initial MBP in particular was selected to be the center of the halo throughout the entire simulation, noting that it unlikely that it should be stripped while a bound halo still persists.

2.3.2 Fitting the density profile

At every snapshot in the simulation, both halos' spherically averaged density profiles were fit with a Hernquist profile. Given that the mass of the halo M_o was well defined, the fit was then dependent solely on a single paramater, the scale radius "a". The best fit value for this parameters was obtained using a simple logarithmic χ^2 minimization given by,

$$\chi^2_{\rm Hernquist} = \sum_{i=1}^{N_{bins}} [\ln\rho(r_i) - \ln\rho_{\rm Hernquist}(r_i)]^2$$

where $Nbins$ is the number of bins when creating the density profile based on the actual distribution of particles. The fitting is performed in logarithmic space so as to provide a more even weighting across all density bins[16, 24].One could also imagine various fitting

methods including the use of a log-likelihood method for fitting, however this method is adopted as used in Wong & Taylor (2012). In fitting the profile, the most bound particle was used as the center of the radial density profile and generally produced good fits to the analytic density profile, as seen in figure 2.3.

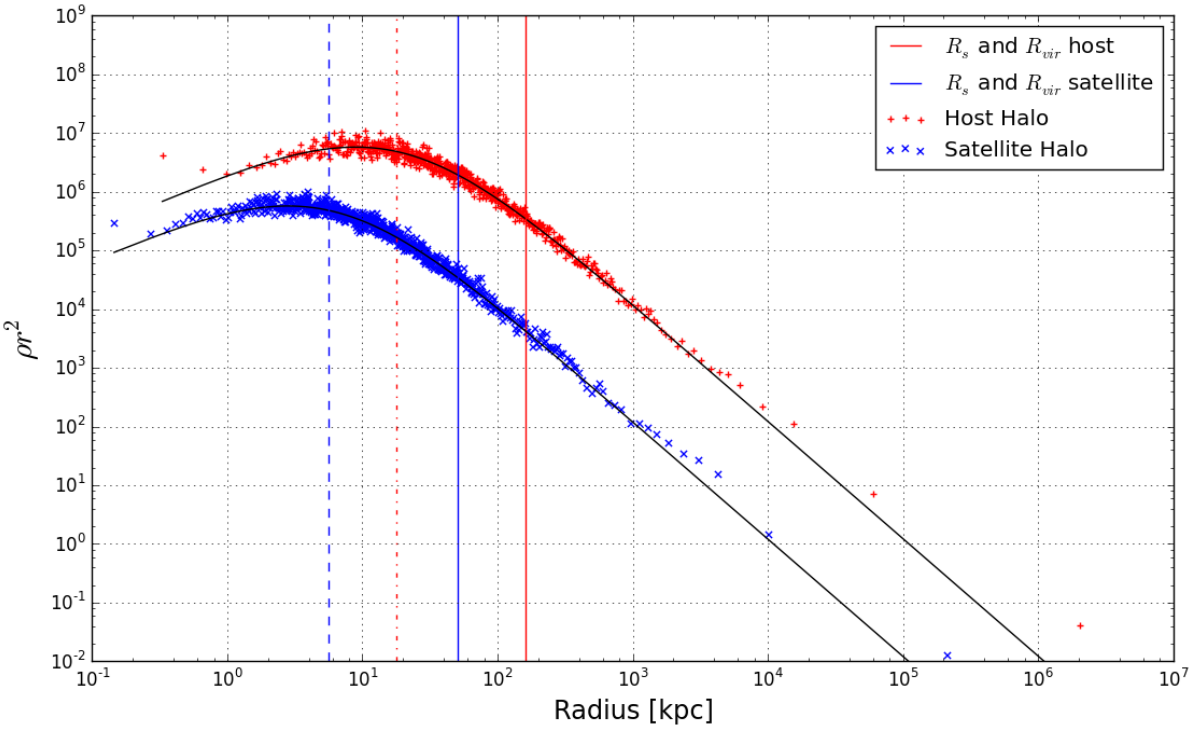

Figure 2.3: Least squares fit (solid) of host (red) and satellite (blue) halos at initial snapshot, in simulation "E10C07MR05". The red points form the density profile of the red halo and the blue points form the density profile of the blue halo. The scale radius for the blue and red halos are shown using dashed and dotted vertical lines, respectively, while the solid vertical lines show the virial radii of each halo, color coded accordingly.

2.4 Satellite Orbits

2.4.1 Orbital Parameters

For spherical systems, an important property its associated circular velocity $v_c(r)$, the speed of a circular orbit at some particular radius r. This can easily be derived, understanding uniform circular motion, $a = v^2/r$ we may then, with the inclusion of mass, relate the velocity to the force such that,

$$\frac{mv_c^2}{r} = m|\mathbf{a}| = |\mathbf{F}(r)| = \frac{d\Phi}{dr} = \frac{GMm}{r^2}$$

so,

$$v_c^2 = \frac{GM(r)}{r} \tag{2.8}$$

Thus, for a Hernquist profiled halo, the circular velocity may be determined using the cumulative mass function.

$$v_c^2 = \frac{GM(r)}{r} = \frac{GM_o}{r}\frac{r^2}{(r+a)^2} = -\frac{r}{(r+a)}\Phi(r) \tag{2.9}$$

The specific energy of such an orbit in an inertial reference frame is then given by,

$$E_{circ} = \Phi(r) + \frac{1}{2}v_c(r)^2 = \Phi(r)\left[1 - \frac{r}{2(r+a)}\right] = -\frac{GM_o}{2}\frac{r+2a}{(r+a)^2} \tag{2.10}$$

The energy of orbits in each simulation was rescaled to the orbital energy of a circular orbit at the virial radius for that simulation. These energies were computed with respect to the most bound particle of the red halo. Noting the relationship between $\Phi(r)$ and $v_c(r)$ in equation 2.9, and defining a concentration parameter, $c \equiv r_{vir}/a$, in similar fashion to NFW, we may develop a useful equation for the energy of a circular orbit at the virial radius.

$$\begin{aligned} E_{vir} &= \Phi(r_{vir}) + \frac{1}{2}v_c(r_{vir})^2 = -\frac{GM_o}{2}\frac{r_{vir}+2a}{(r_{vir}+a)^2} \\ &= -\frac{GM_o}{2(r_{vir}+a)}\frac{r_{vir}+2a}{(r_{vir}+a)} = \Phi(r_{vir})\frac{r_{vir}+2a}{2(r_{vir}+a)} \\ &= \frac{r_{vir}+2a}{2(r_{vir}+a)}\left[-\frac{r_{vir}+a}{r_{vir}}v_c^2(r_{vir})\right] = -(1+1/c)\frac{c+2}{2c+2}v_c^2(r_{vir}) \end{aligned} \tag{2.11}$$

Although the energy of the orbits of the satellites were set to that of a circular orbit at the virial radius, the circularity, η, was given one of two specific values, generating non-circular orbits. The vis-viva equation was used to calculate the corresponding initial velocities.

Let us define a few parameters used in describing the orbits of masses about systems. The main characteristic parameters involved in describing an object's motion in an orbit are its, eccentricity "e", its pericenter "r_p" and its apocenter "r_a", as well as its azimuthal and radial periods, both of which will be described in chapter 3. The eccentricity is essentially a measure of the roundness of the orbit. Making the approximation that the satellite sits in a Keplerian potential, which should be accurate before entering the main body of the host, the eccentricity may be related to the semi-major axis by,

$$a \equiv \frac{L^2}{GM(1+e^2)} \tag{2.12}$$

and the radial distance from the focus of the orbit by,

$$r(\psi) = \frac{a(1+e^2)}{1+e\cos(\Delta\psi)} \tag{2.13}$$

where ψ is the angle of the revolution about the host. The pericenter and apocenter of an orbit are the point closest to, and farthest away from, the host, along the orbit. These values may be defined in terms of the eccentricity such that,

$$r_a = a(1+e) \quad \text{and} \quad r_p = a(1-e) \tag{2.14}$$

Again, these quantities are given purely for reference as they are calculated for a Keplerian potential, rather than the potential generated by these halos.

Let the starting position of the satellite be the apocentre of its orbit, that is to say the point furthest from the center of the potential. Under the assumption of conservation of energy along with angular momentum conservation we may conclude may first equate the energies at apocenter and pericenter.

$$E_a = E_p$$

so,

$$\frac{1}{2}v_a^2 + \Phi_a = \frac{1}{2}v_b^2 + \Phi_b \tag{2.15}$$

We can also equate the angular momentums at both apsides.

$$L_a = L_p$$

so,

$$v_a r_a = v_p r_p$$
$$v_p = \frac{v_a r_a}{r_p} \tag{2.16}$$

Combining these two statements,

$$v_a^2 - v_p^2 = 2(\Phi_p - \Phi_a)$$
$$v_a^2 - [v_a r_a / r_p]^2 = 2(\Phi_p - \Phi_a)$$
$$v_a^2 \left[1 - r_a^2/r_p^2\right] = 2(\Phi_p - \Phi_a) \tag{2.17}$$

Recalling repression 2.4, and re-expressing equation 2.9,

$$v_c^2 \equiv v_{c,vir}^2 = \frac{GM(r_{vir})}{r_{vir}} = \frac{GM_o}{r_{vir}} \left(\frac{r_{vir}}{r_{vir}+a}\right)^2 = (r+a)\Phi(r)\frac{r_{vir}}{(r_{vir}+a)^2} \tag{2.18}$$

We can use relation 2.18 combining with 2.17 and relate the apocentric velocity to the circular velocity through $\kappa = v_a/v_c$.

$$\begin{aligned} v_a^2 = \frac{2(\Phi_p - \Phi_a)}{\left[1 - r_a^2/r_p^2\right]} &= -2v_c^2 \frac{(r_{vir}+a)^2}{r_{vir}} \left[\frac{1}{1 - r_a^2/r_p^2}\right] \left[\frac{1}{r_p + a} - \frac{1}{r_a + a}\right] \\ &= -2v_c^2 \frac{(r_{vir}+a)^2}{r_{vir}} \left[\frac{r_p^2}{r_p^2 - r_a^2}\right] \left[\frac{r_a - r_p}{(r_p+a)(r_a+a)}\right] \\ &= -2v_c^2 \frac{(r_{vir}+a)^2}{r_{vir}} \left[\frac{r_p^2}{(r_p+r_a)(r_p-r_a)}\right] \left[\frac{r_a - r_p}{(r_p+a)(r_a+a)}\right] \\ &= 2v_c^2 \frac{(r_{vir}+a)^2}{r_{vir}} \left[\frac{r_p^2}{(r_p+r_a)(r_p+a)(r_a+a)}\right] \end{aligned}$$

so,

$$(v_a/v_c)^2 = 2\frac{(r_{vir}+a)^2}{r_{vir}} \left[\frac{r_p^2}{(r_p+r_a)(r_p+a)(r_a+a)}\right] \tag{2.19}$$

Let $r_{vir} = 1$ and simplify 2.19,

$$\kappa^2 = (v_a/v_c)^2 = 2(1+1/c)^2 \left[\frac{r_p^2}{(r_p+r_a)(r_p+1/c)(r_a+1/c)}\right] \tag{2.20}$$

Thus, we may determine for any choice of apocenter 'r_a', peridcenter 'r_p', and concentration 'c', the initial velocity of our system 'v_a', relative to the circular velocity at the virial radius 'v_c'.

We may also characterize the satellite's orbit in terms of both its orbital energy relative to the energy of a circular orbit at the virial radius, as well as its angular momentum, relative to the angular momentum of a circular orbit with the same energy. We may define both these quantities as, $\epsilon = E/E_{vir}$, the relative energy parameter and $\eta = L/L_c$, the relative angular momentum parameter (circularity).

We know first,

$$E_{vir} = \Phi(r_{vir}) + \frac{1}{2}v_c(r_{vir})^2 = -(1+1/c)v_c^2 + \frac{1}{2}v_c^2 = -(1/2+1/c)v_c^2 \tag{2.21}$$

while,

$$E_a = \Phi(r_a) + \frac{1}{2}v_a^2 = \Phi_{vir}\frac{r_{vir}+a}{r_a+a} + \frac{1}{2}\kappa v_c^2 \tag{2.22}$$

Now, the relative energy parameter can be expressed as,

$$\begin{aligned}
\epsilon = E_a/E_{vir} &= \left[\Phi_a + \frac{1}{2}v_a^2\right]/E_{vir} = \left[\Phi_{vir}\frac{r_{vir}+a}{r_a+a} + \frac{1}{2}\kappa^2 v_c^2\right]/E_{vir} \\
&= \left[-(1+1/c)v_c^2\frac{r_{vir}+a}{r_a+a} + \frac{1}{2}\kappa^2 v_c^2\right] / \left[-(1/2+1/c)v_c^2\right] \\
&= \frac{(1+1/c)}{(1/2+1/c)}\frac{r_{vir}+a}{r_a+a} - \frac{1}{2}\frac{\kappa^2}{(1/2+1/c)} \\
&= \frac{2(c+1)}{c+2}\frac{r_{vir}+a}{r_a+a} - \kappa^2\frac{c}{c+2} \\
&= \frac{2(c+1)}{c+2}\frac{c+1}{c(r_a/r_{vir}+1/c)} - \kappa^2\frac{c}{c+2}
\end{aligned}$$

Again, in units where $r_{vir} = 1$ and, recalling equation 2.20,

$$\begin{aligned}
\epsilon &= \frac{2(c+1)}{c+2}\frac{c+1}{c(r_a+1/c)} - 2(1+1/c)^2\left[\frac{r_p^2}{(r_p+r_a)(r_p+1/c)(r_a+1/c)}\right]\frac{c}{c+2} \\
&= \frac{2(c+1)^2}{c(c+2)}\frac{1}{(r_a+1/c)} - 2\frac{(c+1)^2}{c^2}\frac{c}{c+2}\frac{1}{(r_a+1/c)}\left[\frac{r_p^2}{(r_p+r_a)(r_p+1/c)}\right]
\end{aligned}$$

so,

$$\epsilon = \frac{2(c+1)^2}{c(c+2)}\frac{1}{(r_a+1/c)}\left[1 - \frac{r_p^2}{(r_p+r_a)(r_p+1/c)}\right] \tag{2.23}$$

For bound orbits, the total energy is always negative and decreases monotonically as $r \to 0$, which implies that $\epsilon < 1$ indicates that $0 > E_a > E_{vir}$. A circular orbit then, with energy E_a, will be less bound than a circular orbit at the virial radius, under the condition $r_e > r_{vir}$.

We may also express the circularity 'η' in terms of the angular momentum of a circular orbit with the same energy as the orbit with energy E_a previously defined. If we know E_a, the energy of the orbit we require, as well as ϵ, we may determine the radius of this new circular orbit. Let this new orbit have radius 'r_e', corresponding to energy E_a such that,

$$\begin{aligned} E_a = \epsilon E_{vir} &= -\frac{GM_o}{r_e + a} + \frac{GM_o}{2}\frac{r_e}{(r_e + a)^2} \\ &= \frac{GM_o}{r_e + a}\left[\frac{r_e}{2(r_e + a)} - 1\right] \\ &= -\frac{GM_o}{r_e + a}\left[\frac{r_e + 2a}{2(r_e + a)}\right] \\ &= -\frac{GM_o}{2}\frac{r_e + 2a}{(r_e + a)^2} \\ &= E_{vir}\frac{(c+1)^2}{c(c+2)}\frac{r_e + 2a}{(r_e + a)^2} \end{aligned}$$

implying,

$$\epsilon = \frac{(c+1)^2}{c(c+2)}\frac{cr_e + 2}{(cr_e + 1)^2} \tag{2.24}$$

We may define,

$$y \equiv \eta\frac{(c+2)}{(c+1)^2} \quad \text{and} \quad x \equiv cr_e + 1$$

such that,

$$\begin{aligned} y &\equiv \frac{x+1}{x^2} \\ x^2 &= y^{-1}(x+1) \\ x^2 - \frac{x}{y} + \frac{1}{y} &= 0 \\ \Rightarrow x = \frac{1}{2y} &\pm \frac{1}{2}\sqrt{1/y^2 + 4/y} \end{aligned} \tag{2.25}$$

Choosing the positive root of this function for obvious reasons we may conclude that,

$$x = \frac{1}{2y}\left[1 + \sqrt{1 + 4y}\right] \quad \text{and} \quad r_e = \frac{1}{2cy}\left[1 + \sqrt{1 + 4y}\right] - \frac{1}{c}$$

Knowing r_e, it is then possible to calculate the corresponding η,

$$\eta = L/L_c = r_a v_a / r_e v_{c,e} = r_a(\kappa v_{c,vir})/r_e v_{c,e} \tag{2.26}$$

Recalling 2.19,

$$v_{c,e} = v_{c,vir}\left[2\frac{(r_{vir}+a)^2}{r_{vir}}\left(\frac{r_p^2}{(r_p+r_a)(r_p+a)(r_a+a)}\right)\right]^{1/2} = v_{c,vir}\left[\frac{r_e}{r_{vir}}\right]^{1/2}\frac{(r_{vir}+a)}{(r_e+a)}$$

This means,

$$\begin{aligned}\eta &= r_a(\kappa v_{c,vir})(r_e v_{c,vir})^{-1}\frac{(r_e+a)}{(r_{vir}+a)}\left[\frac{r_{vir}}{r_e}\right]^{1/2} \\ &= \kappa\frac{r_a(r_e+a)}{(r_{vir}+a)}\left[\frac{r_{vir}}{r_e^3}\right]^{1/2}\end{aligned} \tag{2.27}$$

In practice we may explore an interesting parameter space, setting ϵ, the relative energy parameter, and η, the circularity, to desired values, and working backwards through the previous equations to obtain the more basic orbital parameters in order to generate the desired simulations.

2.5 Output

The output of the simulations from Gadget are as described above. The snapshots are then converted to ASCII files, however, using a C-code which also calculates some basic information about each timesteps. These ASCII snapshots list the identities, locations, and velocities of the MBPs, as well as standard information for every particle. The first columns in the file refer to the particle in the inertial frame: IDs, locations, velocities, masses, group number; while subsequent columns give particle information relative to both halos: radii relative to both halo centers, velocities relative to both halo velocities, thermal kinetic energies in both halo frames of reference, and the potential energy contributions of each halo. Any subsequent information is obtained from this initial data, using a secondary analysis code.

Chapter 3

Orbital Dynamics

If the two halos were point sources or rigid bodies, the total energy of either halo would remain constant throughout, and no significant exchange of energy would occur between them, however, simulated halos are large extended structures composed of many bodies. As a result, when halos undergo merger, two processes significantly modify both the orbits and the energetics of the halos involved. These processes are know as tidal stripping and dynamical friction; the former of which is simply the pruning of mass from the satellite halo, while the latter is the process by which the satellite's orbital energy is re-distributed, by means of a frictional drag force, into the host halo causing the satellite to sink into its center. The transfer of this orbital energy occurs such that the host halo becomes "heated", and its thermal kinetic energy is increased.

3.1 Timescales

It is of primary importance to understand the timescales for various interactions, as these should relate directly to the timescale involved in either heating or mixing the halos. Although many of the following timescales resemble each other, their physical significance differs.

3.1.1 The Crossing Time

The crossing time may simply be defined as the typical time for a member of a system to cross that system. Letting v be the typical velocity of an object in a system of radius R,

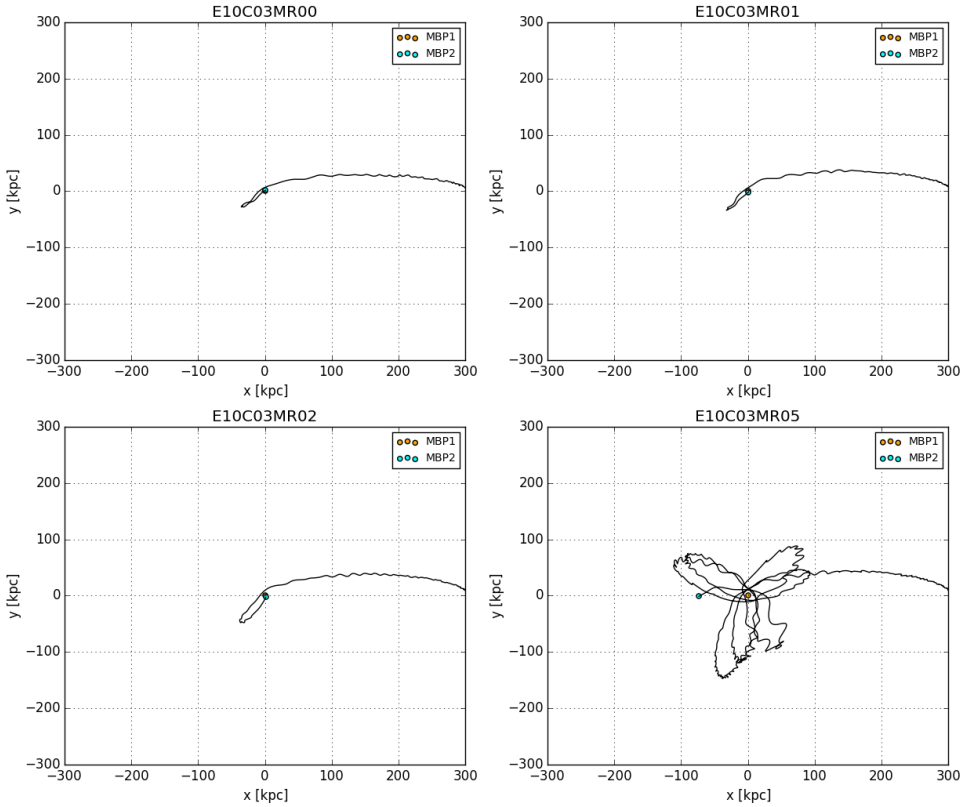

Figure 3.1: Orbital decay of satellites on orbits of initial circularity $\eta = 0.3$, for primary-secondary mass ratios of 1:1 (top left panel), 1:2 (top right panel), 1:4 (bottom left panel), and 1:32 (bottom right panel). The satellite position is taken to be that of the most bound particle.

we may define the crossing time as,

$$t_{crossing} = \frac{R}{v} \tag{3.1}$$

3.1.2 The Relaxation Time

The relaxation time is defined as the approximate time for a typical object to interact with other objects within a system such that its velocity increases by order $\Delta v/v \approx 1$. We will derive the relaxation time as in Binney & Tremaine (1987)[5]. Let an object of mass m be traveling through a system with N other bodies, also of mass m. Let us assume that two-body interactions create change in velocity δv, such that $|\delta \mathbf{v}|/v \ll 1$. We will make

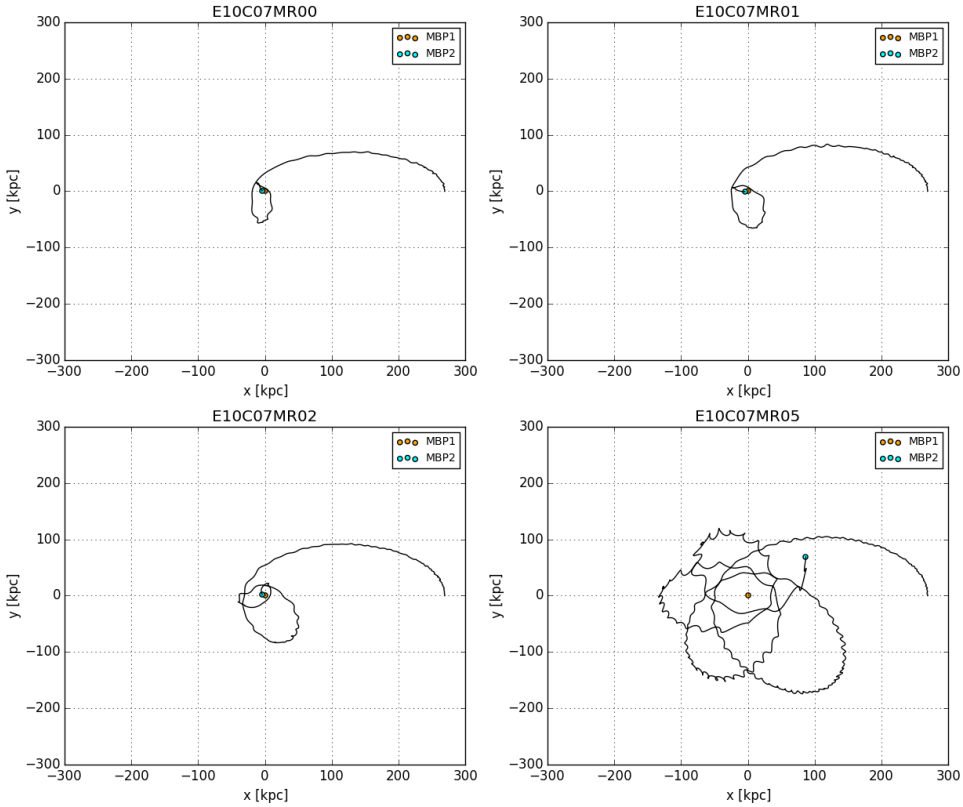

Figure 3.2: Orbital decay of satellites on orbits of initial circularity $\eta = 0.7$, for primary-secondary mass ratios of 1:1 (top left panel), 1:2 (top right panel), 1:4 (bottom left panel), and 1:32 (bottom right panel). The satellite position is taken to be that of the most bound particle.

another assumption, that the perturbing object is almost stationary during the interaction. Assuming a straight line trajectory we may calculate the $\delta\mathbf{v}_\perp$ component of $\delta\mathbf{v}$.

$$\begin{aligned} |\mathbf{F}_\perp| =& \frac{Gm^2}{r^2}\cos\theta = \frac{Gm^2}{b^2+x^2}\cos\theta = \frac{Gm^2 b}{(b^2+x^2)^{3/2}} \\ &\simeq \frac{Gm^2}{b^2}\left[1+\left(\frac{vt}{b}\right)^2\right]^{-\frac{3}{2}} \end{aligned} \tag{3.2}$$

where θ is the angle between the incoming object and the vertical perpendicular to its motion. One can also define the force as

$$m|\dot{\mathbf{v}}| = |\mathbf{F}_\perp| \tag{3.3}$$

which implies,

$$\frac{dv}{dt} = \frac{Gm}{b^2}\left[1 + \left(\frac{vt}{b}\right)^2\right]^{-\frac{3}{2}} \tag{3.4}$$

Solving the differential by substitution using $s = vt/b$, one can write,

$$dv = \frac{Gm}{b^2}\int_{-\infty}^{\infty}\left[1 + s^2\right]^{-\frac{3}{2}} ds = \frac{2Gm}{bv} \tag{3.5}$$

Let the object of interest be traveling through a system with surface density $\Sigma \sim N/\pi R^2$, where R is the characteristic radius of our system. This implies that the number of encounter over one crossing is given by,

$$\delta n = 2\pi\Sigma b db = \frac{2N}{R^2} b db \tag{3.6}$$

with impact parameter b to $b + db$, and each encounter adding the effect $\delta\mathbf{v}_\perp$. Since all perturbations are random the vector sum of these contributions, the net perpendicular force is null. However, summing the squares, we may define

$$\delta v_\perp^2 = \sum_0^{\delta n} |\delta\mathbf{v}_\perp|^2 = \delta n \cdot |\delta\mathbf{v}_\perp|^2 = 8N\left(\frac{Gm}{Rv}\right)^2 \frac{db}{b} \tag{3.7}$$

Of course, this only works for $|\delta\mathbf{v}_\perp|/v \ll 1$. An exception would be very strong two-body encounters, characterized by $b \lesssim b_{min} \equiv Gm/v^2$. Integrating over all impact parameters in order to obtain the total change in velocity, b will go from b_{min} to R.

$$\Delta v_\perp^2 = \int_{b_{min}}^{R} 8N\left(\frac{Gm}{Rv}\right)^2 \frac{db}{b} = 8N\left(\frac{Gm}{Rv}\right)^2 [\ln R - \ln b_{min}] \tag{3.8}$$

Let $\Lambda = R/b_{min}$ so that,

$$\Delta v_\perp^2 = 8N\left(\frac{Gm}{Rv}\right)^2 \ln\Lambda \tag{3.9}$$

Now, for a virialized structure, we can replace the radius in terms of the velocity,

$$v^2 \simeq \frac{GNm}{R} \tag{3.10}$$

The change in velocity may now be written as,

$$\begin{aligned} \Delta v_\perp^2 &= 8N \left(\frac{Gm}{v}\right)^2 \ln\Lambda \left(\frac{v^2}{GNm}\right)^2 \\ \Rightarrow \ \frac{\Delta v_\perp^2}{v^2} &= \frac{8}{N}\ln\Lambda \end{aligned} \tag{3.11}$$

Thus, if v^2 changes by $\Delta v_\perp^2$ at every crossing, the number of crossings required for order unity change is written as,

$$\begin{aligned} \frac{\Delta v_\perp^2}{v^2} n_{relax} &= 1 \\ \Rightarrow n_{relax} &= \frac{N}{8\ln\Lambda} \end{aligned} \tag{3.12}$$

Finally, we may express relaxation time in terms of the crossing time as written previously.

$$t_{relax} = n_{relax} \times t_{crossing} = \frac{N}{8\ln\Lambda}\frac{R}{v} \tag{3.13}$$

3.1.3 The Dynamical Time

The dynamical time is defined as the time it would take for an orbiting body to make its way halfway across the system when released from rest, if the system were spherically homogeneous, with mean density ρ. We can write the circular velocity as:

$$v_c^2 = \frac{GM(r)}{r} = \frac{4\pi G\rho}{3} r^2 \tag{3.14}$$

and so we can also define the period of such an orbit,

$$T = \frac{2\pi r}{v_c} = \sqrt{\frac{3\pi}{G\rho}}. \tag{3.15}$$

The equation of motion of a test particle at rest at radius r is given by,

$$|\ddot{\mathbf{r}}| = -\frac{GM(r)}{r^2} = -\frac{4\pi G r}{3}\rho \tag{3.16}$$

which is the equation of motion of a harmonic oscillator that has angular frequency $2\pi/T$. Thus the period is actually independent of the initial radius r_i where the particle is at rest, and as a result, the dynamical is simply one fourth of the period, or

$$t_{dynamical} = \frac{T}{4} = \sqrt{\frac{3\pi}{16G\rho}}. \tag{3.17}$$

3.1.4 Orbital Periods

Non-circular orbits in a general spherical potential will not return to the same location after a single cycle but rather will trace a rosette pattern through apsidal precession. In general potentials, the radial and azimuthal periods, that is the time it takes to return to the same radial distance such that $\Delta d = 0$ and the time it takes to return to the same angle so that $\Delta\phi = 2\pi$, are not equal. We may define the radial period "T_r" generally as,

$$T_r = 2\int_{r_a}^{r_p} \frac{dr}{\sqrt{2[E - \Phi(r)] - L^2/r^2}} \tag{3.18}$$

This may be related to the azimuthal period through,

$$T_\psi = \frac{2\pi}{|\Delta\psi|} T_r \tag{3.19}$$

We focus on the radial period because it determines when the satellite passes through pericentre, where it is tidally stripped and/or interacts with the center of the main halo. The azimuthal period is of no importance sin the main system is spherically symmetric.

3.2 Dynamical Friction

When traveling in a background particle field, a massive particle creates a wake. Through the net effect of two-body encounters, the combined system of the satellite along with the smaller masses it encounters move towards equipartition of the orbital energy carried in by the satellite. This causes the satellite to fall into the host towards the center of its potential well. The overall interaction between the background particles and the satellite generates a form of gravitational drag called dynamical friction. The dynamical friction formula developed by Chandrasekhar (1943) [7] may be written as,

$$\mathbf{F}_{DF} = -\frac{4\pi \ln(1+\Lambda^2) G^2 \rho M^2}{v_M^3} \left[\mathrm{erf}(X) - \frac{2X}{\sqrt{\pi}} \exp\left(-X^2\right)\right] \mathbf{v}_M \tag{3.20}$$

with,

$$X \equiv \frac{|\mathbf{v}_M|}{(\sqrt{2}\sigma)} \quad \text{and} \quad \Lambda \equiv \frac{b_{max} V_o^2}{G(M+m)}$$

where M is the mass of the satellite, V_o is its velocity, m is the mass of a background particle, and ρ is the local mass density. Λ is the Coulomb logarithm for the halo, the

factor by which small-angle collisions are more effective than large-angle collisions; b_{max} is defined as the largest impact parameter that need be considered, and σ is the local velocity dispersion at the satellite center[5]. Of course, as we are dealing with *two* extended bodies, both of which are non-uniform structures, this treatment is incomplete; *sigma* as well as ρ may vary across the satellite. As stated in Taylor & Babul (2001)[39], b_{max} is a rather ambiguous quantity; this quantity, for any finite system, is typically taken to be the characteristic scale of the system. Quinn & Goodman (1986) used the half-mass radius for a spherically symmetric system, while Binney & Tremaine (1987) used the distance over which the density changes by a factor of two. Other choices also include the tidal radius of the halo and the distance between the host and satellite centers Colpi et al. (1999). For simplicity, the radial distance between the satellite and host halo was chosen as an appropriate value for b_{max}.

The timescale for this interaction may be estimated as in Binney & Tremaine (1987) section 7.1, pg. 427. Assuming a body on circular orbit about the host halo at some radius r_i is being dragged in to the center of the host by the dynamical friction force, the time to reach this center from its initial radius r_i, is given by the $t_{DF}(r_i)$ estimated below.

3.2.1 Timescale

For simplicity, we derive the timescale for decay in an isothermal sphere with a density profile given by:

$$\rho(r) = \frac{v_c^2}{4\pi G r^2}. \tag{3.21}$$

The corresponding velocity dispersion is:

$$\sigma = \frac{v_c}{\sqrt{2}} \tag{3.22}$$

where v_c is the circular velocity. The dynamical friction of an object being dragged into the host halo by force F may be written using equation 3.20 such that,

$$\begin{aligned} |\mathbf{F}_{DF}| &= -\frac{4\pi \ln(1+\Lambda^2) G^2 M^2}{v_M^3} \left(\frac{v_c^2}{4\pi G r^2}\right) \left[\mathrm{erf}(1) - \frac{2}{\sqrt{\pi}} \exp(-1)\right] \mathbf{v}_M \\ &= -0.428 \ln\Lambda \frac{GM^2}{r^2} \end{aligned} \tag{3.23}$$

Because the satellite is on a circular orbit, the force is tangential to its path at any point and so the satellite loses angular momentum per unit mass at a rate

$$\frac{dL}{dt} = \frac{Fr}{M} \approx -0.428 \frac{GM}{r} \ln\Lambda \tag{3.24}$$

The rate of loss of angular momentum is actually proportional to the rate of change of the radius and as a result, the speed of the satellite is v_c even as it is dragged into the host, its specific angular momentum continues to be $L = rv_c$ until it reaches the center. We may plug this result into 3.24 and solve the resulting differential equation,

$$\begin{aligned} v_c \frac{dr}{dt} &= -0.428 \frac{GM}{r} \ln \Lambda \\ \Rightarrow r \frac{dr}{dt} &= -0.428 \frac{GM}{v_c} \ln \Lambda \\ \Rightarrow \int_{r_i}^{0} r dr &= -0.428 \frac{GM}{v_c} \ln \Lambda \int_{0}^{t_{DF}} dt \end{aligned}$$

such that the resulting dynamical friction timescale is given by,

$$t_{DF}(r) = \frac{1.17}{\ln \Lambda} \frac{v_c r^2}{GM} \tag{3.25}$$

This timescale is actually similar to the dynamical time, modulo a factor dependent on the mass of the satellite, and b_{max} in the case of dynamical friction.

It is evident upon understanding the concept of dynamical friction that the mass of the satellite is of great importance. Unlike in the preceding derivation, however, the mass of the satellite is generally not constant, and the mass loss caused by tidal stripping is a non-negligible effect. As $F_{dyn} \propto M_{sat}^2$, the instantaneous mass and associated loss becomes important to accurately determine the drag force, and thus the energy gained by the host during the interaction.

3.3 Mass Stripping

The large scale gravitational field of the host system prunes the satellite system of mass during each encounter. A tidal radius may be estimated such that at any given moment during an encounter, material outside of this radius is unbound from the satellite. The tidal radius depends ultimately on four factors: the potential of the host, the potential of the satellite, the orbit of the satellite and the orbits of the objects composing the satellite (see Von Hoerner (1957), King (1962), Toomre & Toomre (1972), Read (2006)).

3.3.1 The Jacobi Radius

We may model the tidal radius using the simple case of a satellite of mass m in circular orbit about a host halo of mass M at radius some radius D. We may then define the

angular speed about their mutual center of mass to be,

$$\Omega = \sqrt{\frac{G(M+m)}{D^3}} \tag{3.26}$$

In a co-rotating coordinate system centered on the center of mass of the whole system, energy and angular momentum are not conserved individually, but there is a conserved quantity known as the Jacobi integral, E_J. In this rotating coordinate system, the equations of motion is given by a combination of the gradient of the potential, the Coriolis force, and the centrifugal force as,

$$\begin{aligned} \frac{d^2\vec{r}}{dt^2} &= \vec{F}_{gravity} + \vec{F}_{coriolis} + \vec{F}_{centrifugal} \\ &= -\Delta\Phi - 2(\vec{\Omega} \times \frac{d\vec{r}}{dt}) - \vec{\Omega} \times (\vec{\Omega} \times \vec{r}) \end{aligned} \tag{3.27}$$

Taking the the dot product of this equation with $d\vec{r}/dt$, it can be shown that [5],

$$\frac{dE_J}{dt} = 0 \tag{3.28}$$

with,

$$\begin{aligned} E_J &= \frac{1}{2}\left(\frac{d\vec{r}}{dt}\right)^2 + \Phi(\vec{x}) - \frac{1}{2}|\vec{\Omega} \times \vec{r}|^2 \\ &= \frac{1}{2}\left(\frac{d\vec{r}}{dt}\right)^2 + \Phi_{eff}(\vec{x}) \end{aligned} \tag{3.29}$$

In a steadily rotating potential such as this, moving along any orbit the Jacobi integral is constant. As such, an object whose Jacobi integral E_J may not cross into a region in which $\Phi_{eff} > E_J$. This implies that for a particular Jacobi integral, $\Phi(\vec{x}) = E_J$ sets the boundary of a so-called zero velocity surface. In the region nearby either object, surfaces of constant E_J concentrically surround the respective systems. This is not true at larger radii, where the zero velocity surface surrounds both the host and satellite. We can then define a limiting radius r_J, to be the largest radius before which the zero velocity surface begins to surround both systems. Mathematically, this radius is the distance between the satellite and the saddle point of Φ_{eff}. Thus, particles at such radii, where the zero velocity surface surrounds both the host and satellite is free to move between the two, while an object within r_J is limited to its respective system.

We may set this rotating frame such that the positions of the host and satellite lie purely along the x-axis of our coordinate system. The positions of the host and satellite is

given by,

$$\vec{x}_M = \left(-\frac{Dm}{M+m}, 0, 0\right) \quad \text{and} \quad \vec{x}_m = \left(\frac{DM}{M+m}, 0, 0\right)$$

as such, the saddle point will be found a distance r_J away from the center of the satellite, at the point $\vec{x}_J = (\vec{x}_m - r_j, 0, 0)$. This saddle point implies,

$$\left.\frac{\partial \Phi_{eff}}{\partial x}\right|_{x=x_J} = 0 \tag{3.30}$$

We may approximate the two bodies to be point sources at any given moment in time, separated by a distance D. The resulting effective potential is given by,

$$\Phi_{eff}(\vec{x}) = -G\left[\frac{M}{|\vec{x}-\vec{x}_M|} + \frac{m}{|\vec{x}-\vec{x}_m|} + \frac{1}{2}\frac{M+m}{D^3}|\hat{e}_z \times \vec{x}|\right] \tag{3.31}$$

Taking the derivative of 3.31, and equating it to zero, knowing that this condition is satisfied at the saddle point $\vec{x}_J$, we may develop an equation to determine the value of r_J.

$$\left.\frac{\partial \Phi_{eff}(\vec{x})}{\partial x}\right|_{x=x_m-r_J} = -G\left[\frac{M}{D^2(1-r_J/D)^2} - \frac{m}{r_J^2} - \frac{M}{D^2} + \frac{(M+m)}{D^3}r_J\right] = 0 \tag{3.32}$$

Under the approximation that $r_J << D$, we may use a Taylor series expansion of $(1 - r_J/D)^{-2}$ to first order in r_J/D to compute the Jacobi radius.

$$\begin{aligned} 0 &= \frac{M}{D^2}\left(1 + \frac{2r_J}{D}\right) - \frac{m}{r_J^2} - \frac{M}{D^2} + \frac{(M+m)}{D^3}r_J \\ &= \frac{2r_J}{D^3} + \frac{(M+m)r_J}{D^3} - \frac{m}{r_J^2} \\ &= \frac{2r_J^3}{D^3} + \frac{(M+m)r_J^3}{D^3} - m \end{aligned}$$

Such that,

$$r_J = D\left[\frac{m}{3M+m}\right]^{\frac{1}{3}} \tag{3.33}$$

The Jacobi radius, used as the tidal radius, becomes a useful tool for determine the boundedness of an object within the satellite. This radius, however, proves to be inherently inexact due its aspherical nature; no single radius may fully characterize the limiting zero velocity surface. We have also made a number of simplifying assumptions in our derivation that will cause the real boundary between bound and unbound particles to differ from this

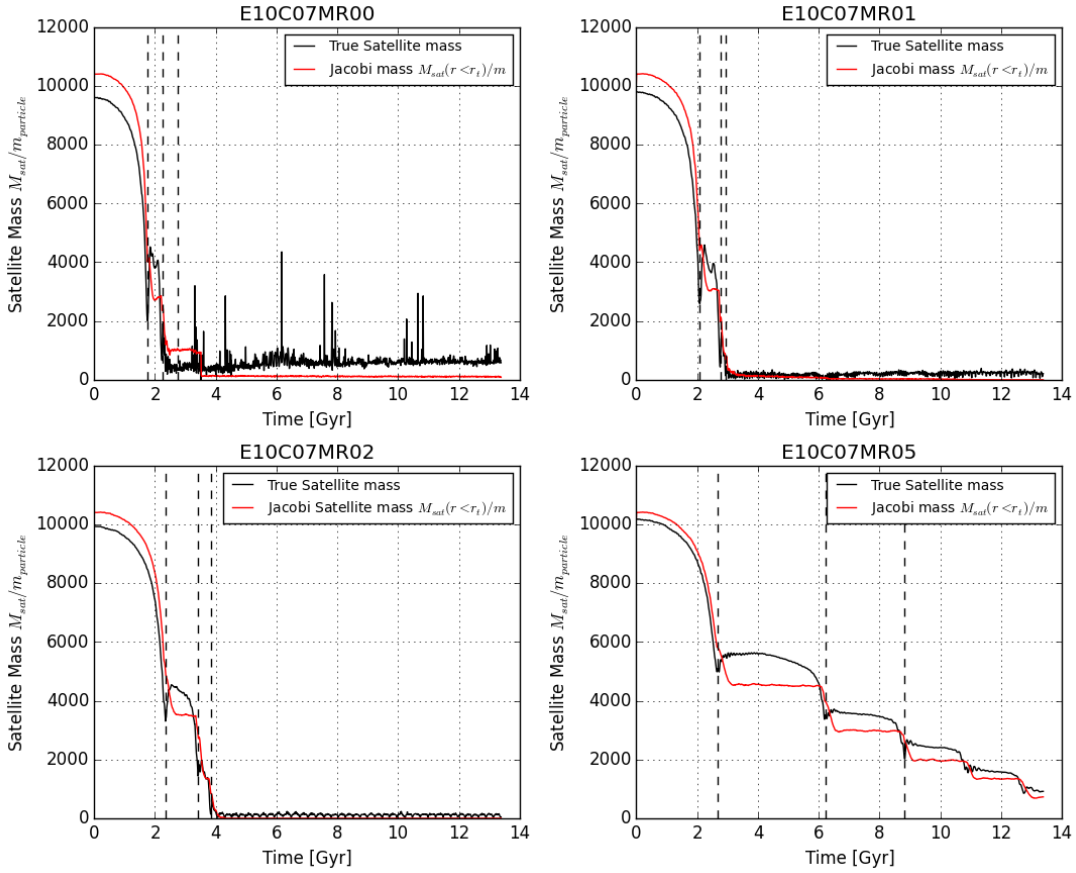

Figure 3.3: Tidal stripping of satellite for simulations with circularity $\eta = 0.3$. Comparison between the estimation of the mass of the satellite using the Jacobi radius (red) and the satellite mass calculated checking boundedness using energy (black).

radius the host and satellite bodies are not circularly rotating point masses but rather, are large extended structures on non-circular orbits. There exists no analog of the Jacobi integral for objects moving in non-static potentials [5].

Another derivation of this idealised tidal radius is described in Taylor & Babul (2001) [39] and was developed by King (1962). It reformulates the equations of motion as a function of the orbital frequency to derive a simple form for this radius, noting the fact that the Jacobi tidal radius cannot truly be defined for non-circular orbits. Once more the saddle point of the potential field between the host and satellite will yield the approximate

maximum radius at which stars will be stripped. This tidal radius is given by,

$$r_t = \left[\frac{GM_{sat}}{\omega^2 - d^2\Phi/dr^2}\right]^{\frac{1}{3}} \tag{3.34}$$

and more accurately reflects the actual tidal radius, taking into account the extended nature of the halo through the potential.

3.3.2 Towards a More Realistic Model of Mass Loss

Based on the tidal radius definition of King (1962), Taylor & Babul (2001)[39] developed a simple yet robust stripping condition in terms of the relative densities of the host and satellite. The tidal limit R_t within which the mean density of the satellite $\bar{\rho}$, exceeds the mean density of the host interior to the orbital radius by a factor η such that,

$$\bar{\rho}_{sat}(< R_t) = \eta\bar{\rho}_{host}(< r) \tag{3.35}$$

where

$$\begin{aligned}\eta &\equiv \frac{\bar{\rho}_{sat}(< R_t)}{\bar{\rho}_{host}(< r)} = \frac{r^3}{R^3}\frac{M_{sat}}{M_{host}(< r)} \\ &= \frac{r^3}{GM(< r)}\left[\omega^2 - \frac{d^2\Phi}{dr^2}\right] = \frac{\omega^2}{\omega_c^2} - \frac{1}{\omega_c^2}\frac{d^2\Phi}{dr^2}\end{aligned} \tag{3.36}$$

We may note that the η parameter described here is not the circularity parameter. Taylor & Babul (2001) developped a simple method for accurately determining the mass of the satellite over time using the tidal radius. The mass lost was assumed to be stripped from the satellite over some fiducial timescale (taken by Taylor and Babul (2001) as the instantaneous orbital time t_{orb}). At every timestep and they removed a fraction of the mass outside the tidal radius corresponding to the fraction of time between snapshots to the orbital period. This process was repeated at each timestep, proceeding until the satellite was completely disrupted.

Through the combined presence of both physical phenomena explained above, the dynamical friction acting on the satellite mass which has not been stripped, energy is expected to flow from the in-falling satellite into the host halo. Whether this injection of energy is purely local is not yet known. However, it is the goal of this study to understand how the heating from the satellite affects the radial expansion of the host, observing in detail the behavior of the scale radius as well as the changes occurring to the particles within it. This heating will be discussed in chapter 4.

Chapter 4

Heating

One of the main goals of running the simulations described in Chapter 3 was to measure the heating of the host as a function of satellite mass and orbital circularity. We may define heating simply as the dumping of energy from the satellite into the host. Two possible mechanisms for the exchange of energy are present within these systems, relaxation trhough two-body interactions and dynamical friction. In reality relaxation is irrelevant as dark matter particles have zero-cross sections, however, the particles used in simulation do have non-zero cross sections and are therefore susceptible to relaxation. Using equation 3.13 the relaxation time for these systems is on the order of $\sim$ 1000 Gyrs, while at $\sim$ 14 Gyrs the runtime of our simulation limit the effects of relaxation such that they are negligible. Dynamical friction, the drag force caused by a satellite moving through a background density field must be the source of heating, dumping the orbital energy of the satellite in our simulations into the thermal component of the host. The way one can measure the heating of the halo is to measure the drop in concentration. As explained previously, the concentration parameter is formulated in terms of the virial radius and the scale radius. The virial radius is a cosmologically driven quantity, being defined solely by the total mass of the halo and the background density. Its is simple to understand how it changes, while the changes to scale radius will be more complex. In this chapter, we will study changes in the scale radius as a proxy for heating, as changes in the thermal component will result in change in the average radius of each particle being heated. This will be key in understanding what the final halo will look like.

4.1 Method

For our purposes, the particles from the host and satellite halos are considered distinct and labeled *red* and *blue* accordingly. The host/satellite distinction becomes meaningless for one-to-one mergers, and so the color-coding of the halos provides an unambiguous understanding of which halo in the simulation is being discussed. From this, it is possible to determine the energetic characteristics of each system separately and notice any red- or blue-dependent trends. The properties of the total combined system will also be analyzed in order to relate the final halo, which should be the relaxed final state of the merger, back to the characteristics of the red host halo.

Viewing the halo in radius and energy shells will allow the characterization of where the most heating is occurring and an additional way of observing the timescale for the changes in scale radius to occur. At each timestep, the red halo particles were grouped into twenty radial bins, and their average properties were measured collectively in each bin. The average radius of each of these bins was computed in order to visualize the average movement of each shell throughout the merger. To accompany this, the average energy of the particles in each of these bins was also computed to see if any particular trends would emerge. The cumulative mass distribution for the whole halo was also determined at each timestep, to visualize at each pericentric passage in order to see the heating through the movement of mass from the inner regions of the halo.

The scale radii for both simulations at the last snapshot were collected from the simulations and can be seen in table 4.1.

Mass Ratio	$r_{s,red}$ [kpc]	$r_{s,blue}$ [kpc]	η	$r_{s,total}(t_{final})$ [kpc]
1:1	17.787	17.794	0.7	26.537
			0.3	26.405
1:2		14.123	0.7	23.838
			0.3	23.676
1:4		11.209	0.7	21.959
			0.3	21.663
1:32		5.605	0.7	18.205
			0.3	18.162

Table 4.1: Relevant scale radii for all simulations taken at $t_{final} \approx 13.4$ Gyrs.

4.2 Analysis in Shells: Mean Radius and Mean Energy

It is evident from figure 4.1 that the outer shells are significantly more perturbed than the core of the halo, due to the nature of the gravitional potential well being more shallow at the outer edges of the halo. The mean radius of each shell here, acts as a proxy for measuring the heating; any increase in energy of an individual particle leads to a kick in its orbit, increased velocity and larger radius, thus if the shell is heated on average, the average radius will also increase. The radius at which any individual particle may find itslef after being heated depends non-linearly on the amount of energy deposited and the initial radius of the particle. In truth relating the amount of energy gained to the final radius of any group of particles is highly non-trivial. It is sufficient to say that the average distance of particles from the center of the halo increases on average, as the kinetic energy gained by the particles allows them to travel on larger orbits.

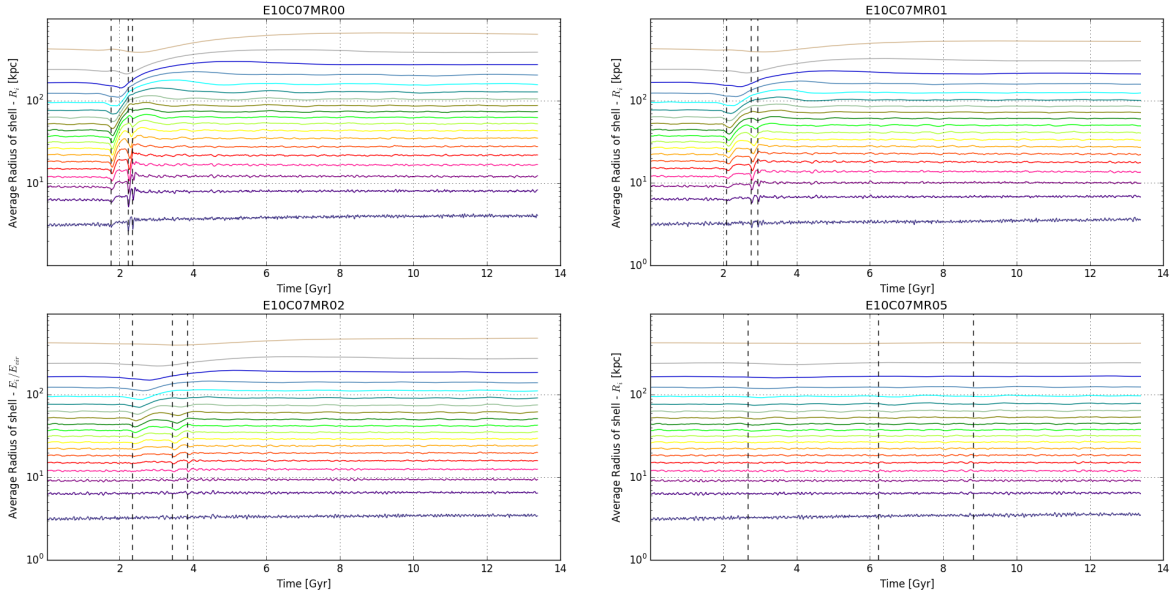

Figure 4.1: Average radius of particles in twenty concentric bins for all simulations with circularity $\eta = 0.7$. Top left panel shows the results for a mass ratio of 1:1; top right panel shows the results for a mass ratio of 1:2; bottom left panel shows the results for a mass ratio of 1:4; bottom right panel shows the results for a mass ratio of 1:32.

We see that at every pericentric passage the mean radius of the particles in each respective shell tends to increase; each layer in the host is being heated as each layer receives

energy from the satellite. The first pericentric passage appears to be the dominant period during the merger in which energy is imparted to the red particles, while the third pericentric passages appears to be the last visually discernable perturbation.

It is interesting to note that the heating of the outer shells takes longer than that of the inner regions, while the inner shells react over an relatively small timescale and stabilize, probably due to how bound these particles are within the halo. The outer shells grow in radius slowly over a few gigayears, and only have one significant interaction with the blue halo. Additionally, small dips in the radii of the shells may be seen shortly before every passage. This is most likely the dragging in of material as the blue halo crosses the shell.

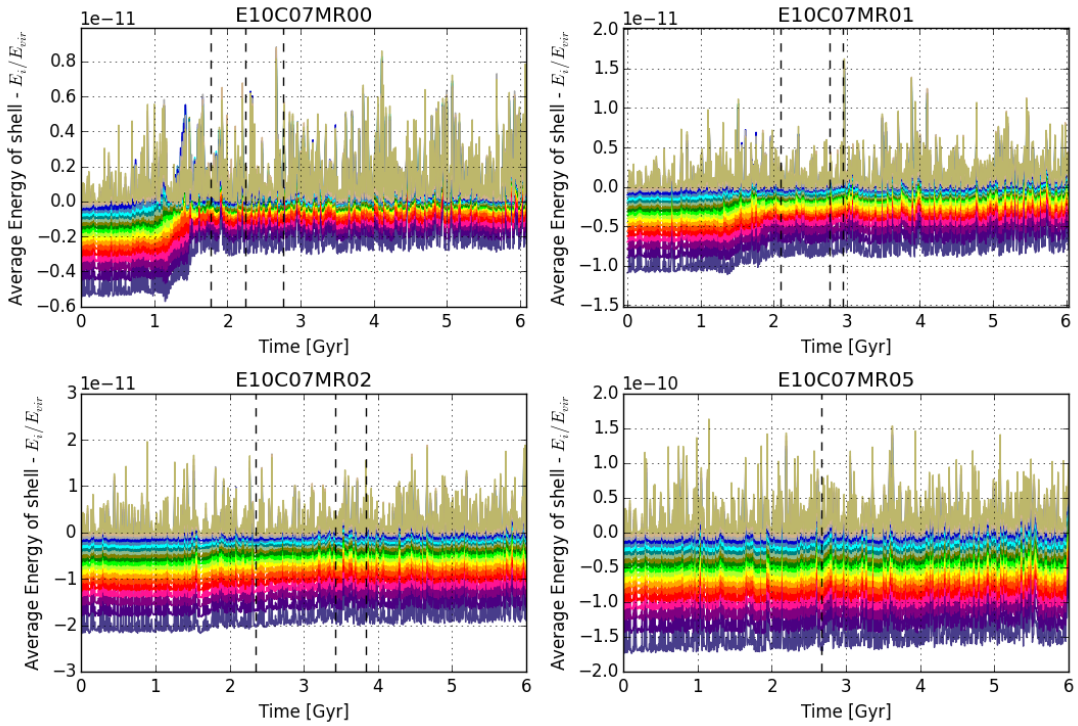

Figure 4.2: Average energy of particles in twenty concentric bins for all simulations with circularity $\eta = 0.7$. Top left panel shows the results for a mass ratio of 1:1; top right panel shows the results for a mass ratio of 1:2; bottom left panel shows the results for a mass ratio of 1:4; bottom right panel shows the results for a mass ratio of 1:32.

Looking at the energy shells neglecting the potential contribution from the satellite in figure 4.2, we may determine that halo is actually heated unevenly during the merger. The total energy of the inner shells is increased significantly, while the outer shells on average tend to increase only marginally in energy.

4.3 Cumulative Mass Distribution

An equally interesting way to view the heating is to measure the changes to the cumulative mass distribution. Over every pericentric passage the mass interior to an increasingly receding radius is disturbed. As figure 4.3 demonstrates, every pericentric passage of the satellite is observed to drag material outward. These changes should also be reflected in

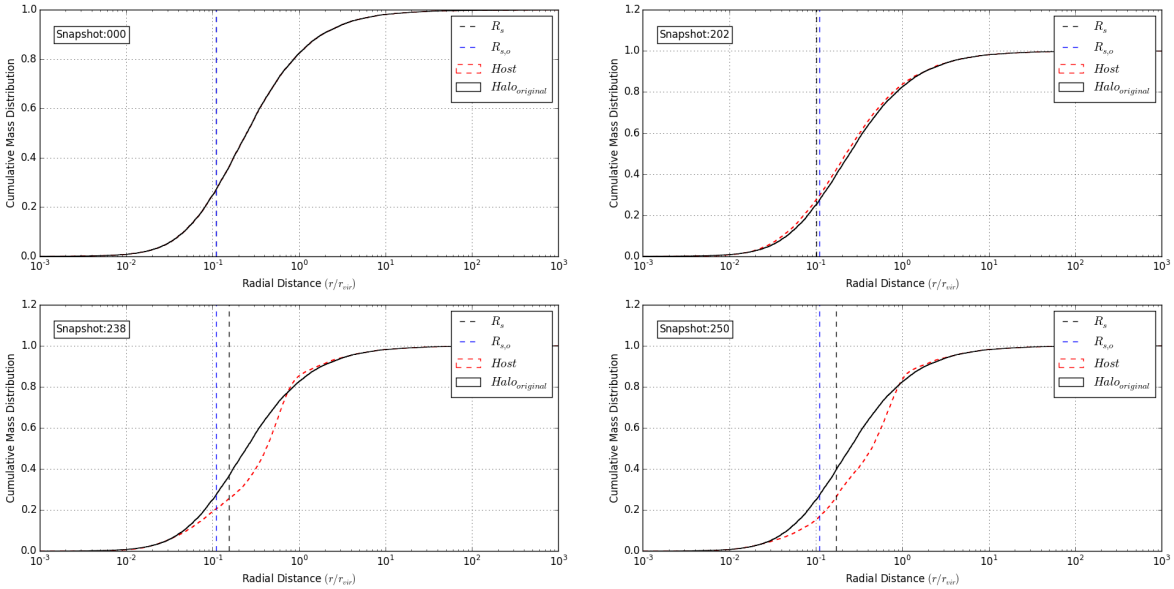

Figure 4.3: The cumulative mass distribution for the initial conditions (top left), first percicentric passage (top right), second pericentric passage (bottom left) and, third pericentric passage (tbottom right) demonstrating the heating of particles in the host halo of simulation "E10C03MR00".

the density profile, we may be able to distinguish where the mass is being pulled and where it ends up. The question of whether or not the resulting halo has a Hernquist profile is also relevant here. In figure 4.4, we choose to plot the quantity $\rho(r)r^2$ since it highlights deviations from the Hernquist profile quite well. In figure 4.4 we see in the second panel the formation of a higher density "lump" caused by the interaction of the two halos. As the second pericentric passage occurs a second "lump" of mass is formed near the exterior of the scale radius. This seems to suggest that the blue halo not only heats the red one, but also drags material from the inner regions outward. The red halo final states for each simulation were well matched to Hernquist profiles, having similar χ^2 values to the initial state fits.

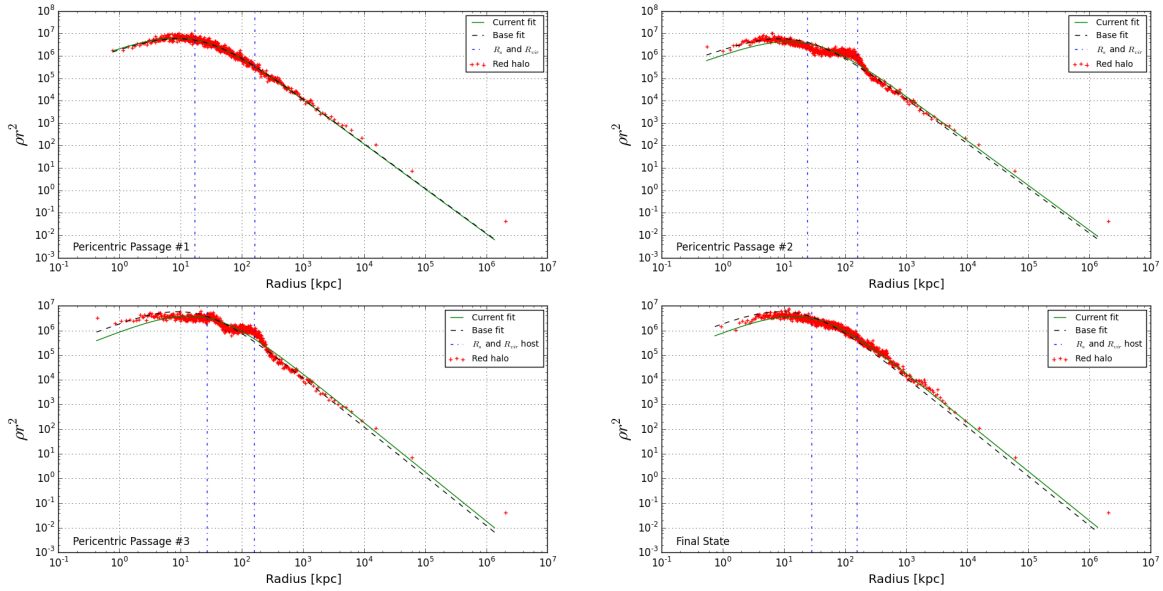

Figure 4.4: A plot of the quantity $\rho(r)r^2$ versus radius for the initial conditions (top left), first percicentric passage (top right), second pericentric passage (bottom left) and, third pericentric passage (bottom right), demonstrating the density changes in the profile and the resulting changes to the scale radius for the host halo of simulation "E10C07MR00".

4.4 The Scale Radius

Figure 4.5 illustrates the changes in the scale radius "a", for each simulation with circularity $\eta = 0.3$. A relationship between the increase in scale radius and host-satellite mass ratio is obvious and merits investigation. The scale radius is directly dependent on the mass of the given halo, characterizing the radius containing one fourth of the total mass of the halo for a Hernquist profile[15]. As a result, during merger, it may also be interesting to measure the change in this quantity with respect to the mass brought into the scale radius.

4.4.1 Mass dependence

Plotting the change in scale radius as a function of the merger mass ratio in figure 4.6 suggests that the form of the relationship between these two parameters is non-linear. Presumably, as the mass ratio goes to zero, the amount of disturbance in the scale radius will also become negligible; we can then assume that any mass-ratio dependence will pass through the zero coordinate. It appears that the change in scale radius could be a power

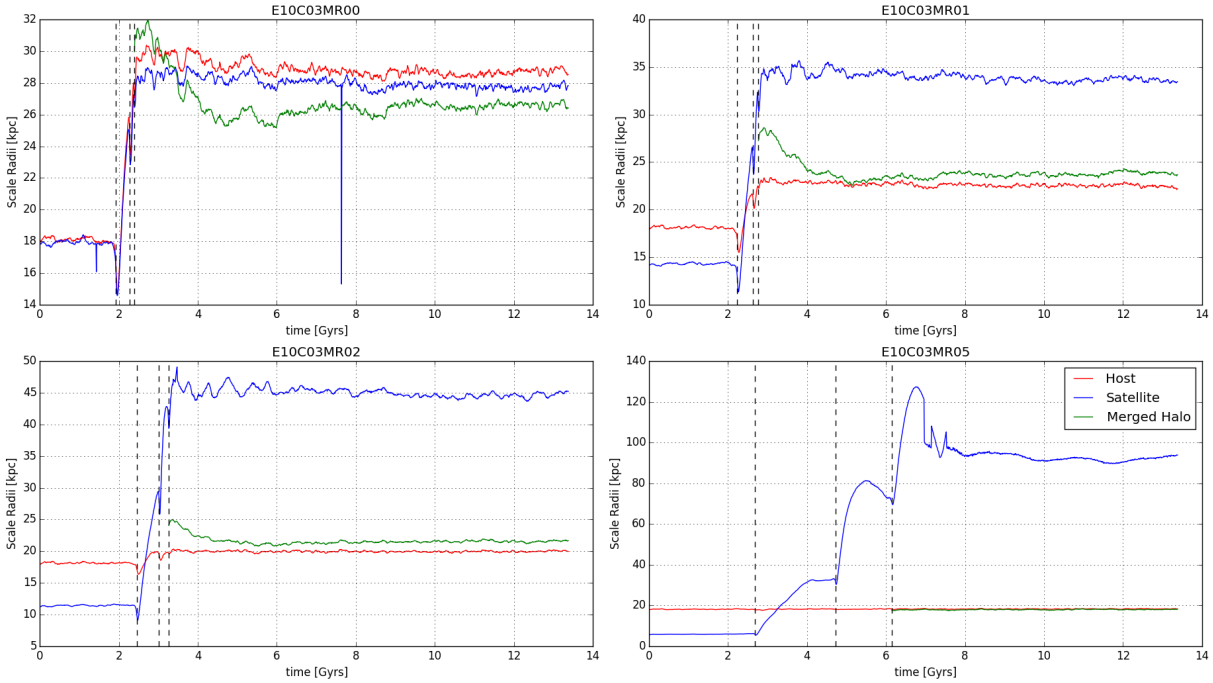

Figure 4.5: The change in scale radius throughout the merger for all simulation with circularity $\eta = 0.3$.The final scale radius of the halo is defined as its scale radius after the third pericentric passage, at which point the system seems to have reached equilibrium. Top left panel shows the results for a mass ratio of 1:1; top right panel shows the results for a mass ratio of 1:2; bottom left panel shows the results for a mass ratio of 1:4; bottom right panel shows the results for a mass ratio of 1:32. The increase in scale radius after every merger can be observed to be mass dependent, being largest for 1:1 mergers and smallest for low mass ratio mergers.

law function of the mass ratio, although there is no formal reason for this to be the case. We may also note the possibility of an extremely weak circularity dependence, noting that all changes in scale radii are systematically larger for $\eta = 0.7$, although not significantly. Since this relationship is non-trivial, we may try and relate it to other parameters and search for a physical reason for the shape of the function. We may also determine how the change in scale radius tracks the change in the final mass, however, this ends up simply being a translation of the function since,

$$\frac{M_{blue}}{M_{red}} = \frac{M_f}{M_{red}} - 1$$

We may then ask if the change in scale mass is related more simply to the change in

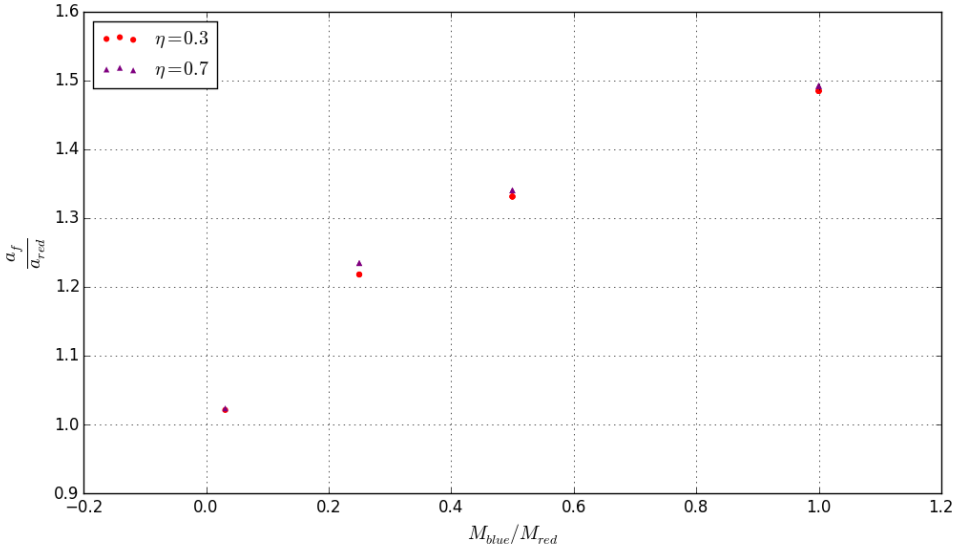

Figure 4.6: The relative increase in scale radius plotted as a function of the mass ratio. Circular points for $\eta = 0.3$ and triangular points for $\eta = 0.7$.

scale radius. This however should not change the relationship, as for Hernquist profiles, the ratio of initial and final scale masses will simply reduce to the ratio of the final mass to the initial mass.

We may think however that the mass which causes the heating of the core, ends up staying in the core, if the interactions are local. In such a way, the outer layer of the halo may be stripped while sinking into the halo, allowing for the majority of the inner blue particles to exchange energy with the inner red particles. In this way, we could make a naive postulate; the blue particle mass which is within a scale radius "a_{red}" centered on the blue halo is that which will generate the heating of the red core. This serves essentially as an approximation of the satellite mass. The mass dictates the amount of heating which occurs since the dynamical friction force, serving as the only mechanism by which the orbital energy is transfered into the red halo, depends quadratically on this mass. Let us relate then, the ratio of this *local mass* from the blue halo and the mass within the red halos own scale radius, to the relative increase in scale radius as in figure 4.7, noting that $M_{red}(r < a_{red}) = M_{red}/4$.

We will call this ratio of masses, the local mass ratio (LMR). We find a roughly linear relationship between the LMR and the relative increase in scale radius. Thankfully the *local mass* of the blue halo, as described above, is analytically tractable in terms of the

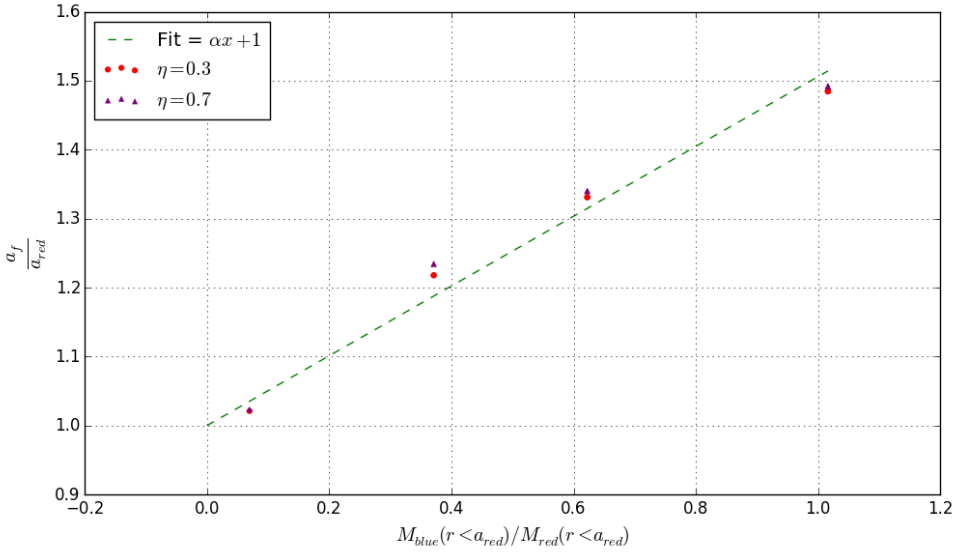

Figure 4.7: The change in scale radius plotted as a function of the local mass ratio (LMR) $M_{blue}(r < a_{red})/M_{red}(r < a_{red})$. Linear fit $a_f/a_{red} = \alpha(LMR) + 1$, where $\alpha = 0.4977 \pm 0.01828$.

mass ratio and scale radii (or concentration). Given that,

$$M(r) = M_o \frac{r^2}{(r+a)^2}$$

then,

$$\frac{M_{blue}(r < a_{red})}{M_{red}(r < a_{red})} = \frac{4M_{blue}(r < a_{red})}{M_{o,red}} = \frac{4M_{o,blue}}{M_{o,red}} \frac{a_{red}^2}{(a_{red} + a_{blue})^2}$$

$$\frac{M_{blue}(r < a_{red})}{M_{red}(r < a_{red})} = \frac{4M_{o,blue}}{M_{o,red}} \left[\frac{a_{red}^2}{a_{red}^2(1 + \frac{a_{blue}}{a_{red}})^2} \right]$$

$$\frac{M_{blue}(r < a_{red})}{M_{red}(r < a_{red})} = 4 \left(1 + \frac{a_{blue}}{a_{red}} \right)^{-2} \frac{M_{o,blue}}{M_{o,red}} \tag{4.1}$$

Carrying this through to the function relating the change in scale radius to the LMR, we obtain a fairly simple relation,

$$\frac{a_{final}}{a_{o,red}} = \alpha \left[4 \left(1 + \frac{a_{blue}}{a_{red}} \right)^{-2} \frac{M_{o,blue}}{M_{o,red}} \right] + 1 \approx \left[2 \left(1 + \frac{a_{blue}}{a_{red}} \right)^{-2} \frac{M_{o,blue}}{M_{o,red}} \right] + 1 \tag{4.2}$$

Although the assumptions are simple we may obtain a relatively accurate estimation of the scale radius increase. Looking at figure 4.8 We see the model underestimates the change in scale radius more significantly for moderate mass ratios. One should also note however, that the model does not include any circularity dependence while it is expected to be there in some form.

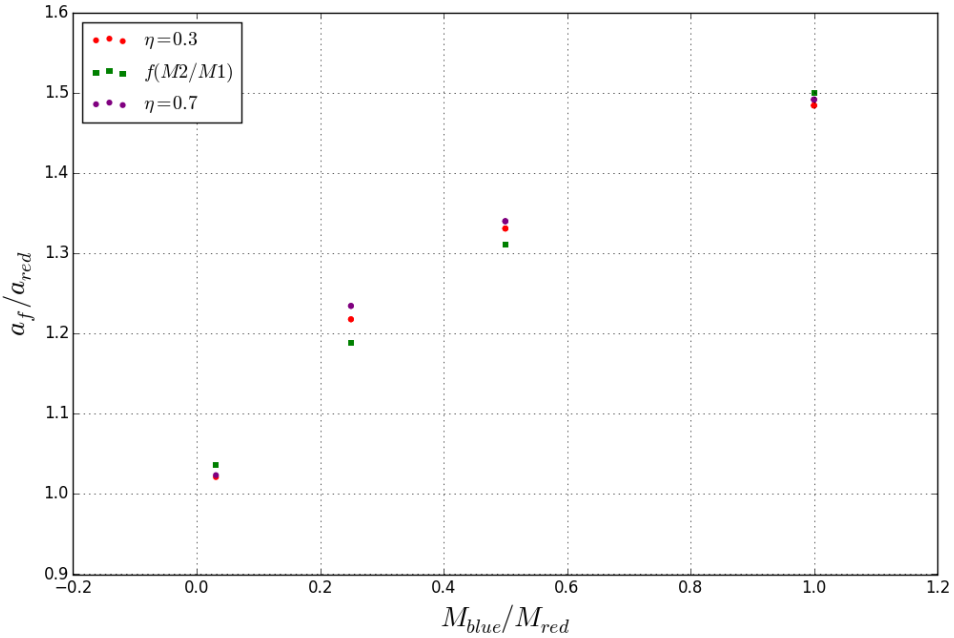

Figure 4.8: The change in scale radius plotted as a function of the mass ratio model as in equation 4.2 using fitting parameter $\alpha = 0.4977 \pm 0.01828$.

4.5 Summary

As shown in this chapter, mergers heat a halo unevenly. Large amounts of energy appear to be dumped into the exterior of the halo causing large increases in average radii, while the average radius of inner shells only increase slightly. Of course, there is considerable energy being deposited into these inner shells; the depth of the potential, however, is also increasing correspondingly. Despite this, the core of the halo does have a tendency to be heated. This heating overall tends to make the halo "puffy" , i.e. increases the overall extent of the halo, and making the density profile of the red halo more shallow, suggesting that a drop in concentration should occur. This is reflected equally well in

the cumulative mass distribution and the density profile, demonstrating in both cases the overall transport of material from the core to larger radii. Changes in the fitted scale radius provide a measure of this heating. The increase in the scale radius, representing fundamentally the extent of mass considered to be the core of the halo, is observed to have non-trivial dependence on the mass of the in-falling halo. Using naive and very simple assumptions, however, we have developed a simple model which provides the ability to estimate the change in the scale radius as function of the mass ratio of the merging objects. This model is limited in terms of ignoring the orbit of the interaction and could be revised using a large sample of circularities, although the dependence on this parameter seems limited. This model could be revised however, looking at the possible orbital energy parameter dependence as all simulations here were performed at the same orbital energy with $\epsilon = 1$. From our data, this model also appears to under estimate the change in scale radius for moderate mass ratios.

Chapter 5

Mixing

5.1 Introduction

The mixing of the material within the final halo is also of great interest. It is suggested that particles in a halo, at the individual level retain little to no memory of initial conditions and are well mixed among themselves during merger, while on a mesoscopic scale groups of particles remain quite ordered[18, 5]. The process by which the individual particles in a given system lose their memories of initial conditions is named *relaxation*. Through two-body encounters, objects wander away from their initial velocities, energies and orbits. This, in fact, is what generates the inhomogeneous nature of stellar systems. One should not only expect self-mixing of an individual halo but also expect a certain amount of phase-space mixing among merging structures, as they will overlap spatially. Both these issues were addressed in this study in order to better identify whether the distinction between "old" and "new" material is relevant in phase-space, as well as whether memory of initial conditions is retained in halos after singular mergers. The effects were tested over several host-satellite mass ratios in order to examine its dependence on the satellite mass; one could postulate, for example, that due to its mass and consequently the energy exchange, a $1:1$ mass ratio merger would lead to more mixing. Although the mass may play an important part in determining the level of mixing, it is also relevant to examine the circularity with which the merger occurs. A purely radial orbit would be thought to generate a higher degree of self-mixing within a host halo by trailing material through the center across the halo. Conversely, one would expect an almost circular orbit to generate little mixing, smoothly sinking into the host halo's potential well which would produce very little radial disturbance.

5.2 Self-mixing

Looking at an entire system, one can measure the level at which the current properties of the particles match their original configuration. At an individual particle level we can observe an example of the loss of coherence between the original radial configuration and the radial configuration at later times, as shown in figure 5.1. The radial spread increases as a function of time as the system becomes more and more mixed. The radial spread demonstrates the increased variation in radial position for any given particle. Even though the scatter increases, the structure of the relation retains its shape and indicate some level of correlation. In this study, the mixing in both energy and radii was measured using two statistics. The first statistic used was a simple rank correlation rating, in order to verify how monotonically related the original distribution of either property was to the same distribution in its later dynamical states. The Spearman rank correlation function is formulated as,

$$\rho_x = 1 - \frac{6\Sigma d_i^2}{n(n^2-1)} \tag{5.1}$$

where the variables from each dataset X_i ,Y_i are converted into into ranks x_i,y_i, such that, $d_i = x_i - y_i$. The parameter n is the number of objects in either dataset. This statistic provides a good tool for verifying the coherence between a property at different times since it is non-parametric. This statistic will be most sensitive to radial and energetic shell crossings, since it measures only whether or not the two sets are related monotonically. Any deviations in the form of particles exchanging rank will lower the statistic from its maximum correlation of $\rho = 1$ to either a random arrangement corresponding to $\rho = 0$, or a maximum anti-correlation of $\rho = -1$.

Work produced by both Kandrup et al. (1993) and Voglis et al. (1995) using simulated mergers demonstrate a definite correlation between binned energy distributions before and after mergers [18, 43]. Kandrup et al.(1993) demonstrated a final correlation between the initial and final individual energies, calculated with respect to the halo center of mass and to the global center of mass to be ~ 0.64 and ~ 0.48, respectively. These rank correlations were found to be accompanied by large rms deviations in the ranking, suggesting that on a microscopic level the individual particle energy ordering was generally *not* conserved. An important element was that these rank correlations were calculated using *both* red and blue halos (using our nomenclature). In this study, we will focus on the red halo and, therefore the local center-of-mass energies will be computed. The correlation coefficients will be based on the radii and energies of the red halo only. The rank order of binned energies were also examined, showing almost no change in rank amongst bins. The effects outlined in Kandrup et al. were studied (and expanded upon) by Dantas & Ramos (2006)[9] in

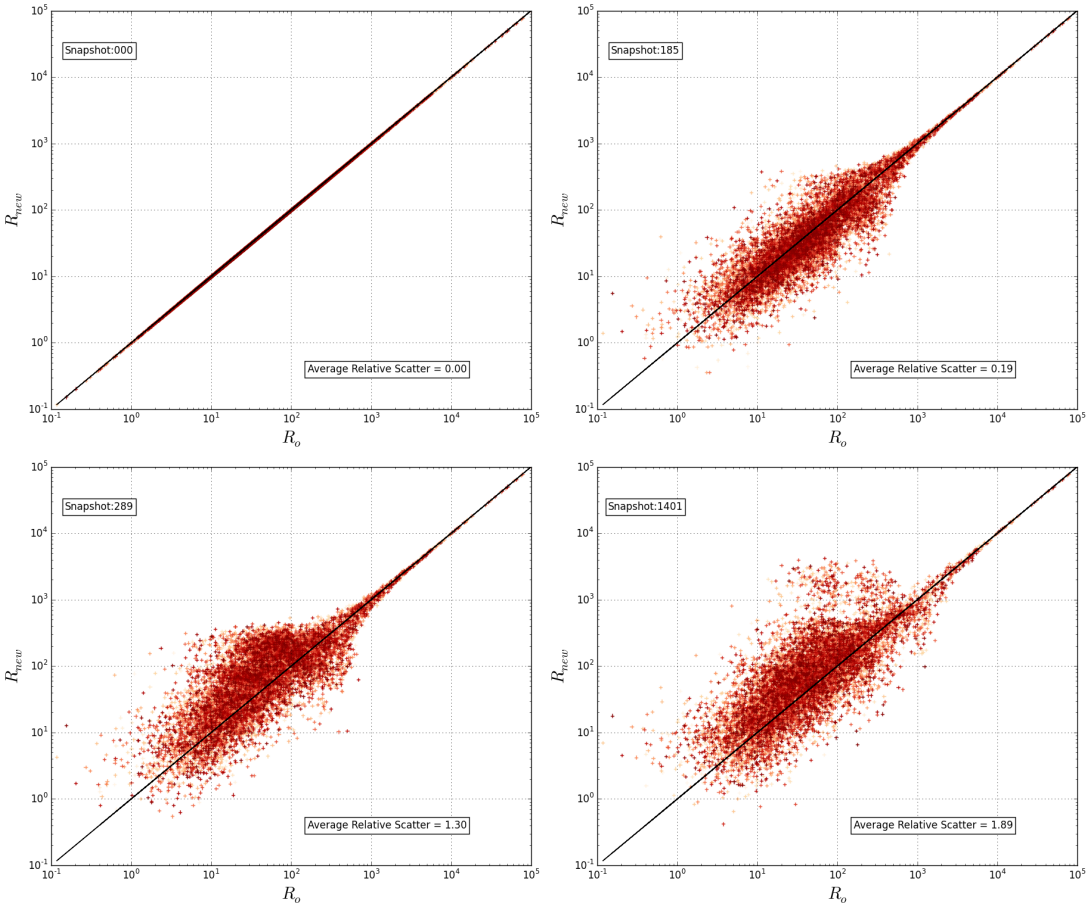

Figure 5.1: Radial scatter of particles for simulation *E10C07MR00* at the inital conditions (top left), first pericentric passage (top right), third pericentric passage (bottom left) and final snapshot (bottom right). The current radial positions of each particle versus their initial radial positions is plotted in red, and the one-to-one line of perfect correlation is plotted in black. The annotation denote the average relative radial scatter.

a cosmological context, developing constraints on the coarse-graining level necessary to effectively measure shell rank ordering. These issues should not be present in the context of these simulations, being significantly higher-resolution simulations, while only using 50 bins (six times the number of particles, and 2.5 times the number of bins found in Kandrup et al. (1993)). In a similar fashion to Kandrup et al., both the binned energies and individual energies were correlated through time and their respective rank correlations computed, as shown in figures 5.2 and 5.3. In a direct measurement of the rank correlation statistic for both radius and energy of individual particles, two stages of disordering were clearly seen in figure 5.2. The first disordering is naturally occurring, in that the individual

particles typically travel on eccentric orbits and therefore have different radii at different times, losing their individual particle ordering within an orbit. This fact is captured by the level of correlation, as it is maintained at approximately $\rho \approx 0.875$ until merger. The second disordering occurs at about the first pericentric passage where, depending on the amount of mass involved in the merger, we may observe larger or weaker levels of disordering. Evidently, major mergers result in more significant disturbances in the order, when compared to minor mergers. The largest overall disorder seen, however, occurring with the largest host-satellite mass ratio drops the correlation only to about $\rho \approx 0.725$, an unexpectedly high level of order if we were to refer to the binned correlation findings of Kandrup et al.(1993)[18]. From figure 5.2 we can see that, surprisingly, the rank ordering

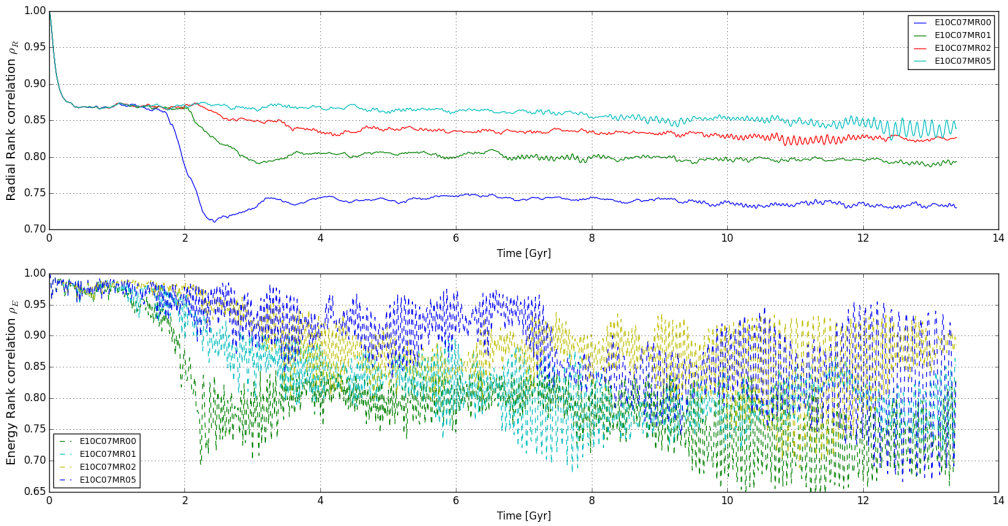

Figure 5.2: Rank correlation for radii and energy of individual particles for all simulations with circularity $\eta = 0.7$ corresponding to mass ratios 1:1 (blue), 1:2 (green), 1:4 (red), 1:32 (cyan).

of particles is relatively well conserved, despite some of the host halos undergoing large amounts of heating.

The analysis above clearly indicates the correlation between the mass of the satellite with respect to the host and the disordering of the halo, to a maximum disordering demonstrated by the $1:1$ merger. This analysis, however, does not take into account any possible effects caused by the concentration of the blue halo, as each halo is matched in concentration. As discussed previously, the levels of rank correlation observed when using binned energy information are expected to be very high, with the binned energies being highly

monotonic. This idea proved to be entirely consistent with the data collected from this set of simulation. In all cases, one would expect the highest mass ratio encounter to provide the largest amount of mixing. Despite generating large gravitational disturbances, even such massive mergers have limited effect on the binned distributions as seen in figure 5.3. We see that the largest lasting effect occurs during the 1:1 merger, in which the maximal disturbance and therefore minimum correlation is seen to be at $\rho_R \sim 0.93$. These figures, along with figure 5.2, demonstrate that on a mesoscopic scale, the overall distribution and structure of the halo remains fairly coherent. Although individual particles may have a variety of energies and radial positions, they appear not to stray too significantly from their initial conditions. At the level of shells, the halo is extremely coherent and retains much information about its initial structure.

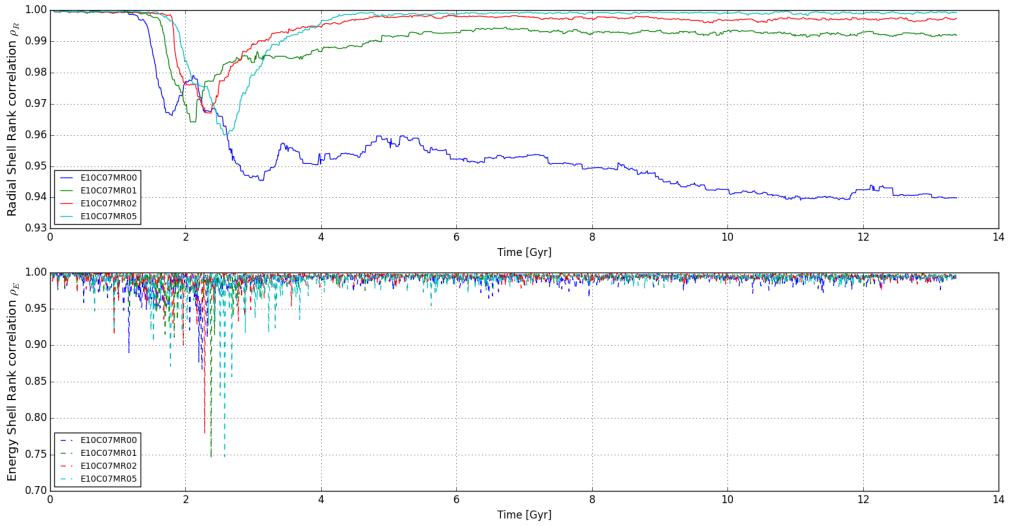

Figure 5.3: Rank correlation for binned radii (top) and energies (bottom) of particles for all simulations with circularity $\eta = 0.3$ corresponding to mass ratios 1:1 (blue), 1:2 (green), 1:4 (red), 1:32 (cyan).

5.3 Phase-Space Mixing

Other than self-mixing, the mixing between the merging structures is an astrophysically relevant phenomenon. With a clear understanding of phase-space mixing, it may be possible to differentiate new and old materials in merged systems. Phase-space mixing can be

defined as the overlap of between the spatial and velocity distributions of the red and blue halos. If the distribution of each observable is the same for both halos, they can be said to be perfectly mixed.

We consider three possibilities for the mixing of the blue halo with the red halo for either observable. Spatially, the first possibility is that the blue halo forms an outer shell around the red halo, such that the material is concentrated near its outer edge. The second is that the blue halo is captured and sinks to the center of the halo, such that most of the material may be seen to reside within the core of the red halo. The third possibility is that the blue halo ends up well mixed with its material permeating the red halo. Similarly, in velocity space, we expect the one-dimensional velocity distributions in well mixed halos to overlap entirely while the velocity distribution of unmixed halos will differ significantly. We will also use a χ^2 statistic in order to measure qualitatively how well the distributions are mixed in phase-space.

A naive way to qualitatively measure the phase-space mixing of halos is simply to visualize the final radial distribution and velocity distribution of each halo and verify if any obvious structural distinctions can be observed. We may visualize the spatial structure is through the radial distribution of the halo at the initial and final snapshot of the simulation. In figure 5.4 and 5.5 we see that for all except mass ratio 1:32, the final radial distributions of both halos tend to overlap. As the mass ratio becomes smaller, the two distributions do begin to be dissimilar. The 1:4 and 1:32 mergers also appear to form two distinct peaks of number density. These observations suggest a fairly high amount of mixing between the red and blue particles spatially for any mass ratio ner unity. It is clear however, that the 1:2,1:4, and 1:32 mergers demonstrate the gradual loss of spatial mixing between the halos. In the low mass ratio case, it appears that the blue halo is significantly heated and does not appear to track the red halo very well.

We may also observe the velocity distributions of the red and blue halos in a similar fashion to view how well they are affected by merger. Figure 5.6 pictures the velocity distributions of both halos post merger as well as the red particle distribution at initial conditions for simulations with $\eta = 0.3$; we can see that as the mass ratio decreases, the final halo velocity distributions appear to be more disparate. The same can be said of the final distributions in simulations with $\eta = 0.7$ when observing figure 5.7. We may notice an interesting difference from the $\eta = 0.3$ simulations however; the difference between the original red particle velocity distribution and its final state is decidedly more stark for simulations with $\eta = 0.7$. Thinking back to the small discrepancy in scale radius changes between both circularities in chapter 4, specifically in seen in figure 4.6, this may be an indication of heating being more efficient for more circular orbits. This is interesting but inconclusive, and may merit future investigation.

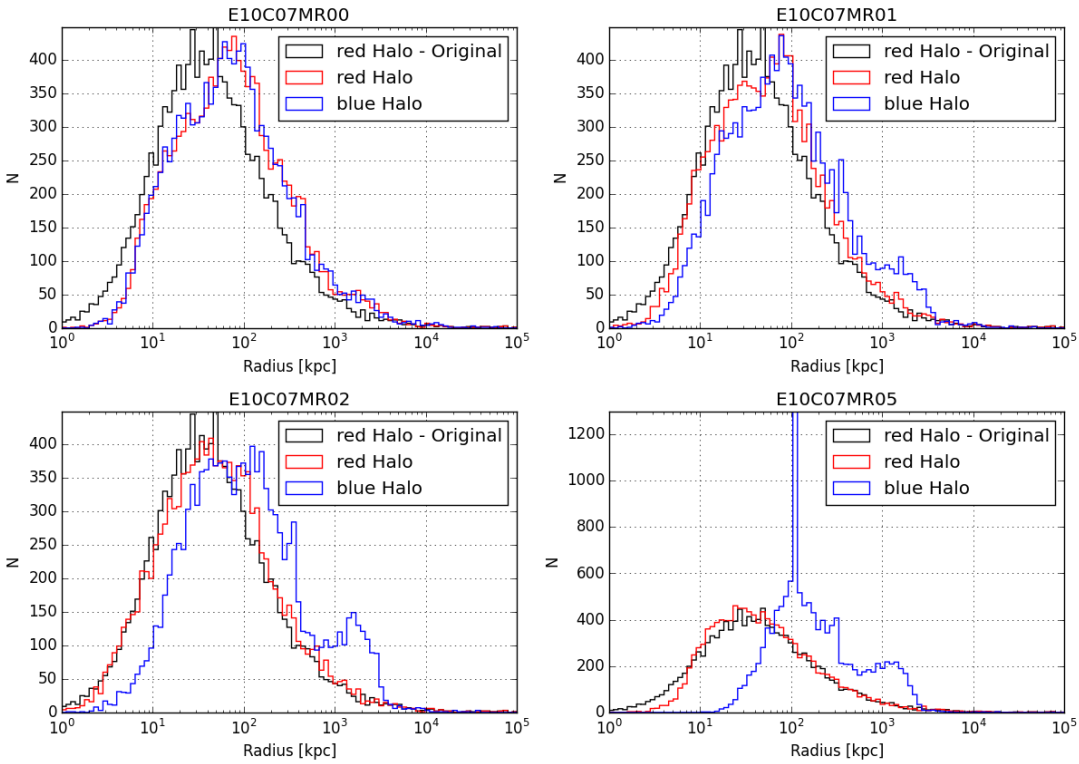

Figure 5.4: Radial distribution for red particles at initial conditions (black) and final snapshot (red) as well as blue particles at final snapshot (blue) for all simulations with circularity $\eta = 0.7$ corresponding to mass ratios 1:1 (top left), 1:2 (top right), 1:4 (bottom left), 1:32 (bottom right).

We wish to quantitatively describe the spherically averaged characteristics of phase-space of the halo. Let us reduce the dimensionality of the problem to two dimensions by using the magnitude of the distance and velocity such that our variables become $r = |\mathbf{x} - \mathbf{x}'|$ and $v = |\mathbf{v} - \mathrm{v}'|$ relative to the center of the red halo. In this way, the blue halo particles will, by default, start a distance away from the red halo in phase-space. Let us define a set of phase-space coordinates, $R = \{(r_1, v_1), (r_2, v_2), ..., (r_n, v_n)\}$ and $B = \{(r_1, v_1), (r_2, v_2), ..., (r_n, v_n)\}$ for the red and blue particles, respectively. Now we may form a pair of two-dimensional binned distributions $h_1(r, v)$ and $h_2(r, v)$, in order to measure an effective *distance* between them using a sort of χ^2 statistic of the form,

$$\chi^2 = \sum_i^N \sum_j^N \frac{(h_1(i,j) - h_2(i,j))^2}{\left(\frac{1}{h_1(i,j)} + \frac{1}{h_2(i,j)}\right)^{-1}} \tag{5.2}$$

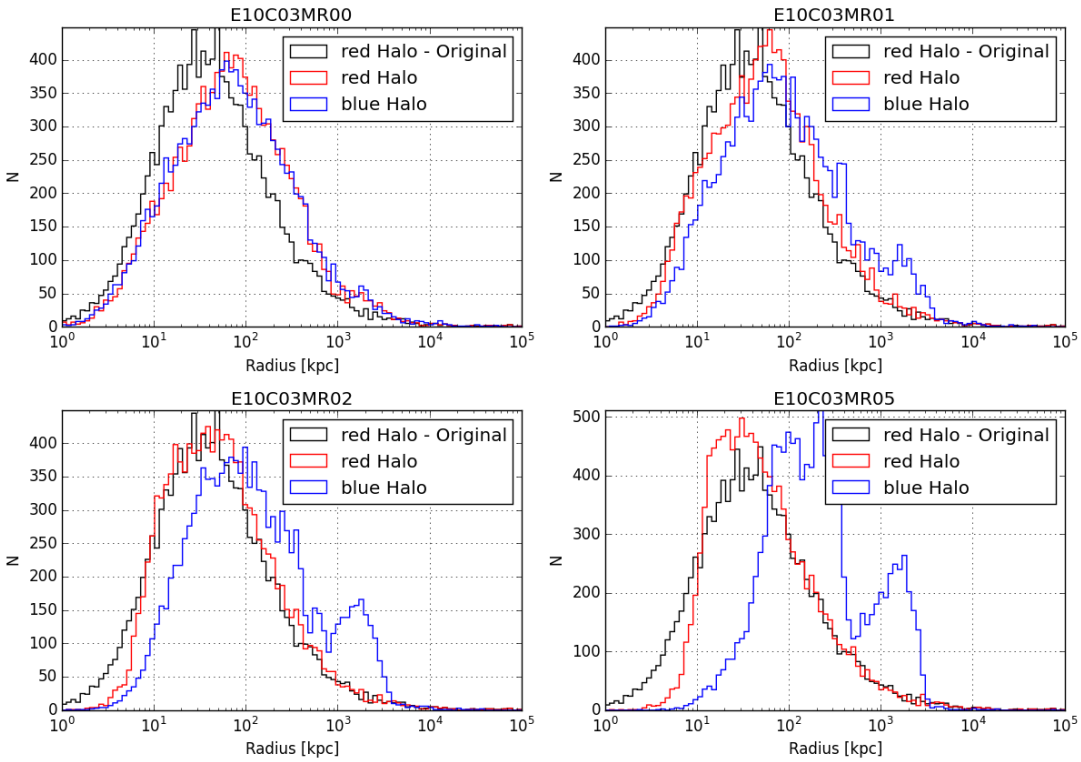

Figure 5.5: Radial distribution for red particles at initial conditions (black) and final snapshot (red) as well as blue particles at final snapshot (blue) for all simulations with circularity $\eta = 0.3$ corresponding to mass ratios 1:1 (top left), 1:2 (top right), 1:4 (bottom left), 1:32 (bottom right).

The behavior of the numerator in this statistic is self evident, while the behavior of the denominator dictates the weighting of the distance between bins. If both value in a particular bin are either very large or very small, Of course, this value on its own is useless as we have no reference value for two sets pulled from the same distribution. To understand the how mixed the two halos are, and as a result whether the histograms are pulled from the same distribution, two equal subsets of the phase-space coordinates for each halo were taken such that, generally, subsets A_i and A_j satisfy $A_i \bigcap A_j \equiv \emptyset; i \neq j$. Corresponding subsets (R_i,R_j and B_i,B_j) were binned by radius and velocity and compared using the distance measurement. Similarly, random subsets from each halo were compared against each other. This entire process was repeated 1000 times in order to build distributions of the χ^2 statistic for each comparison, that is: red to red, blue to blue and red to blue. The results of this comparison are shown in figure 5.8. The red-red and blue-blue distributions essentially define the approximate χ^2 for the distance between two subsets randomly pulled

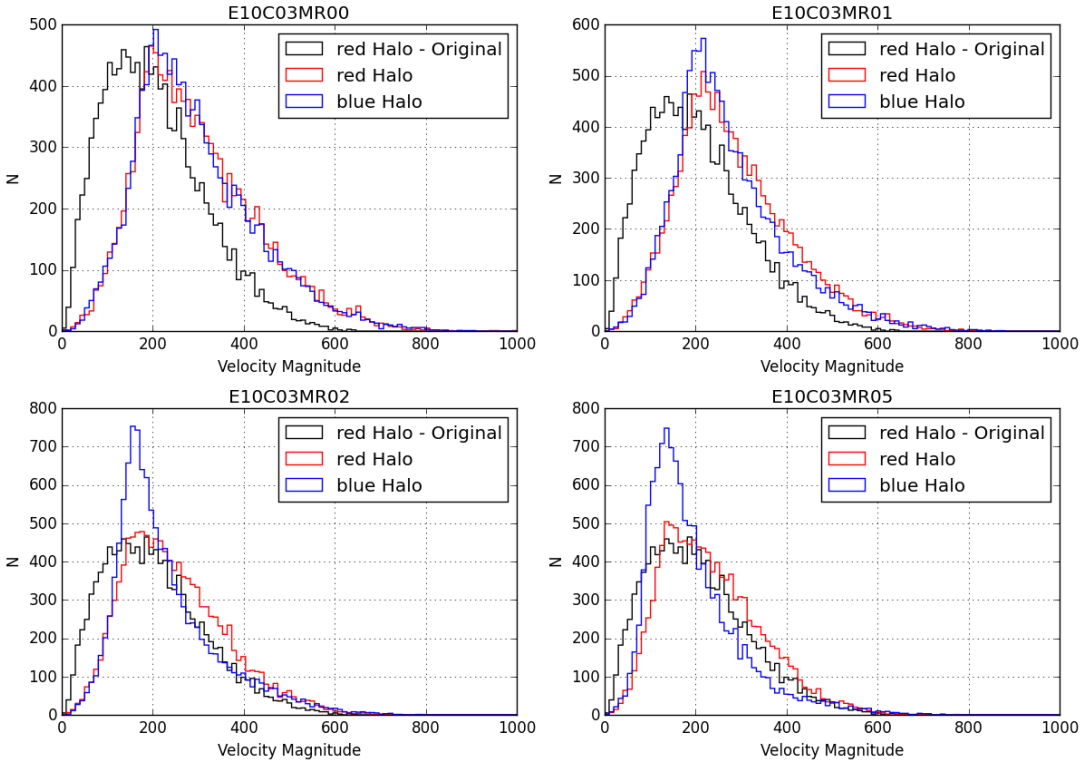

Figure 5.6: Velocity distribution for red particles at initial conditions (black) and final snapshot (red) as well as blue particles at final snapshot (blue) for all simulations with circularity $\eta = 0.3$ corresponding to mass ratios 1:1 (top left), 1:2 (top right), 1:4 (bottom left), 1:32 (bottom right).

from the same distribution. When the red-blue χ^2 distance distribution approaches that of the red-red and blue-blue distributions, it implies that the halos have become more and more mixed. We see that every pericentric passage causes the red-blue distribution to approach the other two, until finally, they overlap. Referring back to figure **??**, we see that as the mass ratio decreases the final distribution of blue particles tends to not track the corresponding red particle distribution; this effect is reflected using this measure of mixing. As may be seen in table 5.1 we can see that as the mass ratio decreases, the final distance between the $\overline{\chi^2}$ for the red-red and the red-blue distributions increases, suggesting that for low mass ratios phase-space mixing is inefficient.

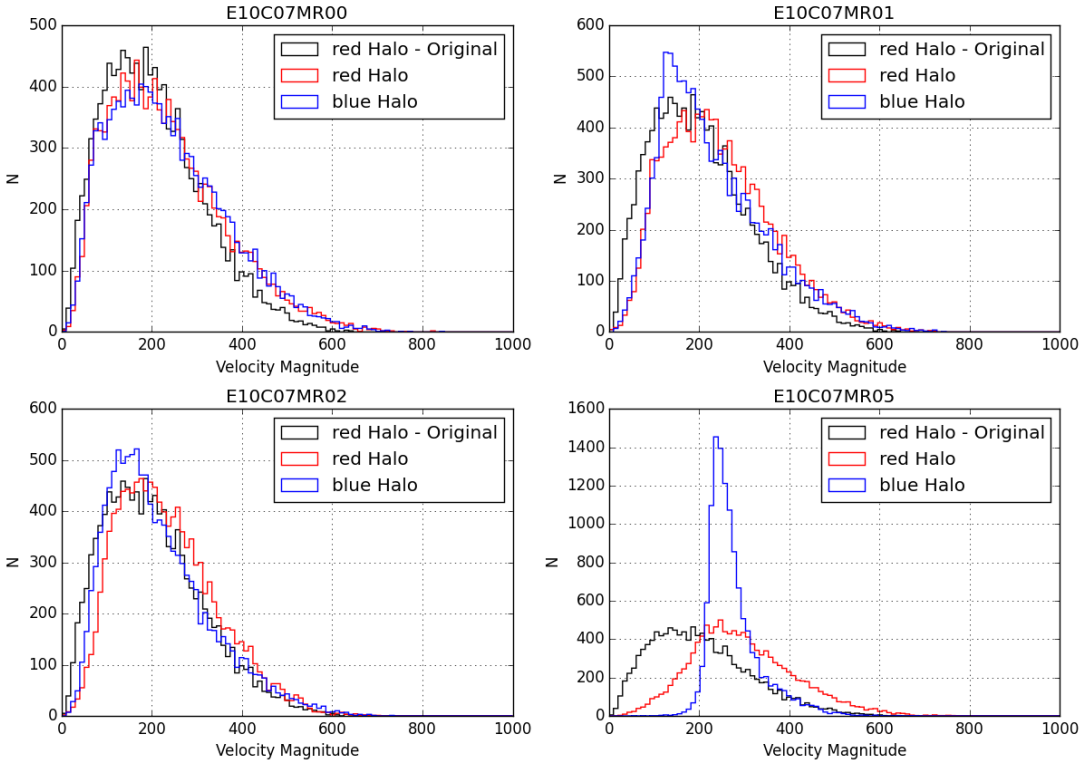

Figure 5.7: velocity distribution for red particles at initial conditions (black) and final snapshot (red) as well as blue particles at final snapshot (blue) for all simulations with circularity $\eta = 0.7$ corresponding to mass ratios 1:1 (top left), 1:2 (top right), 1:4 (bottom left), 1:32 (bottom right).

5.4 Summary

The rank correlation analysis, both for individual particles and for binned particles, demonstrates that self-mixing during mergers is highly dependent on the mass of the in-falling halo. Self-mixing also appears to be quite limited, with the particles only partially losing rank order and shells showing almost no violation of rank in both energy and radius. The findings at the level of multiple particles agree with the literature discussed earlier exceptionally well, while at the individual particle level, mixing is slightly less efficient then expected from the literature, with energy losing rank ordering on the same level and over the same timescale as the rank ordering of radii.

Phase-space mixing between merging halos is also found to be significantly mass dependent, with the distance between the self-sampled χ^2 distributions and the cross sampled

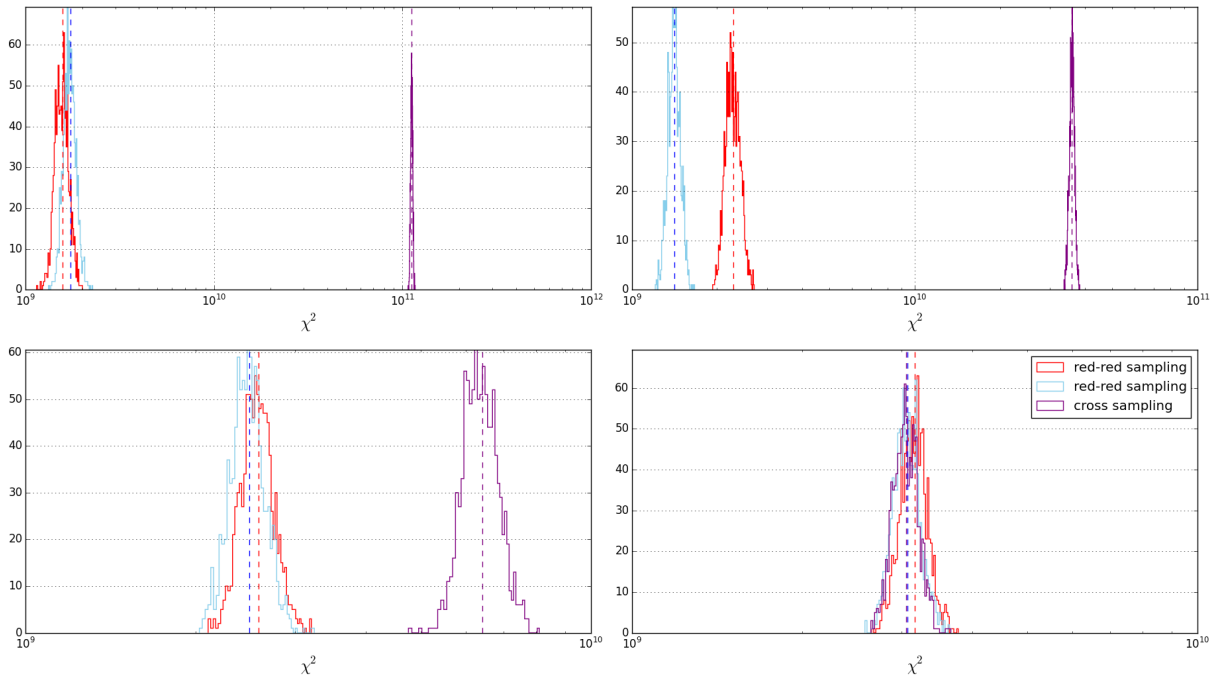

Figure 5.8: χ^2 distributions for red-red, blue-blue and red-blue random sampling comparisons for mass ratio 1:1 and circularity $\eta = 0.3$ at initial conditions (top left), first pericentric passage (top right), third pericentric passage (bottom left), and final timestep (bottom right).

distribution being anti-correlated to the mass ratio. This implies that there is in fact a statistical difference in the final structure of the blue and red particle distributions. It may be possible, for astrophysical applications, to distinguish these particles based on their radial and velocity characteristics.

Mass Ratio	η	$\overline{\chi^2}_{rr}\,[10^9]$	$\overline{\chi^2}_{bb}\,[10^9]$	$\Delta\overline{\chi^2}/\overline{\chi^2}_{rr}$	$\Delta\overline{\chi^2}/\overline{\chi^2}_{bb}$
1:1	0.7	2.40	2.44	0.006	0.011
	0.3	3.17	3.09	0.035	0.0099
1:2	0.7	2.42	2.56	0.156	0.092
	0.3	2.50	2.88	0.233	0.073
1:4	0.7	2.16	2.57	0.983	0.669
	0.3	2.27	2.42	0.424	0.334
1:32	0.7	2.34	1.22	14.1	27.9
	0.3	2.09	2.31	8.99	8.07

Table 5.1: χ^2 distribution data for red-red (rr), blue-blue (bb) and red-blue (rb) distributions: outlining red-red centroid, blue-blue centroid, relative distance between red-red centroid and red-blue centroid as well as the relative distance between blue-blue centroid and red-blue centroid.

Chapter 6

Cosmological simulations

6.1 Introduction

Thus far, we've dealt purely with single merger events. In reality, halos undergo multiple major mergers, accreting a significant fraction of their mass by this mechanism[11]. It is logical that if single merger events rearrange the halo density profile and change the concentration, a series of multiple mergers would also affect the concentration. As discussed previously, the specific sequence of mergers and accretion for any particular halo may be defined as a mass accretion history (MAH). In this section, we hope to study the age parameter and MAH fits proposed by Wong & Taylor (2012), as they pertain to the merger rate calculated from cosmological simulation. We also hope to study the statistics contained within these mass-accretion histories to develop and verify the merger rate calculation performed by Fakhouri & Ma (2008)[11] (hereafter FM).

6.2 Cosmological Simulation Setup

This set of cosmological simulations was created using the GRAFIC-2 and GADGET-2 codes[4, 37]. The initial conditions were created using GRAFIC2, a code producing a grid-based density and velocity distribution. GRAFIC-2 relies on the Zel'dovich approximation in order to produce a set of positions and velocities corresponding to particles perturbed from their original lattice positions.

The initial conditions were generated with WMAP7 cosmological parameters ($\Omega_b = 0.0449, \Omega_{CDM} = 0.222, \Omega_\Lambda = 0.734, h = 0.71$, and $\sigma_8 = 0.801$)[21], in a simulation box of

length 200Mpc h^{-1} containing $N = 256^3$ particles (called simulation *256 v1 L200* hereafter). Using these initial conditions in GADGET-2, the system was evolved to redshift z=0 using Newtonian gravity as described in chapter 2.

In order to construct merger trees it is necessary to first define how to identify halos and their associated particles within the simulation. Although many techniques to identify halos exist, there exist two techniques which are by far the most implemented: Friends-of-Friends (FoF) and Spherical Overdensity (SO) halo finding. These two methods solve the problem of defining halos within simulations in very different ways; FoF functions buy grouping nearby particles to each other while SO identifies halos using spherical regions around points of high density. SO generates halos within spherical volumes which tends to make them more spherical, while the shape of FoF halos are not constrained[45]. Halos do not have well defined physical boundaries in reality, thus, for the purposes of computing mass-accretion histories the most important characteristic is an accurate measurement of the mass irrespecive of shape. FoF provides a halo mass not constrained by the tendency of SO to form spherical halos. The FoF algorithm developed by the N-Body shop at University of Washington was used to define our halo objects.

6.2.1 Friends-of-Friends

The FoF halo finding algorithm is based on a key parameter "b" called the linking length. It works by recursively joining particles that are within a length $b\Delta_p$ apart from each other, where Δ_p is the mean inter-particle spacing. These joined particle sets are called friends. This algorithm leads to arbitrary halo shapes. From this particle list composing the halo, it is possible to compute many of its physical characteristics such as angular momentum, gravitational potential, velocity, shape, center of mass and orientation. This algorithm is susceptible to certain pitfalls however. The FoF algorithm may demonstrate an over-linking effect, the scenario in which two halos are linked by a bridge of particles. As a result what is obtained by the algorithm is not a single halo but a complex system of halos undergoing relaxation or merger. Its been found that generally 15-20% of all FoF determined halos calculated with linking length $b = 0.2$ are bridged objects. This effect may be corrected with a shorter linking length. Due to the expanding nature of the universe, and that the linking length is set to be a constant co-moving length, its physical length (within the simulation) will grow according to the expansion history of the universe or along with "z" the redshift. From these halos, we can follow a halo across multiple snapshots and create MAHs from a merger tree.

6.2.2 Merger Trees

Once the FoF halos are identified it is then possible to generate merger trees based on the halos from each snapshot and their associated particles. Beginning at redshift $z = 0$, we iteratively link the halos of the current snapshot to its progenitors in the previous snapshot. In order to determine whether or not a earlier halo is a progenitor of a more recent halo in an adjacent snapshot, we require that over half of the mass contained within the progenitor candidate finds itself within the descendant halo. This definition forces all progenitors to have a single descendant, and allows for multiple progenitors to compose the descendant. In order to determine the main progenitor of the descendant halo, we simply define the main progenitor as the parent halo which constitutes the largest mass fraction in the child halo. Using this method, we may go through all the snapshots creating a single sequence of halos leading down to the $z = 0$ snapshot. This sequence of halos provides a well-defined MAH for the final halo. For the following study, all halos with over 1000 particles at $z = 0$ were selected[48].

6.3 Mass Accretion Histories

As discussed in chapter 1, McBride et al. (2009) combined developed a two parameter fitting function of the form,

$$\frac{M(z)}{M_o} = (1+z)^{\beta} e^{-\gamma z} \tag{6.1}$$

where β and γ are fitting parameters, $\gamma = \ln(2)/z_f$, and z_f is the formation time defined as $M(z_f) = M(0)/2$. Although this form provides adequate results, the fitting values are strongly correlated implying the possibility that a better one-dimensional parameterization may be possible. Wong and Taylor (2012)[48] (WT12 hereafter) carried out a principal component analysis on a large set of MAHs in order to determine the functional form of this fit. It was determined from the principal component's strong dependence on the concentration parameter, as well as $z_{0.5} = M(0)/2$, that the principal component is a reflection of the age of the halo. The measure of age of the halo may be computed through fitting the analytic form developed in terms of the derivative of $M(z)/M_o$. This fit takes the form,

$$\frac{d}{da}\frac{M(a)}{M_o} = f(a) = \exp\left[-Sa\right] \exp\left[-\frac{1}{g(S)a}\right] \tag{6.2}$$

where S is the fitted age parameter and g(S) may be defined as,

$$g(S) = 5 \exp\left[-\frac{S}{4.5}\right] \exp\left[-\frac{1}{5S}\right] \tag{6.3}$$

We fit our set of MAHs to this form in order to obtain a distribution of the age parameter, as shown in figure 6.1. We note that the age parameter distribution here is

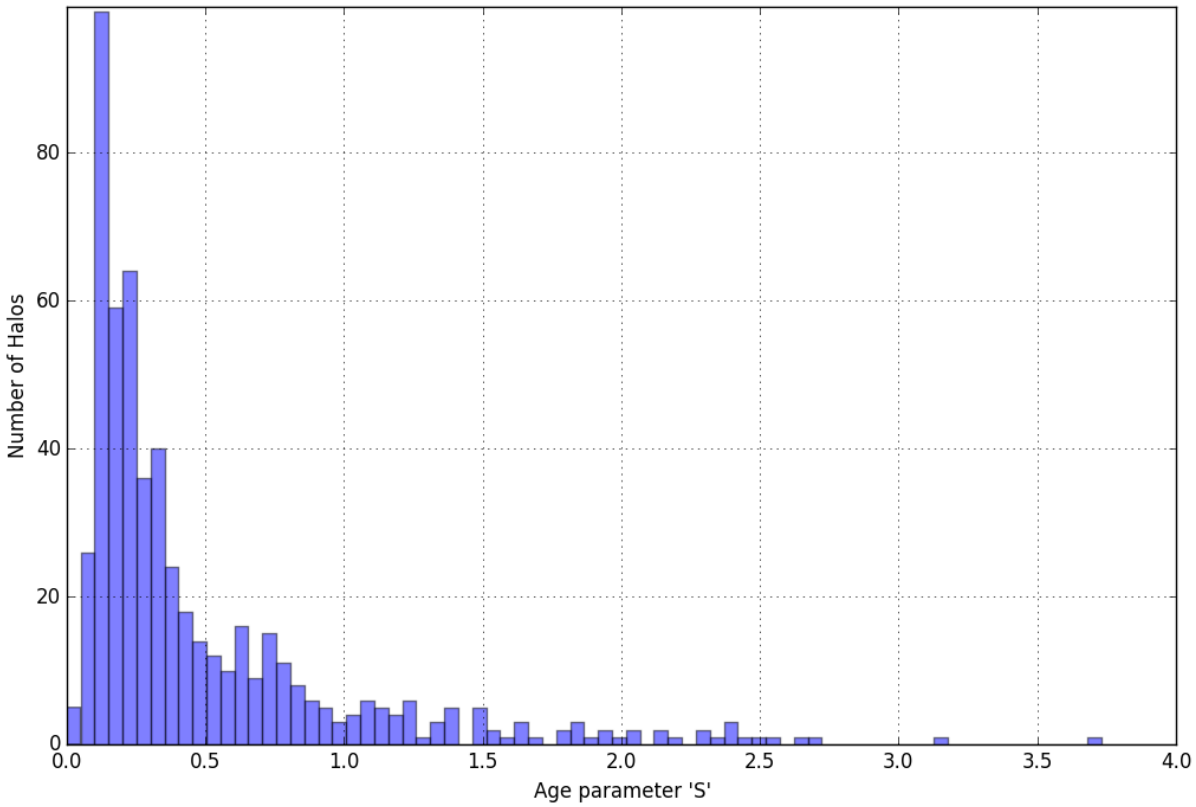

Figure 6.1: Age parameter S distribution for 556 well-resolved halos from simulation *256_v1_L200*.

skewed towards smaller age parameters. Now, using the relation between the deviation from the average MAH and the age parameter from the data in WT12, we may measure the distribution of deviations from the mean MAH. This distribution appears skewed in the favor of late forming halos as its un-binned average deviation from the mean MAH lies at $\bar{\sigma} = -1.565$. The sample of halos taken is relatively small, having 68% of the number of halos used originally in WT12. This skew towards early type halos seems odd given that

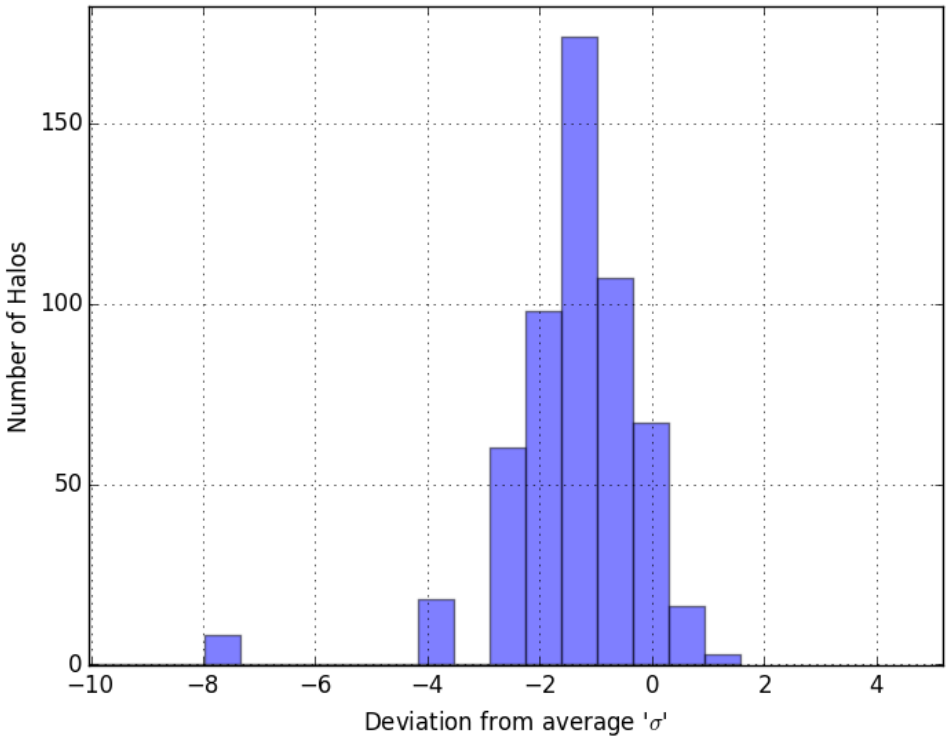

Figure 6.2: Distribution of deviations from the mean MAH calculated in WT12, for 556 well-resolved halos from simulation *256_v1_L200*

.

only massive halos with more then 1000 particles at $z = 0$ were selected, implying that a large number of low-mass halos, which are presumably younger on average, are being cut from the sample.

The mass-accretion histories serve an additional purpose. They allow for the use of our model in order to predict a concentration distribution at redshift $z = 0$. Two models were used in order to visualize the theoretical concentrations of the halos, what will be called a *reset* model and our heating model outlined previously. The reset model simply assumes that any major merger will reset the concentration to 4 and thus change the scale radius. Otherwise there is no change in scale radius. The heating model is outlined as above. Both models assume that the initial concentration of the halo at early times is $c = 4$. Figure 6.4 demonstrates a sample mass accretion history along with the scale radius as a function of time for both models. All 556 MAHs extracted from the simulation were used in order to build an understanding of the concentrations of these halos at $z = 0$ would

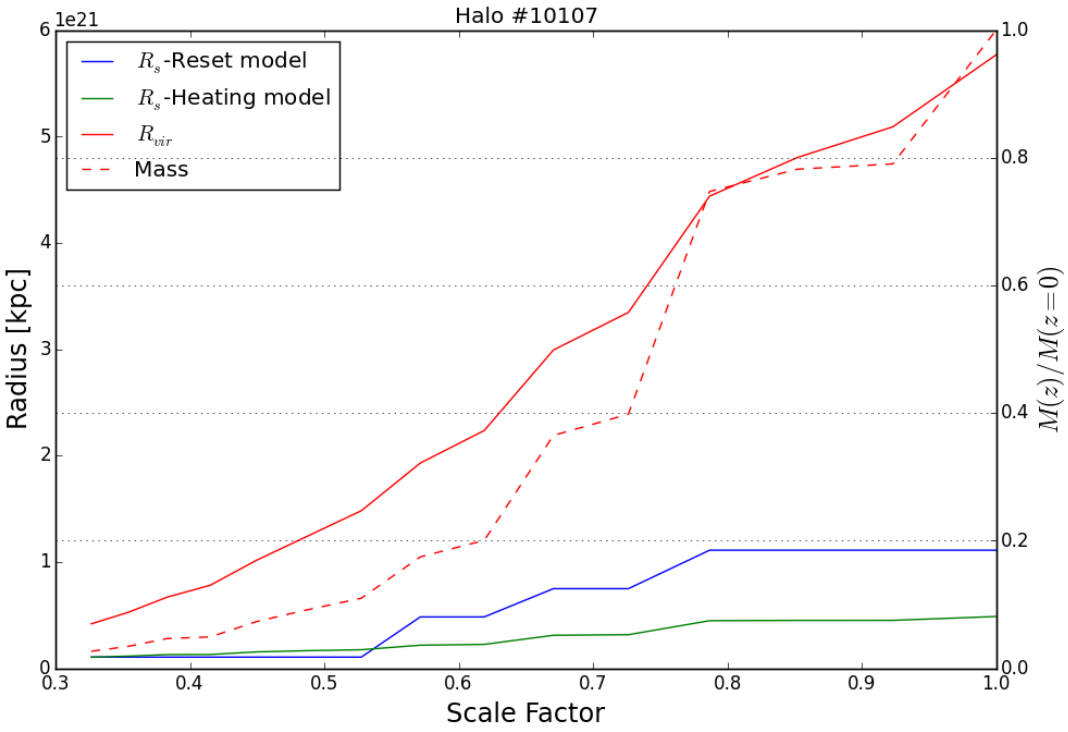

Figure 6.3: MAH (red dashed), virial radius (red solid), and scale radius determined using reset model (blue) and heating model (green).

can theoretically look like. The concentration distribution can be seen in figure **??**. We note that on average halos tend to get much more less heated uisng the heating model, however, the temporal resolution of the simulation is poor which leads to only using single merger events with relatively high mass ratio.

6.4 Merger Rates

Consider a merger where an object of mass M1 merges with one or more other halos, producing an object of final mass M_o. The progenitor mass ratio ξ, is defined as:

$$\xi \equiv \frac{M_i}{M_1} \tag{6.4}$$

Where M_1 is the most massive progenitor and i ranges from 2 to the number of progenitors N_P. Using the cosmological simulations we produced we may estimate the mean merger

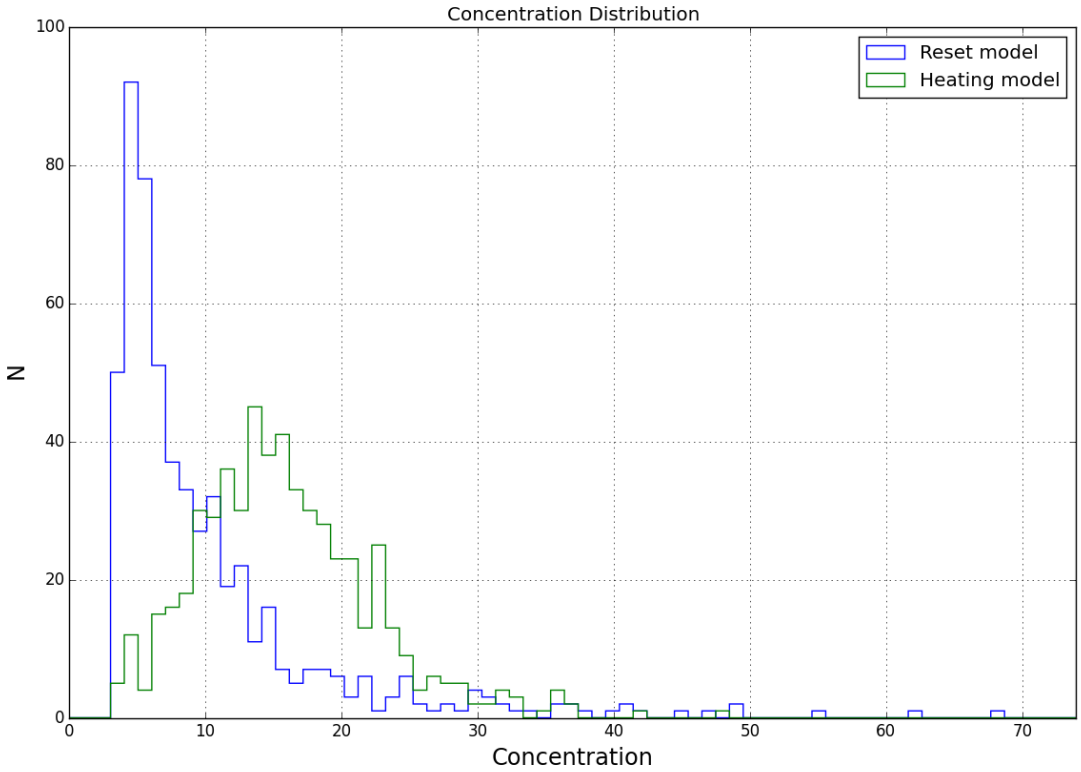

Figure 6.4: Concentration distribution at redshift $z = 0$ determined using the reset model (blue) and the heating model (green)

.

rate for these halos as:

$$\frac{B}{n} \equiv \frac{B(M_o, \xi, z_P : z_D)}{n(M_o, z_D)} \tag{6.5}$$

Here, $B(M_o, \xi, z_P : z_D)$ measures the mean merger rate (mergers per unit redshift) per unit volume for a descendant halo at redhift z_D with mass M_o, with progenitor mass fraction ξ, for progenitors at redshift z_P. $n(M_o, z_D)$ measures the number density of the descendant halos at redshift z_D. Thus, B/n describes the number of mergers per halo for descendant halos of mass M_o and progenitor mass ratio ξ, as in FM. We will use a binary model of merger and assume that the total mass in secondary progenitors is contained within a single halo before merging with the main progenitor such that $M_{secondary} = \sum_2^{N_P} M_i$.

Fakhouri & Ma (2008) (FM hereafter) propose a universal fitting form for B/n described

by,

$$\frac{B(M_o, \xi, z_P : z_D)}{n(M_o, z_D)} = A \left(\frac{M_o}{\tilde{M}}\right)^{\alpha} \xi^{\beta} \exp\left[\left(\frac{\xi}{\bar{\xi}}\right)^{\gamma}\right] \left(\frac{d\delta_c}{dz}\right)^{\eta} \tag{6.6}$$

where $\tilde{M} = 1.2 \times 10^{12} M_{\odot}$ and $\delta_c(z) \propto 1/D(z)$ is the density collapse threshold normalized to $\delta_c = 1.686$ at $z = 0$, with $D(z)$ being the linear growth factor. Typical values for these constants are $A = 0.0344, \bar{\xi} = 0.125, \alpha = 0.118, \beta = -1.921, \gamma = 0.399, and \eta = 0.853$ as given in Fakhouri & Ma (2008).

Integrating the differential merger rate over M_o and over ξ, we may also calculate the mean merger rate for all descendant halos with mass within a given mass range $[m, M]$, and progenitor mass within range $[x, X]$, given by,

$$\frac{d\bar{N}_{merge}}{dz}([m, M], [x, X], z_P : z_D) = \frac{1}{N} \int_m^M \int_x^X B(M_o, \xi, z_P : z_D) d\xi dM_o \tag{6.7}$$

where N is the total number of halos with mass within the range $M \in [m, M]$.

Due to the assumption of mergers being binary rather than involving multiple halos, we expect to underestimate the merger rate for both low ξ and large Δz. In the case of low ξ, the smaller secondary progenitor halos will be aggregated to the largest secondary progenitor, causing their contribution to the merger rate to be neglected. In the case of large Δz, the binary assumption is simply not valid, and adds a secondary decrease to the low-ξ merger rate. This is discussed thoroughly in FM[11].

6.5 Calculating The Merger Rate

The merger rates discussed above were calculated for simulation *256_v1_L200*. Both the merger rate $B(M_o, \xi, z_P : z_D)$ and the merger rate per halo B/n were calculated using the set of mass-accretion histories discussed in the previous section. Figure 6.5 demonstrates what is outlined in FM, the mean merger rate per halo is nearly independent of the descendant mass. Although in the left panel of figure 6.5 there is an increase in the amplitude of $B(M_o, \xi, z_P : z_D)$ for larger M_o, dividing by the number of these objects re-normalizes the merger rates to be very nearly identical. Qualitatively this work matches the trends expected from FM when using the assumptions of binary merger. The negative contributions to the merger rates are a product of the binary merger assumption and the poor temporal resolution causing underestimation at values smaller than $\xi = 0.1$. An additional reduction of merger statistics caused by our selection criteria may also be observed, as any halos with particle number smaller than $N = 1000$ is also neglected from the computation

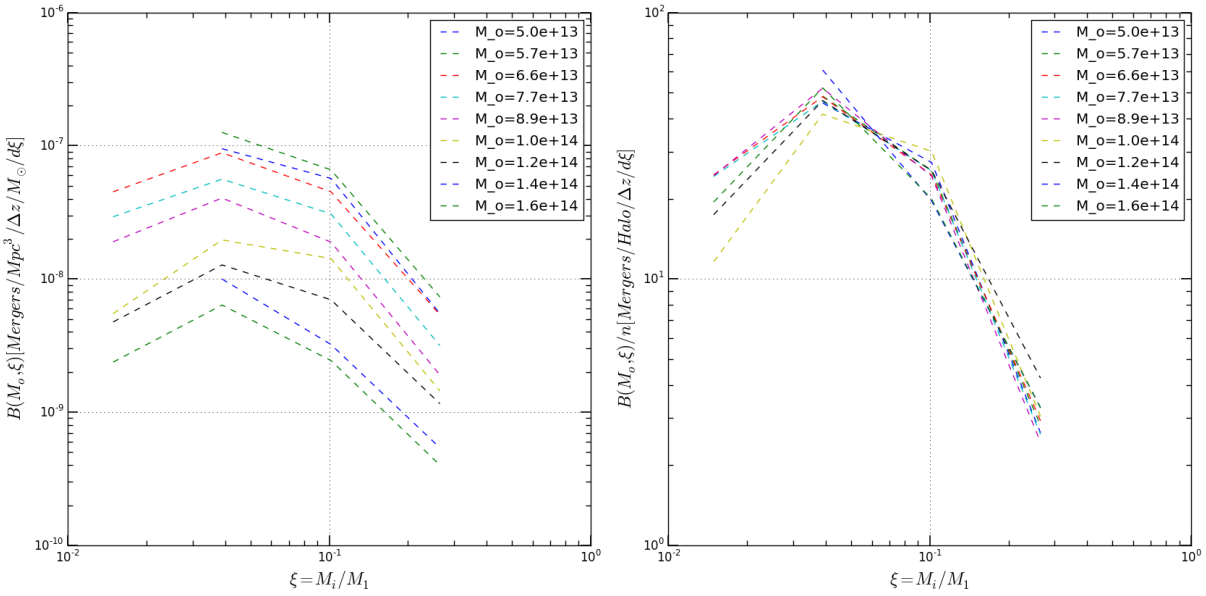

Figure 6.5: Left panel: Merger rate for descendant mass M_o with progenitor ratio ξ, as a function of ξ, at redshift bin z_i:z_f = 0:0.09. Right panel: Mean merger rate per halo for the same redshift bin, with mass dependence mostly collapsed.

of the merger rate, resulting in a reduction of the merger rate compared to FM. Overall we underestimate the merger rate even in regions where our resolution effects and the binary merger assumption are expected to be relatively negligible, this is possibly due to our halo finding algorithm or temporal resolution.

6.5.1 Major Mergers

It is of interest to understand how often major mergers occur as these have been shown to most strongly impact the host halo's structure (see chapter 4). Major mergers are the cause of large amounts of heating in the core and the consequent expansion of the scale radius. One-to-one mergers would be of interest, however given our definition of ξ, the progenitor mass ratio, and the limited temporal resolution of the simulation being used, we do not identify any truly equal-mass mergers. We can however, qualify the merger rate per halo for mergers with $\xi > 0.5$, which we will call *major* mergers. We can measure the major merger rate per halo at three mass scales as a function of redshift. These mass scale are that of galaxy-scale halos ($2 \times 10^{12} \leq M < 3 \times 10^{13}$), group-scale halos ($3 \times 10^{13} \leq M < 10^{14}$), and cluster-scale halos ($M \geq 10^{14}$). As seen in figure 6.6, generally we can see that the

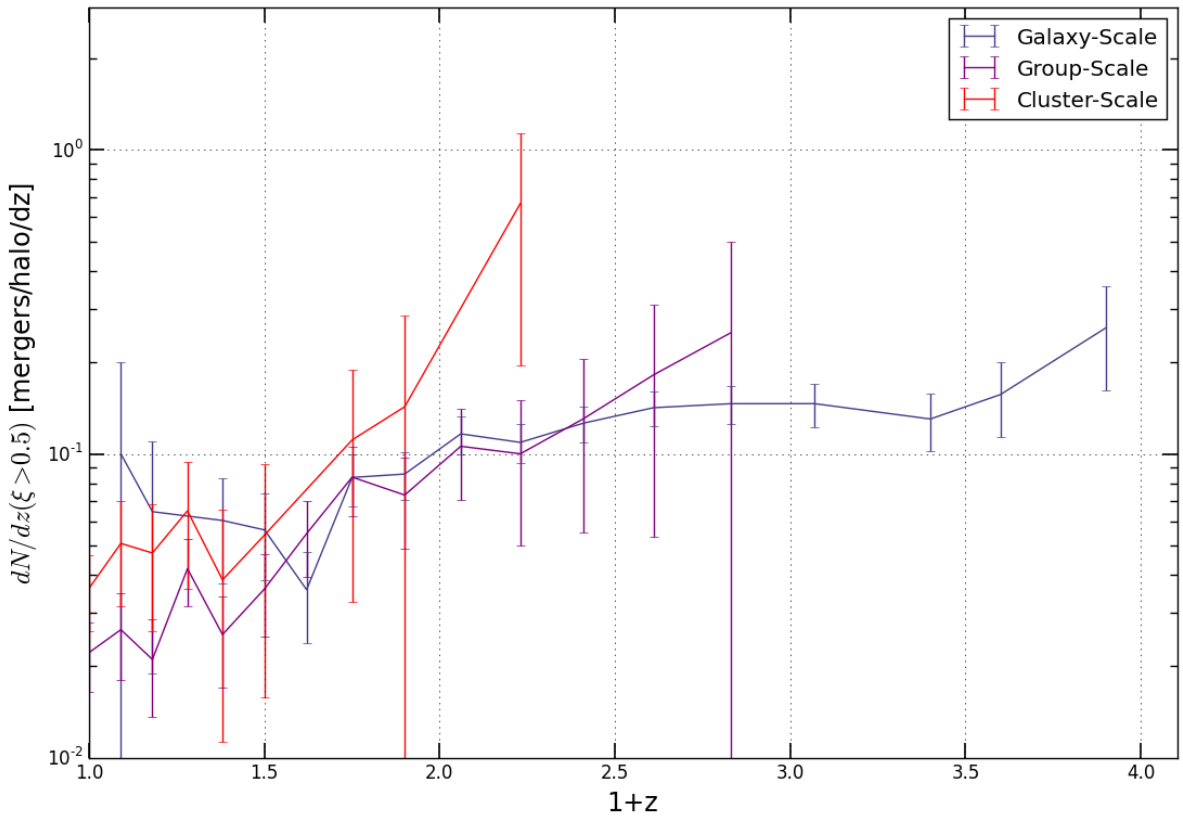

Figure 6.6: The major merger rate for various mass ranges, as a function of redshift. Mass scales are that of galaxy-scale halos ($2 \times 10^{12} \leq M < 3 \times 10^{13}$) in blue, group-scale halos ($3 \times 10^{13} \leq M < 10^{14}$) in purple, and cluster-scale halos ($M \geq 10^{14}$) in red.

major merger rate has a redshift-dependent slope which differs for each mass scale. For cluster-scale halos, we observe a sharp continuous rise in the merger rate at redshifts larger than ~ 1.5, while group-scale halos have a fairly constant rise as a function of redshift over this range. The galaxy-scale halo merger rate appears to begin to rise at a redshift of ~ 3.5, but the data is insufficient to make any serious claim. These merger rates suffer from the same limitations as the merger rates calculated previously, and so simulations with higher mass and time resolution are necessary to make any definitive conclusions.

Chapter 7

Summary/Conclusions

When observing the heating of the red halo during merger, we observed its dependence on the mass ratio of the merging structures and the circularity of the in-fall orbit. Of particular interest to us is the measurement of the concentration as a proxy for the heating of the red halo. As explained previously, the concentration parameter is formulated in terms of the virial radius and the scale radius and since the virial radius is a cosmological quantity more-so than a dynamical one, and so we aim to gain a better understanding of changes to the scale radius. From this observable we attempted to determine how much heating of the host was taking place and what effects it had on the overall structure of the final halo.

We observed that halos are unevenly heated by in-falling material. The halo is heated such that inner shells expand very little, while outer shells expand much more. This is naturally due to the outer shells being less bound. Interestingly, there also appears to be a sharp stabilization of the inner shell radii after the third pericentric passage which can now be considered as the point at which the halos fully merge. The heating overall tends to make the halo expand, which suggests the need for a drop in the concentration parameter due to the increase in scale radius.

The cumulative mass distribution and the density profile both show that material from the core is transported to larger radii during the merger. The fitted scale radius is a convenient parameter with which to measure this heating. The scale radius represents the extent of the core of the halo, within which is contained a quarter of its mass. The overall change in this quantity during the merger appears to have non-trivial dependence on the mass ratio of the red and blue satellite. Using very simple assumptions, however, we have developed a model that provides the ability to estimate the change in the scale radius as

function of the mass ratio of the merging objects (eq. 4.2). The model does not take the circularity nor the total energy of the orbit into consideration, while both may be needed in the future. From our data, this model also appears to underestimate the change in scale radius for moderate mass ratios.

The mixing of the material within the final halo was also investigated. The literature suggests that particles in a halo, on an individual particle level, retain little to no memory of initial conditions, in the form of their initial positions and velocities. It is also stated that these structures are well mixed among themselves during merger, while on a mesoscopic scale binned groups of particles remain quite ordered[18, 5].We find that individual halos are self-mixed to some degree, due to the motions of particles within them. Our research showed however, that this mixing will not be particularly significant, even over the entire course of a major merger. We also investigated the nature of phase-space mixing between the red and blue halos. We expected a certain amount of phase-space mixing among the merging structures due to the fact that they must overlap saptially and because of the exchanges of energy, in principle bringing their velocity distributions closer together. Overall, merging halos will tend towards equipartition of their energies through the dynamical effects discussed in chapter 3. Both these issues were addressed in this study in order to better identify whether the distinction between "old" and "new" material is relevant in phase-space. We find that phase-space mixing is most efficient at mass ratios close to 1:1, while for decreasing mass ratios, we find that the probability of either phase-space distribution being pulled from the other decreases correspondingly. It appears that distinguishing red from blue material in the final structure is relatively easy in an average sense, but impossible on a particle-by-particle basis.

The rank correlation of both observables, the energy and the radius, at the individual level and at the mesoscopic level, indicate that:1) self-mixing is dependent on halo mass ratio, and 2) self-mixing is a less efficient process than previously thought. Self-mixing also appears to be quite limited, with the particles only partially losing rank order and shells showing almost no violation of rank in both energy and radius. The findings at the coarse grained level agree with the literature discussed earlier exceptionally well, while at the individual particle level, mixing is slight less efficient then expected.

Phase-space mixing between merging halos is also found to be dependent on the halo mass ratio. The distance between the self-sampled (red-red or blue-blue) χ^2 distributions and the cross-sampled (red-blue) distribution were found to be anti-correlated to the mass ratio. This implies the presence of a non-trivial difference in the final structure of the blue and red particle distributions. Although identifying the origin of an individual particle is impossible, samples in different regions of phase-space will show systematically different ratios of red/blue particles.

Looking at the merger rates, one can easily see the major mergers play a significant role at higher redshift. Moving back in redshift, most large halos have had a major merger by redshift ~ 2. We also demonstrated through the replication of FMs work that, one can almost completely eliminate the mass dependence of the merger rate at any particular redshift by computing the merger rate per halo as given by B/n from chapter 6. Although this qualitative feature is present in our calculation, the merger rates calculated using our simulation do not agree with that of FM. This is most likely due to the temporal resolution or our halo-finding algortihm. Using the extracted MAHs however, we may estimate the concentration history of any particular halo from simulation. As a result, the increase is scale radius may now be understood and even predicted in order to determine the final state of the halo. We demonstrated this by producing a concentration distribution. In future work, the application of this model will be followed by a comparison with the directly measured concentrations from the simulation.

References

[1] S. W. Allen, D. A. Rapetti, R. W. Schmidt, H. Ebeling, R. G. Morris, and A. C. Fabian. Improved constraints on dark energy from Chandra X-ray observations of the largest relaxed galaxy clusters. *Monthly Notices of the Royal Astronomical Society*, 383:879–896, January 2008.

[2] J. Barnes and P. Hut. A hierarchical O(N log N) force-calculation algorithm. *Nature*, 324:446–449, December 1986.

[3] E. Bertschinger. Self-similar secondary infall and accretion in an Einstein-de Sitter universe. *Astrophysical Journal, Supplement*, 58:39–65, May 1985.

[4] E. Bertschinger. GRAFIC-2: Multiscale Gaussian Random Fields for Cosmological Simulations. Astrophysics Source Code Library, June 2011.

[5] J. Binney and S. Tremaine. *Galactic dynamics*. 1987.

[6] J. S. Bullock, T. S. Kolatt, Y. Sigad, R. S. Somerville, A. V. Kravtsov, A. A. Klypin, J. R. Primack, and A. Dekel. Profiles of dark haloes: evolution, scatter and environment. *Monthly Notices of the Royal Astronomical Society*, 321:559–575, March 2001.

[7] S. Chandrasekhar. Dynamical Friction. I. General Considerations: the Coefficient of Dynamical Friction. *Astrophysical Journal*, 97:255, March 1943.

[8] R. G. Clowes, K. A. Harris, S. Raghunathan, L. E. Campusano, I. K. Söchting, and M. J. Graham. A structure in the early Universe at z˜1.3 that exceeds the homogeneity scale of the R-W concordance cosmology. *Monthly Notices of the Royal Astronomical Society*, 429:2910–2916, March 2013.

[9] C. C. Dantas and F. M. Ramos. Gravitational Mesoscopic Constraints in Cosmological Dark Matter Halos. *Celestial Mechanics and Dynamical Astronomy*, 94:67–81, January 2006.

[10] J. Einasto. On the Construction of a Composite Model for the Galaxy and on the Determination of the System of Galactic Parameters. *Trudy Astrofizicheskogo Instituta Alma-Ata*, 5:87–100, 1965.

[11] O. Fakhouri and C.-P. Ma. The nearly universal merger rate of dark matter haloes in ΛCDM cosmology. *Monthly Notices of the Royal Astronomical Society*, 386:577–592, May 2008.

[12] L. Gao, J. F. Navarro, S. Cole, C. S. Frenk, S. D. M. White, V. Springel, A. Jenkins, and A. F. Neto. The redshift dependence of the structure of massive Λ cold dark matter haloes. *Monthly Notices of the Royal Astronomical Society*, 387:536–544, June 2008.

[13] J. R. Gott, III, M. Jurić, D. Schlegel, F. Hoyle, M. Vogeley, M. Tegmark, N. Bahcall, and J. Brinkmann. A Map of the Universe. *Astrophysical Journal*, 624:463–484, May 2005.

[14] J. E. Gunn and J. R. Gott, III. On the Infall of Matter Into Clusters of Galaxies and Some Effects on Their Evolution. *Astrophysical Journal*, 176:1, August 1972.

[15] L. Hernquist. An analytical model for spherical galaxies and bulges. *Astrophysical Journal*, 356:359–364, June 1990.

[16] Y. P. Jing. The Density Profile of Equilibrium and Nonequilibrium Dark Matter Halos. *Astrophysical Journal*, 535:30–36, May 2000.

[17] Y. P. Jing and Y. Suto. Triaxial Modeling of Halo Density Profiles with High-Resolution N-Body Simulations. *Astrophysical Journal*, 574:538–553, August 2002.

[18] H. E. Kandrup, M. E. Mahon, and H. Smith, Jr. Energy and phase space mixing for self-gravitating systems of stars. *Astronomy and Astrophysics*, 271:440, April 1993.

[19] S. Khochfar and A. Burkert. Orbital parameters of merging dark matter halos. *Astronomy and Astrophysics*, 445:403–412, January 2006.

[20] A. Knebe and V. Wießner. Triaxial versus Spherical Dark Matter Halo Profiles. *Publications of the Astron. Soc. of Australia*, 23:125–128, November 2006.

[21] D. Larson, J. Dunkley, G. Hinshaw, E. Komatsu, M. R. Nolta, C. L. Bennett, B. Gold, M. Halpern, R. S. Hill, N. Jarosik, A. Kogut, M. Limon, S. S. Meyer, N. Odegard, L. Page, K. M. Smith, D. N. Spergel, G. S. Tucker, J. L. Weiland, E. Wollack, and E. L. Wright. Seven-year Wilkinson Microwave Anisotropy Probe (WMAP) Observations: Power Spectra and WMAP-derived Parameters. *Astrophysical Journal, Supplement*, 192:16, February 2011.

[22] A. Liddle. *An Introduction to Modern Cosmology*. Wiley, 2015.

[23] A. D. Ludlow, J. F. Navarro, R. E. Angulo, M. Boylan-Kolchin, V. Springel, C. Frenk, and S. D. M. White. The mass-concentration-redshift relation of cold dark matter haloes. *Monthly Notices of the Royal Astronomical Society*, 441:378–388, June 2014.

[24] A. V. Macciò, A. A. Dutton, F. C. van den Bosch, B. Moore, D. Potter, and J. Stadel. Concentration, spin and shape of dark matter haloes: scatter and the dependence on mass and environment. *Monthly Notices of the Royal Astronomical Society*, 378:55–71, June 2007.

[25] J. McBride, O. Fakhouri, and C.-P. Ma. Mass accretion rates and histories of dark matter haloes. *Monthly Notices of the Royal Astronomical Society*, 398:1858–1868, October 2009.

[26] H. Mo, F. C. van den Bosch, and S. White. *Galaxy Formation and Evolution*. May 2010.

[27] J. F. Navarro, C. S. Frenk, and S. D. M. White. Simulations of X-ray clusters. *Monthly Notices of the Royal Astronomical Society*, 275:720–740, August 1995.

[28] J. F. Navarro, C. S. Frenk, and S. D. M. White. The Structure of Cold Dark Matter Halos. *The Astrophysical Journal*, 462:563, May 1996.

[29] J. F. Navarro, C. S. Frenk, and S. D. M. White. A Universal Density Profile from Hierarchical Clustering. *Astrophysical Journal*, 490:493–508, December 1997.

[30] J. F. Navarro, E. Hayashi, C. Power, A. R. Jenkins, C. S. Frenk, S. D. M. White, V. Springel, J. Stadel, and T. R. Quinn. The inner structure of ΛCDM haloes - III. Universality and asymptotic slopes. *Monthly Notices of the Royal Astronomical Society*, 349:1039–1051, April 2004.

[31] A. Nusser and R. K. Sheth. Mass growth and density profiles of dark matter haloes in hierarchical clustering. *Monthly Notices of the Royal Astronomical Society*, 303:685–695, March 1999.

[32] J. A. Peacock. *Cosmological Physics*. January 1999.

[33] H. C. Plummer. On the problem of distribution in globular star clusters. *Monthly Notices of the Royal Astronomical Society*, 71:460–470, March 1911.

[34] V. C. Rubin and W. K. Ford, Jr. Rotation of the Andromeda Nebula from a Spectroscopic Survey of Emission Regions. *Astrophysical Journal*, 159:379, February 1970.

[35] V. C. Rubin, W. K. J. Ford, and N. . Thonnard. Rotational properties of 21 SC galaxies with a large range of luminosities and radii, from NGC 4605 /R = 4kpc/ to UGC 2885 /R = 122 kpc/. *Astrophysical Journal*, 238:471–487, June 1980.

[36] M. I. Scrimgeour, T. Davis, C. Blake, J. B. James, G. B. Poole, L. Staveley-Smith, S. Brough, M. Colless, C. Contreras, W. Couch, S. Croom, D. Croton, M. J. Drinkwater, K. Forster, D. Gilbank, M. Gladders, K. Glazebrook, B. Jelliffe, R. J. Jurek, I.-h. Li, B. Madore, D. C. Martin, K. Pimbblet, M. Pracy, R. Sharp, E. Wisnioski, D. Woods, T. K. Wyder, and H. K. C. Yee. The WiggleZ Dark Energy Survey: the transition to large-scale cosmic homogeneity. *Monthly Notices of the Royal Astronomical Society*, 425:116–134, September 2012.

[37] V. Springel. The cosmological simulation code GADGET-2. *Monthly Notices of the Royal Astronomical Society*, 364:1105–1134, December 2005.

[38] J. E. Taylor. Dark Matter Halos from the Inside Out. *Advances in Astronomy*, 2011:6, 2011.

[39] J. E. Taylor and A. Babul. The Dynamics of Sinking Satellites around Disk Galaxies: A Poor Man's Alternative to High-Resolution Numerical Simulations. *Astrophysical Journal*, 559:716–735, October 2001.

[40] J. E. Taylor and J. F. Navarro. The Phase-Space Density Profiles of Cold Dark Matter Halos. *Astrophysical Journal*, 563:483–488, December 2001.

[41] G. Tormen. The rise and fall of satellites in galaxy clusters. *Monthly Notices of the Royal Astronomical Society*, 290:411–421, September 1997.

[42] F. C. van den Bosch. The universal mass accretion history of cold dark matter haloes. *Monthly Notices of the Royal Astronomical Society*, 331:98–110, March 2002.

[43] N. Voglis, N. Hiotelis, and M. Harsoula. Surviving Memory in Violently Relaxing Systems. *Astrophysics and Space Science*, 226:213–228, April 1995.

[44] H. Y. Wang, Y. P. Jing, S. Mao, and X. Kang. The phase-space distribution of infalling dark matter subhaloes. *Monthly Notices of the Royal Astronomical Society*, 364:424–432, December 2005.

[45] W. A. Watson, I. T. Iliev, A. D'Aloisio, A. Knebe, P. R. Shapiro, and G. Yepes. The halo mass function through the cosmic ages. *Monthly Notices of the Royal Astronomical Society*, 433:1230–1245, August 2013.

[46] R. H. Wechsler, J. S. Bullock, J. R. Primack, A. V. Kravtsov, and A. Dekel. Concentrations of Dark Halos from Their Assembly Histories. *The Astrophysical Journal*, 568:52–70, March 2002.

[47] A. R. Wetzel. On the orbits of infalling satellite haloes. *Monthly Notices of the Royal Astronomical Society*, 412:49–58, March 2011.

[48] A. W. C. Wong and J. E. Taylor. What Do Dark Matter Halo Properties Tell Us about Their Mass Assembly Histories? *Astrophysical Journal*, 757:102, September 2012.

[49] J. K. Yadav, J. S. Bagla, and N. Khandai. Fractal dimension as a measure of the scale of homogeneity. *Monthly Notices of the Royal Astronomical Society*, 405:2009–2015, July 2010.

[50] D. H. Zhao, Y. P. Jing, H. J. Mo, and G. Börner. Accurate Universal Models for the Mass Accretion Histories and Concentrations of Dark Matter Halos. *Astrophysical Journal*, 707:354–369, December 2009.

[51] D. H. Zhao, H. J. Mo, Y. P. Jing, and G. Börner. The growth and structure of dark matter haloes. *Monthly Notices of the Royal Astronomical Society*, 339:12–24, February 2003.

[52] F. Zwicky. Die Rotverschiebung von extragalaktischen Nebeln. *Helvetica Physica Acta*, 6:110–127, 1933.